Detecting High Saturation- and Groundwater Flow Zones Using Active Heating-Based Distributed Temperature Sensing

A Thesis Submitted to

The Graduate School of Natural Science and Technology,

Shimane University

In Partial Fulfilment of the Requirements for the Award of Degree of

Doctor of Philosophy

in Science

(Doctoral Program Majoring in Science and Engineering for Innovation)

By

ASHIS ACHARYA

Student ID: N22D206

Matsue, Shimane

July 2025

DECLARATION

I hereby declare that the research work embodied in this thesis is the result of my own original investigation and has been conducted independently under the guidance of my academic supervisors. To the best of my knowledge, this work has not been submitted, either in part or in full, for the award of any degree or diploma at this or any other academic institution.

The experiment was carried out under the supervision of Professor Dr. Tetsuya Kogure (Disaster Prevention Research Institute, Kyoto University, Uji, Kyoto) and Associate Professor Dr. Hideki Mukoyoshi (Department of Earth Science, Shimane University, Matsue, Shimane).

I also confirm that my research advisor has read and approved the thesis for submission to the University.

Every source of information mentioned in the draft has been appropriately cited.

Ashis ACHARYA

ACKNOWLEDGEMENTS

After more than three years of dedicated and hard work, I am proud to share this version of my PhD thesis with you. By going through this journey, I learned many lessons which made me stronger due to continuous comfort and support from many individuals, for which I really want to thank them.

First and foremost, I would like to express my utmost gratitude to my supervisor, Professor Dr. Tetsuya Kogure, for encouraging valuable guidance, care, and motivation throughout my doctoral journey. Dr. Kogure consistently motivated me to write scientific papers, attend international conferences and workshops, and provided both emotional and professional support during times of difficulty. Having him as a mentor, I had the opportunity to work on research in one of the most fascinating and well-known fields of distributed fibre-optic sensing for both geotechnical and engineering geological applications. I was impressed by how he managed to set up all the required opto-electronic equipment both in the laboratory and outside, despite dealing with the problem with the funds. Even though I had little knowledge about the relevant research during the first encounter with Dr. Kogure in early 2022, his enlightening support and insightful guidance nourished me to grow technically, making me more confident. I still recall one powerful message he shared with me during a meeting: "*Your research papers change your fate*". That single sentence became a driving force in my academic journey, encouraging me to devote myself to impactful research.

I am equally grateful for the invaluable encouragement and support from Professor Dr. Tetsuya Sakai and Associate Professor Dr. Hideki Mukoyoshi, Department of Earth Science, Shimane University, during my doctoral studies, which meant a lot to me. Because of their

attentive guidance along with many opportunities for exploring the geology and geomorphology of Shimane Peninsula, I have added great value to my academic experience.

I would also like to extend my deepest appreciation to my technical advisor, Professor Fumihiko Ito, Professor of Instrumentation Systems Engineering at Shimane University, for his invaluable support throughout my journey. His willingness to share his knowledge as a core member of the team that developed the monitoring system used in this study was very valuable for the progress in my research. I appreciate his generous guidance, technical insights and continuous support in this research work.

I am also deeply thankful to our research collaborator, Dr. Toshihiro Sakaki (ESE Consulting, LLC, Ashiya, Hyogo, Japan). His constructive feedback, along with the detailed discussion, data analysis support, and guidance during manuscript writing, has significantly helped me to improve the quality and clarity of my research. I am also equally grateful to other collaborators, including Dr. Issei Doi and Dr. Mitsuru Komatsu, for their invaluable support during my PhD journey.

My heartfelt thanks go to my colleagues, Ms. Sweta Guragain and Mr. Tong Morigen, for their unwavering support and encouragement during this work.

I want to express my sincere appreciation towards the Ministry of Education, Culture, Sports, Science and Technology (MEXT), Japan, for awarding me the MEXT scholarship, which financially helped me to conduct my doctoral thesis in Japan and devote all my efforts to research. I am also very grateful to the Sasakawa Scientific Research Grant 2023 (The Japan Science Society) for partially supporting my research, which helped me carry out several experiments and join different international conferences, aiding the success in my

research. Further, I am grateful to the Japan Science Society for selecting my research among the top sixteen highly evaluated research results in Japan.

My appreciation goes to the entire Asian Dining AGAN family, one of the popular Indian/Nepali restaurants in Shimane. I am especially thankful to dear brother Prabin Karki and sister-in-law Purnima Thapa for making me feel like a family and providing constant emotional support and encouragement throughout the PhD journey.

Thank you to all my friends, colleagues and supporters from Nepal, Bangladesh and Pakistan for being by my side during good times and bad times. The support, courage, and friendly gestures I received from you all have truly touched me and helped me during my difficult times while conducting this research work.

Last but not least, I want to express my profound love and gratitude towards my parents and family members for their consistent love, support, kindness, as well as for the endless inspiration. I will always be indebted towards their sacrifices and encouragement, which motivated me to achieve this milestone.

From the bottom of my heart, I want to thank everyone who has been a part of this meaningful journey, directly or indirectly, with me.

.

Ashis ACHARYA

ABSTRACT

Active heating-based distributed fibre-optic sensing (AH-DFOS) has emerged as a promising technique for subsurface groundwater flow characterisation, yet its application in complex geological settings remains limited. This study evaluates the applicability of a novel phase noise-compensated optical frequency-domain reflectometry (PNC-OFDR) sensing method for resolving subsurface hydrologic features in turbiditic fractured aquifers. First, two feasibility studies were conducted in a controlled laboratory setting.

In feasibility study-I, a heating cable (H-cable) was embedded within a 2 m-long cylindrical cement grout specimen and subjected to various heating powers. A sensing optical cable (T-cable) was placed adjacent to the heating cable to monitor the temperature distribution continuously. Two water-holding boxes were installed along the specimen at two positions to retain water that mimics high-saturation zones around a grouted borehole in practical applications. The study's results indicated that the PNC-OFDR technique demonstrated a high sensitivity to even small ΔT, enabling it to pinpoint water locations at two distinct points accurately with a spatial resolution of 2 cm and a temperature resolution of 0.1 °C. The research determined the minimal heating power required to successfully locate the water positions. The magnitude of the heating power exerted a significant impact on the ΔT. Three distinct phases of temperature increment were observed for a given heating period: rapid, fast, and gentle increase.

In feasibility study-II, a novel method was introduced to monitor the location of high-saturation zones using the AH-DFOS method with an optical fibre-embedded fully grouted

rock bolt (FGRB). A 1 m-long cement grout specimen with a fibre-optic cable instrumented FGRB was prepared, and water was introduced at various positions along the axial position to simulate high-saturation zones/groundwater flow along rock fractures. The results demonstrated a strong potential of the AH-OFDR method for water monitoring in grouted bolt installations. When sufficient heating power was applied, the sensing cable's distance from the heating cable had minimal impact. Due to its high spatial resolution, even fine, closely spaced hydraulically active fractures can be detected. Centrally grouted instrumented bolts required slightly higher heating power for effective water detection, and sensing cables closer to the heating cable provided more uniform temperature responses. The results indicate that using a separate sensing cable provides clearer detection of water-saturated zones and closely spaced fractures. A concept of *thermal halo* formation on either side of the high saturation zones was presented. The rate of ΔT decreased as the width of the high-saturation zones increased. This method has significant practical implications for geotechnical applications, including slope stability assessment, tunnelling, foundation monitoring, and dam reinforcement, where rock bolts are commonly employed as stabilising structures.

The results obtained from feasibility experiments were validated by employing the method inside a 50 m-deep borehole within a highly fractured turbiditic deposit. Heating and temperature-sensing fibre-optic cables were installed into the cementitious grouted borehole, enabling high-resolution temperature monitoring under controlled heating. By applying electrical power of 7.6 W/m through an embedded metallic wire and analysing the resulting thermal response, several zones of saturation and active groundwater flow were identified under ambient conditions. The heating thermal response curves exhibited noticeable noise

that increases with time, while the recovery response exhibited a much smoother trend, decreasing noise with time. The results indicate that approximately 25% of observed fractures were hydraulically active. Moreover, lithological variability induced depth-dependent thermal responses, highlighting the influence of geological heterogeneity on heat transport. Recovery (cooling) data following cessation of heating proved essential for accurate localisation of water-bearing zones and estimation of thermal properties. Field-based AH-DFOS results showed strong agreement with laboratory-derived λ values. The rainfall events showed evidence of alteration of the subsurface water flow, resulting in enhanced advective cooling or thermal dispersion. This study demonstrated the effectiveness of AH-DFOS in providing high spatial and temperature resolution, rapid data acquisition, and robust detection of hydraulically active fractures, which are key information for advancing subsurface hydrogeological investigations.

Keywords: Distributed temperature sensing, thermal response, optical frequency-domain reflectometry, cement grout, grouted rockbolt, high-saturation zones, groundwater flow detection, thermal conductivity

Table of Contents

List of tables

List of figures

List of Abbreviations

AH	Active heating
AH-DFOS	Active heating-based distributed fibre-optic sensing
AI	Auxialiary interferometer
APC	Angled physical contact
BFS	Brillouin frequency shift
BOTDA	Brillouin optical time domain analysis
BOTDR	Brillouin optical time domain reflectometry
BPD	Balanced photodetector
BTS	Brazilian tensile strength (MPa)
CD	Conduction dominant
DFOS	Distributed fibre-optic sensing
DTS	Distributed temperature sensing
e	Void ratio
E	Young`s modulus (GPa)
ECD	Enhanced conduction dominant
FBG	Fibre Bragg grating
FFT	Fast Fourier transform
FGRB	Fully grouted rock bolt
FO	Fibre-optic
FOS	Fibre-optic sensing
FUT	Fibre under test

G_s	Specific gravity
JIS	Japanese industrial standards
λ	Thermal conductivity (W/mK)
MI	Main interferometer
OFDR	Optical frequency-domain reflectometry
OTDR	Optical time-domain reflectometry
PNC-OFDR	Phase noise compensated optical frequency-domain reflectometry
RB	Rayleigh backscattering
RQD	Rock quality designation
SEM	Scanning electron microscope
SNR	Signal-to-noise ratio
TLS	Tunable laser source
TRT	Thermal response test
TTPA	Tempos thermal properties analyser
UCS	Uniaxial compressive strength (MPa)
V_p	P-wave velocity (km/s)
w	Water absorption
XRD	X-ray diffraction
γ	Unit weight
ϕ	Porosity

CHAPTER I INTRODUCTION

1.1 General background

Understanding the physical phenomena that affect our Earth's natural system has become more critical in recent years. It has become apparent that it is difficult to accurately quantify physical quantities such as temperature, pressure, strain, and deformation. Since these factors significantly impact our physical environment, they must be adequately understood. As a result, the scientific community is very concerned with improving the precision of physical parameter measurements.

Temperature is one of the most prevalent and significant physical parameters in the Earth's system. Monitoring underground temperature fluctuations is important to investigate subsurface flow dynamics (Maldaner et al., 2019). It is more challenging, especially in the case of groundwater flow in fractured aquifers, due to the irregular distribution and close spacing of fractures. A common way of measuring groundwater temperature is by using thermometers, thermocouples, or waterproof temperature loggers inside boreholes (Yanes et al., 2025). All of these devices are discrete point sensors with separate wire connections to the surface, so that the spatial resolution of the collected temperature data is determined by the number of sensors installed over a certain distance.

Optical fibres were primarily developed for the telecommunications industry, but during the past two decades, their application has dramatically risen in a wide range of technological disciplines, including structural health monitoring (Bado and Casas, 2021; Gómez et al., 2020), geohazard assessment (Puzrin et al., 2020; Zhang et al., 2021), industrial engineering (Campanella et al., 2016), and environmental monitoring (Amer et al., 2021). In recent years, fibre-optic sensing (FOS) techniques have revolutionised the study of groundwater temperature, offering significantly higher spatial, temporal, and

temperature resolution compared to traditional sensors (Cao et al., 2018; Coleman et al., 2015; Maldaner et al., 2019; Read et al., 2014). This technique operates by launching light of a specific energy along the fibre core, with an interrogation unit collecting the backscattered light. Changes in the frequency of the backscattered light are then used to determine variations in temperature or strain (Acharya et al., 2024; Kogure and Okuda, 2018). Geoscientists have monitored temperature fields using FOS techniques for continuous and real-time monitoring of seepage phenomena (Su and Kang, 2013), tunnelling (Minardo et al., 2018), mining (Tang and Cheng, 2018), and oil and gas pipeline monitoring (Ren et al., 2018). Several applications of FOS methods for the SHM of civil engineering structures are also documented in the literature (Ye et al., 2014, Acharya et al., 2024).

Distributed fibre-optic sensing (DFOS) methods, a type of FOS technique, have received much attention since they have unrivalled capabilities and unprecedented features. DFOS incorporates Rayleigh, Raman, or Brillouin scattering in the time or frequency domain to measure parameters such as temperature, stress, strain, and other acoustic properties (Kishida et al. 2014; Schenato et al. 2017). Compared to conventional geotechnical sensors, this sensing technology has been widely used due to a range of unique benefits, including easy and fast data transfer, high sensitivity to strain and temperature, long-term durability, long-distance and real-time monitoring, cost-effectiveness, compatibility, and resistibility (Barrias et al. 2016). Vlachopoulos (2023) summarised the lessons gained from their previous research activities and emphasised the insights acquired over the past two decades regarding the application of DFOS for monitoring rock masses and supporting elements in underground excavations. They highlighted the advantages of employing the DFOS technique based on their two decades of experience, as illustrated graphically in Fig. 1. Sensors based on DFOS, when embedded into sliding masses,

function akin to the nerves in the human body, adeptly capturing extensive information to assess the health condition of the landslide (Zhu et al., 2023). These innovative sensing approaches serve as uninterrupted sensors spanning tens of kilometres, enabling monitoring of various physical parameters such as strain and temperature (Wijaya et al., 2021). In other words, using the DFOS method is equivalent to placing hundreds or even thousands of point-based monitoring tools (Wei et al., 2022).

The active heating (AH) method utilising the DFOS technique (commonly referred to as AH-DFOS) for groundwater characterisation has been a hot topic in recent years. In this technique, the heat is artificially injected along the metallic armour of the optical cable, and the temperature rise with time is monitored using an adjacent sensing cable to detect subsurface water movement (Acharya et al., 2024). This unique approach has the advantages of sub-meter spacing, real-time monitoring, and distributed temperature measurements, which show the potential of monitoring the high-saturation zones and active groundwater flow (Bakx et al., 2019; Briggs et al., 2016).

Among DFOS methods, optical frequency-domain reflectometry (OFDR) has emerged as a particularly promising technique. The OFDR offers exceptionally high spatial resolution, up to the millimetre scale within a monitoring range of approximately 100 meters, along with superior measurement accuracy. Recently, Sun et al. (2024) demonstrated the advantages of the OFDR sensing method over conventional distributed temperature sensing (DTS) systems based on Raman scattering for achieving continuous spatial and temporal monitoring of soil infiltration processes. Acharya et al. (2024) introduced a novel phase-noise compensated OFDR approach capable of detecting high-saturation zones, achieving a spatial resolution of 2 cm and a temperature resolution of 0.1 °C. Further, the same research team demonstrated the strong potential of using a fibre-optic cable instrumented fully grouted rock bolt (FGRB) for detecting high-saturation

zones. Although OFDR shows significant promise for the high-accuracy detection of groundwater flow, applications of this method in geohydrologic studies remain limited, indicating a need for further research and development.

1.2 Fibre structure and concept of light scattering

The fundamental structure of an optical fibre is shown in Fig. 2. An optical fibre is a silica- or plastic-based light conduit that carries light from one end to the other. The core, cladding, and buffer are the three concentric layers that constitute an optical fibre's overall structure. The core is the central cylindrical layer that is very thin and carries light from one end to the other. The core is generally made up of silica (SiO_2), and the melting point of pure SiO_2 glass is 1610 °C; however, this temperature varies depending on the additional agents used (Mikolajek et al., 2020). The core is covered by glass cladding, and the light gets trapped inside the core due to the difference in refractive index between the core and the cladding (Addanki et al., 2018). The outermost non-optical plastic layer, the buffer, further encapsulates both layers. The buffer protects the fibre from physical damage and prevents the optical fibre from scattering losses caused by microbends.

The phenomenon of light scattering along optical fibres has been well-established since the 1970s. However, in the field of sensing, this phenomenon has been utilised since the 1990s. Given that the angle of the incident light inside the core is greater than the critical angle, the function of the optical fibre is dependent on the theory of total internal reflection, which occurs at the interface between the core and cladding. A light wave interacts with the atoms and molecules as it travels through them. The electric field creates a time-dependent polarisation dipole when the light wave is far from a medium's resonance. The induced dipole generates a secondary electromagnetic wave, which is light scattering (Bao and Wang, 2021). Due to variations in density and composition, the light beam interacts with

the fibre, and some photons return to the light source, causing backscattering. The elastic and inelastic back-propagating light helps to characterise fibre imperfections (Bao and Wang, 2021; Barrias et al., 2016). The properties of the backscattered light can be characterised by phase, frequency, and amplitude to predict the changes in physical factors such as strain and temperature along the fibre. The energy ratio between the incident and backscattered light is significant for predicting fault location along the optical fibre.

Single-mode fibre (SMF) and multimode fibre (MMF) are two types of optical fibres based on their mode number. An SMF can only propagate one mode of light, whereas an MMF has a large core that can propagate multiple light modes. SMF cores typically range from 5 to 10 μm in diameter, with 8 μm being typical. Signals with wavelengths of 1310 or 1550 nm can propagate through an SMF core with a relatively small diameter. SMF cables are designed to maintain each optical signal's spatial and spectral integrity over long distances, allowing data to be delivered faster. In SMF, light propagation is only possible when $v < 2.405$, which is defined by Eq. (1) (Addanki et al., 2018):

$$v = \frac{2\pi a \sqrt{n_1^2 - n_1^2}}{\lambda_0} \tag{1}$$

where v is the normalised frequency, a is the fibre core diameter, λ_0 is the light propagation wavelength, and n_1 and n_2 are the RIs of the core and cladding, respectively.

MMFs have core sizes of 50-62.5 μm and can accommodate a variety of independent light modes within the core's width (Addanki et al., 2018). MMFs transmit high-bandwidth data across a small distance of less than 1 km. Multiple pathways convey a light signal through the MMF's core; the signal usually passes through the cable's core at a wavelength between 810 and 1300 nm (Nyarko-Boateng et al., 2020). Due to the slight RI difference

and low coupling efficiency of the input power, the backscattered power of an SMF is approximately 10 dB lower than that of an MMF (Nakazawa, 1983).

1.3 Types of fibre-optic sensing

The FOS methods are categorised into two different categories: (a) discrete and (b) distributed (Fig. 4), which are briefly described in the following sections.

1.3.1 Fibre Bragg grating (FBG)

An FBG is a short portion of an optical fibre where the refractive index undergoes periodic modulation. This modulation creates a distinctive pattern that reflects specific wavelengths of light while allowing others to pass through. Following the pioneering work by Hill et al. (1978), who introduced the first FBG sensor, this technology has gained widespread use in the field of engineering geology and civil engineering due to several advantages it offers over traditional electrical gauges, such as good reliability, immunity to electromagnetic interference, and multiplexing capacity. When an FBG experiences mechanical strain or temperature abnormalities, the Bragg grating period (Λ) will change, leading to a peak shift in the reflected wavelength, called the Bragg wavelength shift ($\Delta\lambda_{\text{Bragg}}$) (Fig. 5). This property makes FBGs highly responsive and versatile as sensing devices. The relationship between the $\Delta\lambda_{\text{Bragg}}$ and the combined effects of axial strain ($\Delta\varepsilon$) and temperature change (ΔT) is linear and can be described by Eq. (2) (Hill and Meltz, 1997):

$$\frac{\Delta\lambda_{\text{Bragg}}}{\lambda_0} = C_\varepsilon \Delta\varepsilon + C_T \Delta T \tag{2}$$

where C_ε and C_T are strain and thermo-optic sensitivity coefficients, respectively.

The FBG sensors respond to mechanical strain and temperature variations, necessitating the need to account for and differentiate between these factors. When

measuring temperature with an FBG sensor, it should ideally be kept unstrained. Consequently, changes in the reflected wavelength caused by temperature variations are primarily attributed to alterations in the fibre's refractive index. On the other hand, when using FBG sensors for strain measurement, it becomes crucial to compensate for temperature effects. This compensation is achieved by placing an FBG temperature sensor in close proximity to the FBG strain sensor. By subtracting the wavelength shift observed in the FBG temperature sensor from that of the FBG strain sensor, any temperature-related influences on the wavelength data are effectively eliminated. Due to the dual sensitivity of FBG sensors to both mechanical strain ($\varepsilon_{\text{mech}}$) and apparent or thermal strain ($\varepsilon_{\text{thermal}}$), a distinction between these two types of strain is necessary, as outlined in reference using Eq. (3) (Shiratsuchi and Imai, 2021):

$$\varepsilon_{\text{mechanical}}+\varepsilon_{\text{thermal}}=\frac{\Delta\lambda_{\text{Bragg}}}{\lambda_0}\frac{10^6}{F_{\text{G}}}\ (\text{in } \mu\text{m/m}) \tag{3}$$

where F_G represents the gauge factor.

1.3.2 Distributed fibre-optic sensing (DFOS)

DFOS technology allows continuous measurements along the entire length of optical fibre cables; hence, its name is "*distributed*". Figure 6a illustrates the fundamental principle behind DFOS. These DFOS-based sensors are integrated into the structural network, similar to how the human nervous system functions.

The DFOS methods currently in use leverage three different scattering phenomena occurring in the fibre core: Brillouin scattering, Raman scattering, and Rayleigh scattering, either in the optical time-domain (OTDR) or the optical frequency-domain reflectometry (OFDR), as depicted in Fig. 6b. In OTDR, a brief light pulse is injected into the fibre, and the backscattered signal is recorded based on the time it takes to return. While OTDR

provides long-range measurements of physical properties, it suffers from poor spatial resolution, which improves as the bandwidth of the input pulse decreases. However, reducing pulse power significantly impacts the signal-to-noise ratio (SNR) and the sensing range of OTDR (Lu et al., 2019). On the other hand, OFDR employs a swept-wavelength light source that generates two signals: a probe signal sent through a fibre under test (FUT) and a reference signal. The light backscattered from the FUT is combined with the reference signal and detected by balanced photodetectors (BPDs). The time delay between the probe and reference signals allows the determination of a beat frequency. Applying a Fourier transform to the detected signal enables the calculation of the beat frequency value and mapping where the backscattered signal originated (Ding et al., 2018). Rayleigh-based OFDR applications are less common than the others due to their limited measurement range (typically spanning tens of meters) and the higher cost associated with the interrogation unit.

Both Brillouin and Raman scattering exhibit both Stokes and anti-Stokes characteristics. The absorption of a molecule's photon triggers an electron's excitation to a higher energy level. When the electron returns to a lower energy state, it emits a photon with an energy difference proportionate to the absorbed photon. The emitted photon's power can either be higher, lower or remain equal to that of the incident photons. When the emitted photon is stronger than the incident photon, this is referred to as the Stokes component (as shown in Fig. 6c). Conversely, the anti-Stokes component comes into play when the emitted photon possesses less energy than the incident photon. This component is susceptible to temperature variations (Li and Zhang, 2022). The local temperature measurement can be determined by examining the ratio between the intensities of the anti-Stokes and Stokes light signals (Farahani and Gogolla, 1999). However, it’s worth noting

that in Rayleigh scattering, there is no change in energy between the incident and emitted photons.

The most widely employed method for measuring strain over extended distances in geotechnical applications is the use of Brillouin-based DFOSs such as Brillouin optical time domain analysis (BOTDA) and Brillouin optical time domain reflectometry (BOTDR) (Hu et al., 2020). In the BOTDA set up, a pump pulse of light is launched at one end of an optical fibre and travels towards the opposite end, where a probe light wave is continuously emitted in the opposite direction. This arrangement allows for a Brillouin interaction between the two waves, enabling the distributed measurement of the Brillouin frequency shift (BFS) within the fibre core (Xu et al., 2018). In contrast, BOTDR involves the launch of a laser pulse into an optical fibre, with some of the Brillouin-scattered light returning to the input end for measurement. This scattering of light results from the nonlinear interaction between the incident light and the excited photons within the medium through which the light propagates, leading to a change in frequency known as the Brillouin shift. Table 1 illustrates the performance differences between the various DFOS techniques. For a comprehensive assessment of the performance characteristics of these sensing techniques, readers can refer to our previous publication (Acharya and Kogure, 2022). More details of the operational features of these sensing technologies can be found in (Forbes et al., 2018; Vlachopoulos, 2023).

1.4 Basic concept of distributed temperature sensing

The copper wire in the heating cable implanted inside a cementitious grout is the heat source for the distributed temperature profile registered by the sensing cable. Due to the high heat capacity and thermal conductivity (λ) of water, the local temperature field will be affected by the presence of the water. If the anomaly of temperature fields is identified with

the DFOS system by measuring the spectral shift, the high-saturation zones can be located and monitored (Su et al., 2015). This is the primary idea behind temperature monitoring with DFOS sensing. Equation 4 describes the relationship between spectral shift, temperature and strain change (Cheng et al., 2021):

$$\Delta v_R = C_T \Delta T + C_\varepsilon \Delta \varepsilon \quad (4)$$

where v_R is the Rayleigh spectral shift. C_T and C_ε are the sensitivity coefficients for temperature and strain, respectively, and they depend on the material composition and geometry of the optical fibre. ΔT and $\Delta \varepsilon$ represent temperature and strain changes, respectively.

Under no influence of strain, Eq. (4) can be written as:

$$v_R = C_T \Delta T. \quad (5)$$

1.5 Motivation for this study

Accurate and high-resolution monitoring of subsurface water movement is critical for understanding hydrogeological processes, assessing groundwater resources, and evaluating slope stability in landslide-prone regions. Traditional point-based methods often lack the spatial continuity needed to capture subtle thermal variations associated with groundwater flow. DFOS sensors offer a promising alternative by enabling continuous, real-time temperature measurements over long distances. However, the effectiveness of such methods, especially in a highly fractured aquifer system, remains limited. This study is motivated by the need to enhance groundwater detection capability by integrating active heating with PNC-OFDR, aiming to achieve high spatial resolution and sensitivity in detecting water-saturated zones adjacent to boreholes. This study aims to optimise heating

parameters such as heating powers and durations, and cable configurations, contributing to the advancement of DFOS applications in geotechnical and hydrogeological investigations.

1.6 Thesis objectives

The central focus of this study is to examine the effectiveness of the high-resolution and high-precision DFOS method, i.e., Rayleigh-based PNC-OFDR sensing, for temperature measurements with the aim of detecting high-saturation and groundwater flow zones. More specifically, feasibility study-I aims to locate high-saturation zones along a two-meter-long cylindrical cementitious grout where heating and sensing DFOS sensors were freely inserted inside. Similarly, feasibility study-II aims to resolve the issues raised by feasibility study-I where sensors were inserted inside the grout using a mock bolt. This study further aims to investigate the effect of DFOS sensor placement relative to the heating element and the applicability of using a composite cable on temperature measurements. Finally, a field study aims to validate and demonstrate the results of feasibility studies on a field scale. The field test further aims to present the sensing method`s ability to characterise the groundwater and high-saturation zones, and to determine the thermal properties of geological layers.

1.7 Thesis organization

The contents of this thesis are organized in the following ways.

Chapter II introduces the fundamental principles of distributed temperature sensing, with a particular focus on active heating techniques. It also provides a concise review of recent developments in DFOS methods applied to groundwater characterisation. Chapter III presents the detailed methodology of this study, including the operational principles of the PNC-OFDR technique. It also describes the types of DFOS sensors used, heating configurations, and associated data acquisition strategies. Chapter IV outlines the

experimental design, results, and interpretation of feasibility study-I, which evaluates the potential of the proposed technique for water position detection with high precision. Chapter V continues with feasibility study-II, offering further insights into the presented technique's applicability to monitor DFOS sensor instrumented bolt monitoring for locating groundwater. Chapter VI focuses on a field-scale demonstration, where the laboratory-validated methodologies are applied to real-world geological settings to assess performance and practical challenges. The challenges and future directions of FOS techniques in strain/temperature sensing for slope monitoring are discussed in Chapter VII. Finally, Chapter VII synthesizes the key findings of this research, highlighting its contributions, limitations, and recommendations for future work.

CHAPTER II DISTRIBUTED TEMPERATURE SENSING

2.1 Fundamentals of active heating and heat transfer process

In the AH-DFOS method, the change of temperature is monitored for detecting the subsurface water movement by injecting heat along an electrically conductive metallic line-source by applying electrical power at a constant rate (Acharya et al., 2024). A sensing cable (T-cable), installed adjacent to the heating line source (H-cable), senses the radially distributed temperature. In short, AH-DFOS represents the coupling effects of two components: (a) heating, and (b) sensing (Fig. 7a). The application of this advanced technique helps to improve our understanding of groundwater flow and heat transport processes in hydrogeological systems (Cao et al., 2018; Coleman et al., 2015).

Figure 7b illustrates the heat transfer process from a metallic line source installed in a grouted borehole when heated at a constant rate. The transfer of heat from the line source to the surrounding rock follows a sequential path through multiple layers: from the metallic wire to the cable buffer, then to the grout, and finally to the surrounding rock. As heat moves outward from the metallic line source, the temperature decreases with increasing distance from the source. The radial distribution of heat forms a gradient, with the highest temperatures closest to the source (represented by the red descending line in Fig. 7b).

The radial distribution of heat is governed by the thermal properties of each material. Initially, with the application of constant heating power along the metallic line source, heat is quickly absorbed by the cable buffer. Within seconds, the buffer reaches its thermal capacity, transferring heat efficiently to the surrounding grout. The grout, with its relatively high λ, acts as a conduit, ensuring effective heat conduction toward the surrounding rock. As heat is continuously applied, it gradually spreads to the surrounding rock via conduction. Due to the rock's lower λ, it absorbs heat more slowly, leading to a steady increase in

temperature over time. It should be noted that in the above scenario, it is assumed that there is no groundwater movement, which would otherwise alter the temperature profile, particularly in fractured zones. It should also be noted that the aquifer heterogeneity, such as variations in subsurface material`s permeability, porosity (ϕ), and the presence of fractures or layers, can significantly affect how heat is transferred in an AH-DFOS system, which is crucial for accurately characterising groundwater flow.

For distributed temperature measurements, two different cable configurations can be adopted: (a) dual cable arrangement; and (a) composite cable arrangement. In the first scenario, an H-cable, comprising one or more metallic conductors, is embedded at a fixed distance d from a T-cable that contains the optical fibres (Fig. 8a). Both cables are encapsulated within a monitoring medium (e.g., cement grout, soil, or grout-filled borehole), allowing heat injected by the H-cable to conduct through the surrounding material and induce measurable temperature gradients along the T-cable. In the second case, a single composite cable incorporates both heating elements (metallic wires) and sensing fibres within a sheath (Fig. 8b). This integrated design eliminates the need for two discrete cables and fixed spacing to infer subsurface fluid flow in geotechnical applications.

In geohydrologic applications, the measurement of temperature variations can be conducted employing both above-mentioned techniques (Bense et al., 2016). However, there have been few studies available in the literature that used a single cable for both objectives. Such a setup consists of electrically heating a FO cable through its steel armouring while continuously monitoring the elevation in temperature along the heated section using the fibres inside the cable (Simon et al., 2023). Therefore, this study also investigates the effectiveness of using two separate cables and a single composite cable for locating the position of water using the OFDR sensing method.

2.2 Active heating of grouted borehole for fractured aquifer characterisation

The AH-DFOS method provides a clear characterisation of transmissive fractures and flow patterns in fractured sedimentary basins (Fig. 9) (Case I – no water flow and no heat input, representing a baseline condition; Case II – heat input without water flow, illustrating pure thermal conduction through the formation; and Case III – simultaneous heat input and groundwater flow along hydraulically active fractures, highlighting advective heat transport. The resulting heating curves reveal variations in subsurface thermal responses, enabling the identification of hydraulically active, inactive, and saturated zones. A deep vertical borehole often penetrates several layers of rock, including fractured zones where water may flow. When heat is injected into a porous medium with groundwater flow through a metallic line-source, it is transferred via two primary mechanisms: conduction and convection (advection) (Maldaner et al., 2019; Munn et al., 2020). Initially, the heat applied by the line source propagates primarily through conduction, moving outward through the grout and surrounding rock materials. This process establishes a predictable temperature distribution based on the thermal properties of the solid materials. The temperature profile is uniform in regions, sometimes with minor fluctuations, where only conduction occurs. However, in zones where groundwater flows along fractured surfaces, the heat transfer process is altered by convection. As water moves through these fractures, it actively carries heat away from the metallic line source, disrupting the expected conductive temperature distribution. This movement of heat via convection creates noticeable anomalies in the temperature profile, called *thermal halo* (Munn et al., 2020). In areas with active groundwater flow, the temperature will be lower than in regions where water is absent or stagnant, due to the continuous removal of heat by the flowing water. These temperature anomalies reflect different water conditions:

- High saturation zones (low velocity zones): The ΔT is less pronounced, as the movement of water is slow, and heat is carried away more gradually.
- Water flow zones (high velocity zones): The temperature drops more rapidly, indicating faster removal of heat. This creates sharper temperature anomalies, which are indicative of more dynamic water movement.

By analysing these variations in the temperature profile, the AH-DFOS system can effectively map groundwater flow and identify fracture flow patterns. Regions with lower ΔT are expected to highlight areas of active water movement, while higher ΔT suggest zones with little to no flow, providing critical insights into the behaviour of subsurface water systems. However, this behaviour would highly depend upon the relative distance between cables.

2.3 Review of distributed temperature sensing for groundwater monitoring

Characterising groundwater flow by the heat tracing method is important to investigate subsurface flow processes and assess the environmental risks. Thanks to their unprecedented capacities of real-time, distributed, and continuous monitoring over a vast area, DFOS techniques opened up the possibility to study underground temperature where a fibre-optic sensor can provide a vast number of measurement points along its entire length. Such DFOS-based sensors, when installed into the borehole and some other reinforcements, function similarly to how the human nervous system functions because of its nature of continuous measurement (Acharya and Kogure, 2024). In recent years, geoscientists have monitored temperature fields using DFOS techniques for continuous and real-time monitoring of seepage phenomena (Su and Kang, 2013), slope assessment (Acharya and Kogure, 2022), tunnelling (Minardo et al., 2018), mining (Tang and Cheng, 2018), and oil and gas pipeline (Ren et al. 2018). Several applications of FOS methods for the SHM of civil engineering structures are also documented in the literature (Ye et al., 2014).

In AH-DFOS method, the heated fibre-optic cable installed inside the borehole can be considered the heat source for monitoring the distributed temperature profile and the sensing fibre installed next to the heated cable senses the changes of temperature, thus providing the information of water-bearing zones (Bakker et al., 2015; Briggs et al., 2016). The AH creates thermal disequilibrium during heating, and subsequent heat dissipation allows the determination of the accurate distribution of groundwater fluxes. The DTS, which is based on Raman scattering, is the most widely investigated AH method for measuring ground temperature and characterising the groundwater dynamics (Coleman et al., 2015; Freifeld et al., 2008; Klepikova et al., 2022; Su et al., 2017). In the DTS method, light scattering along a fibre core is a random process with a very low intensity; therefore, measurements require a longer time of up to 5 minutes (Hakala et al., 2022). The DTS system can measure temperature over significant distances (as long as 30 km), typically in the range of ±1 °C at a resolution of 0.01 °C to a spatial resolution of 1 m (Ukil et al. 2012). After Liu et al. (2013) reported the use of AH-DTS for the first time for high-resolution groundwater flux variations measurements, the field trials of this sensing technique for hydrogeology applications have been getting worldwide attention. Now, this sensing technique has received a great attention for the thermal response test (TRT) to estimate the groundwater flow rate (Hakala et al., 2022; Zhang et al., 2023), groundwater flow variations over time (Simon et al., 2023), seepage monitoring in a slope and within engineering structures (Ghafoori et al., 2020; Kang, 2023; Li and Yang, 2024; Yan et al., 2015), soil moisture content (Benítez-Buelga et al., 2016), and surface water–groundwater (SW–GW) interactions (Banks et al., 2022).

A few examples exist of studies of AH-DFOS for monitoring temperature for hydrologic applications (Coleman et al., 2015; Hakala et al., 2022; Munn et al., 2020; Read et al., 2014). Munn et al. (2020) presented the first field data from multiple AH-DTS field

tests conducted under different hydraulic conditions (natural gradient condition where boreholes were sealed with flexible and impermeable liners, cross-connected condition, and forced gradient condition) to quantify groundwater flow redistribution within a bedrock aquifer. Simon et al. (2023) investigated the feasibility of the AH-DTS method to monitor and quantify groundwater flux variations over time. An experimental study also demonstrated the excellence of the optical frequency-domain reflectometry (OFDR) method compared to the DTS because of its advantage of high-resolution (Sun et al., 2024). The study highlighted that this novel sensing method enables the monitoring of water flow patterns in geological formations such as slopes in variable climatic conditions so that critical layers prone to disasters can be identified, thereby improving the ability to prevent geological hazards. Recently, in Yan'an new district, China, Liu et al. (2024) investigated a 77 m deep borehole consisting of compacted loess and natural loess for the estimation of unsaturated hydraulic conductivity.

CHAPTER III MATERIALS AND METHODS

3.1 Distributed fibre-optic measurement system

A Rayleigh-based OFDR sensing technique was administered to obtain distributed temperature data from the fibre core in all three experimental scenarios (feasibility study-I and II, and field demonstration). Our sensing setup comprised discrete optoelectronic components, such as a power supply, tunable laser source (TLS), balanced photodetectors (BPDs), couplers, circulators, in-line polarisers, and amplifiers. All the experimental activity was carried out in the laboratory.

Figure 10 illustrates the schematic diagram of the operational principle of the PNC-OFDR system. The emitted light from the swept wavelength light source is divided into two branches (auxiliary interferometer; AI, and main interferometer; MI) by a 99.9:0.1 optical coupler (OC), where 0.1% of the power propagates through AI as a reference signal for the phase-noise compensation. In general, the change in the frequency of the light is nonlinear; the beat signal frequency changes with time, resulting in a broad peak after a fast Fourier transform (FFT) analysis. This nonlinearity and phase noise can be compensated by adding a reference interferometer, by significantly improves spatial resolution. A Mach-Zehnder interferometer with a delay fibre of 30 m was used as an AI for compensation.

The first OC's other 99.9% optical power enters the MI to interrogate the fibre under test (FUT). The injected light is split into the reference and probe arms by a 99:1 OC, where 99% of the power enters the reference arm, and 1% propagates along the FUT guided by a circulator. In an FOS system, the FUT is the specific section of the FO cable that is being used to monitor a physical quantity, such as temperature or strain, through the backscattered light generated by the interaction of a laser beam with the fibre. It is specifically designed

to be sensitive to the measured quantity (in this case, temperature) and is usually embedded in the material or structure being monitored. The beam light propagating along the FUT will continuously produce Rayleigh backscattering along the fibre length due to impurities and inhomogeneities. External factors such as temperature and strain impact Rayleigh backscattering in the sensing fibre, and both will change the Rayleigh backscattered spectrum distribution. The light propagating in the reference arm arrives at the balanced photodetectors (BPDs) (PD1 and PD2) before that in the probe arm, which leads to a delay between the two arms and hence the generation of the beat frequency (Chen et al., 2020). After polarisation splitting by a polarisation diversity optical mixer, the beat signals from the MI and signal from the AI are detected by BPDs, which are recorded by the digital data acquisition at a sampling rate of 150 Hz.

The data from the oscilloscope is sent to the personal computer to undergo a numerical compensation process. The distributed temperature information in FUT is obtained by transforming the acquired time-domain signal to the frequency domain via an FFT. Cross-correlations were made to synthesise the information into pictorial form. More details about the measurement principle can be found, e.g., in Fan et al. (2007).

In the PNC-OFDR sensing method, we adopt an auxiliary interferometer with a delay time τ_{ref} to provide phase noise information about the optical source, enabling us to resample the temporal signals of the measurement. The following expression can account for the $\theta(t)$-$\theta(t-\tau_{FUT})$ phase noise term (Fan et al., 2007):

$$\phi(t)=[\theta(t)-\theta(t-\tau_{FUT})]-\frac{\tau_{FUT}}{\tau_{ref}}[\theta(t)-\theta(t-\tau_{ref})] \quad (6)$$

where $\theta(t)$ is the optical phase noise term at time t and τ_{FUT} is the total time a test signal has been delayed from a local signal. In Eq. (6), once τ_{FUT} equals τ_{ref}, the phase term $\phi(t)$ will be cancelled, allowing for the best compensation.

In this method, the length of the FUT could be divided into several sections for phase compensation using different concatenated generated phases (CGPs) calculated using the following Eq. (7):

$$X_N(t)=\sum_{n=0}^{N-1} X_1(t-n\tau_{\mathrm{ref}}) \quad (7)$$

where $X_N(t)$ is a phase term obtained from an auxiliary interferometer, and N is an integer.

3.2 Optical cables used in this study

The present study employed two different types of optical cables: (a) buffered composite cable for heating (i.e., H-cable); and (b) loose-tube gel-filled cable for temperature sensing (i.e., T-cable) (Table 2). The H-cable is the multi-stranded "buffered composite cable" developed by Fujikura in 2014, Tokyo, Japan. The cable is a flat twin type (3.4×2 mm) in which two copper wires are insulated with a specially formulated PVC compound having high insulation resistance and dielectric strength. This cable is the same as the one used by Kogure and Okuda (2018). The PVC compound also ensures additional safety against fires because of its oxygen and temperature index properties. The allowable tensile strength and allowable bend radius of this cable are 230 N and 70 mm, respectively.

The midsection of the cable comprises four optical fibres of different colours: blue, white, pink, and grey, which are positioned side by side. Each optical fibre consists of two concentric layers: core and cladding, having diameters of 0.125 mm and 0.25 mm, respectively. Two copper wires are placed linearly opposite on the outer sides of the fibres to add additional strength to the fibres. The copper wires and fibres are encapsulated in a rigid PVC outer sheath. The sensitivity coefficients of the FR PVC cable for strain and temperature were -0.134 GHz/ με and -3.36 GHz/°C, respectively [α and β in Kogure and Okuda (2018)].

Similarly, the T-cable is the “loose-tube” picocable, which includes four single-mode fibres (blue, green, yellow, and red) and two multi-mode fibres. All fibres are included in a stainless-steel loose tube, which provides the mechanical strength required for handling and installing inside the borehole. In such a loose tube arrangement, if the cable experiences limited elongation (<1%), the fibre inside will not become strained (Tyler et al., 2009).

3.3 Heating strategies

The effectiveness of AH-DFOS depends on the precise control of heat input along the H-cable's steel armour and the system's sensitivity to detect ΔT caused by groundwater movement. A constant heat output along the H-cable in space and time is highly desired. If the cable's electrical resistance varies in time due to temperature effects, the heat output also varies (Coleman et al., 2015). For AH methods, the power output from the H-cable, P [W], can be calculated according to $P=VI$, where V is the voltage, and I is the electrical current with their units of V and A, respectively. The total output power can then be divided by the length of the heated section to obtain the heat generated per meter of the cable (referred as q throughout this paper).

In this study, the electrical heating of the metallic armour in the H-cable was performed using a Takasago DC generating device (Model ZX-S-1600M, Takasago Manufacturing Co., Ltd., Japan). The same heating system was employed in all of our feasibility experiments and field demonstration (Acharya et al., 2024). This device features an output voltage range of 0–320 V, a current range of 0–120 A, and a maximum output power of 1600 W. The power supply device was connected to the copper wires in the H-cable. The cross-section of copper wire is 1.5 mm^2. The copper wires were connected in parallel to minimise the electrical resistance in the cable. Since the ΔT observed during AH methods

strongly depend on q and heating duration (Klepikova et al., 2022), the investigation of required heating and recovery duration prior to conducting experiments is crucial.

In feasibility study-I, six different heating powers were employed to provide heat along the metallic wire of the H-cable, including 1.6, 2.4, 3.5, 4.8, 6.2, and 7.8 W/m (Table 3). Although most ΔT occur in the first 30 to 60 minutes of heating, the heating period was extended to 180 minutes to collect adequate ΔT data. Similarly, in feasibility study-II, the bolt-embedded grout specimen was heated, maintaining a constant heating power of 7.6 W/m for 150 minutes.

In a field demonstration study, three different heating powers (q=3.7, 5.8, and 9.4 W/m) have been tested. The total heating duration for all conditions was 180 minutes. Figure 11 shows the heating line curves from a depth of 25 m to 30 m generated after heating the H-cable along the borehole with the application of variable q. The purpose of this figure is to compare the thermal response generated by applying different q for localising the groundwater flow and high-saturation zones precisely. At low q, such as 3.7 W/m and 5.8 W/m, the position of groundwater can not be clearly identified, and the ΔT values also resulted in a negative value. However, at higher q, such as 9.4 W/m, the high-saturation and water flow zones can be clearly identified, although the heating curves showed a slight fluctuation. Therefore, these results suggest the necessity of a higher q (comparing to other lower q in this study) for a 66 mm diameter grouted borehole to detect the water flow zones. A total heating duration of 180 minutes was observed to be sufficient. It should be emphasized that the highest q of 9.4 W/m in our study is still relatively low as compared to the previous studies (Zhang et al., 2020). After identifying the best q, the time required to fully heat the borehole and precisely locate the water position by applying that best q was also determined.

CHAPTER IV FEASIBILITY STUDY-I

4.1 Background

In this study, with the goal of offering valuable insights into the feasibility of using the PNC-OFDR method for thermal mapping and groundwater flow monitoring within deep boreholes, the effectiveness of the innovative Rayleigh-based PNC-OFDR method for temperature monitoring was evaluated. A series of experiments was designed and executed to create temperature maps along the length of a cementitious grout specimen in a laboratory setting with a fine resolution and rapid measurement times.

4.2 Experimental methods

4.2.1 Preparation of specimen and installation of cables

For feasibility study-I, only the tight buffered cables (mentioned in Table 2) were employed. One was for temperature sensing (temperature measurement cable; T-cable), and the other was for heating (heating cable; H-cable). Two copper wires of the H-cable were welded to each other to form a closed circuit. The grout specimen was prepared in a high-strength PVC pipe (VP-75, inner diameter: 77 mm, outer diameter: 89 mm, and length: 2000 mm) with a mixture of water and cement at a weight ratio of 0.6 (w/c:0.6). The cement used here is the pre-mixed dry NB mortar G115 (Fukuyama Cement Co. Ltd.) (a bag of 25 kg) comprising processed sand (granite), ordinary Portland cement, and expansive agent, with a higher proportion of sand (59.7%) (Table 4). Studies have demonstrated that the sand content of the grouting material has a substantial effect on the bearing capacity of the bolt, i.e., the higher the sand content in the grouting material is, the higher the bearing capacity of the anchorage system due to interface dilatancy (Zhan et al., 2020). Two cables (T- and H-cables) were inserted within the specimen next to each other during casting. Note that

the spacing between the two cables was 15 mm (Fig. 12). Two circular cable guides were used at both ends of the PVC pipe to properly align the cables with an offset such that both cables were positioned at 14 mm from the surface of the specimen. After installing and positioning the T- and H-cables and pouring cement slurry into the PVC pipe, the sample was stored in controlled environments at a temperature of 15–20 °C. The PVC envelope was carefully removed after the 72-hours curing period, and test experiments were performed on the specimen.

The primary rationale for employing two cables positioned adjacent to each other is rooted in the dynamics of heat transfer: when the heating cable undergoes thermal activation through electrical power, heat propagates radially and is subsequently detected by the sensing fibre after a specific duration of AH. However, opting for only one cable (whether T-cable or H-cable) for both heating and sensing functions carries the risk of interference between these two operations. The heat generated by the heating wire could affect the accuracy of temperature measurements taken by the sensing fibres, leading to inaccurate data regarding temperature distribution within the concrete specimen. Moreover, combining them within a single cable could expose the sensing fibres to excessive heat, potentially damaging or affecting the optical properties, making it more difficult to accurately detect and locate water positions along the specimen.

The test sample was connected to the OFDR system to measure the reflectivity of Rayleigh backscattering (RB) signals. To detect the RB signal, it is essential to minimise the reflectance of the optical signals. We employed techniques to minimise the reflectance while applying PNC-OFDR for temperature sensing. Specifically, we utilised an "optical termination" at the end connector to reduce the reflectance from the rest of the cable under test. We used an angled physical contact (APC) connector, which reduces the Fresnel reflection and reflectance to ~-40 to -50 dB. As the reflectance is incredibly sensitive to

cleanliness, the connector ferrule was carefully cleaned with pure isopropyl alcohol. In addition, the fusion splicing was done accurately with zero loss, and the bare fibre was protected using a fusion protector sleeve. Such high-quality fusion splicing ensures minimal signal loss during light transmission. We have used two polarisation controllers in both branches, AI and MI, to adjust the polarisation state of light signals. By twisting the fibre or rotating the paddle of the polarisation controller, we can minimise back reflections and improve the signal quality.

4.2.2 Description of the grout column specimen

The experimental setup illustrated in Fig. 13 was designed with the capability to mimic high-saturation zones (i.e., boxes filled with water) to simulate a 'fractured zone' around a borehole. First, the entire length of the specimen was divided into five sections, from sections I-V. Two polyethylene terephthalate (PET) boxes (200 mm x 140 mm x 120 mm) were installed in sections II and IV to retain water. Therefore, these two sections are referred to as 'water-supplied sections' or `high-saturation zones`, whereas the other three sections (I, III, and V) are described as `no-water-supplied sections` or `pure conduction zones`.

The PET boxes were filled with stagnant water instead of flowing water to create high thermally conductive zones and investigate local temperature field irregularities during AH. Specifically, the areas with stagnant water in sections II and IV were expected to cause temperature field irregularities during AH. These areas can be identified as high water-saturation zones, which is a key principle of temperature sensing. Therefore, the embedded T-cable will collect the temperature field irregularities, which will be monitored in real-time using an oscilloscope. Note that there was a negligible ΔT under normal conditions (i.e., unheated conditions). This means that temperature irregularities can be identified only when ΔT are artificially imposed (i.e., in heated conditions).

4.2.3 Test procedure

The experimental case was designed to analyse the time and space temperature features of heating wires embedded in the test specimen. The experiment was conducted under six different heating powers to better distinguish and compare the ΔT for the various heating phases. First, the specimen was placed inside the experimental room, where the temperature fluctuations were kept as small as possible for a few days so that its temperature equilibrated with the room temperature; afterwards, it was subjected to repeated test experiments. The detailed experimental procedure was as follows:

Step 1: Fill two PET boxes with tap water and keep them steady throughout the test. Take the initial temperature measurement of the water, which is 22 °C.

Step 2: Connect the FUT (T-cable) to the OFDR measurement system and record the baseline temperature (for 10 minutes). The initial measurement taken before starting the heating serves as a reference, such that any subsequent relative temperature measurement indicates ongoing ΔT.

Step 3: Connect the H-cable to the heating device. Adjust the q at 1.6 W/m and remain unchanged throughout the test.

Step 4: Record T-cable temperature data every 30 minutes until 3 hours of continuous heating. Shut off the power to equilibrate its temperature to its original state. This fulfils the first cycle of the test process at an electrical power of 1.6 W/m.

Step 5: Repeat *steps 1* through *4* for q=2.4, 3.5, 4.8, 6.2, and 7.8 W/m.

Step 6: Analyse recorded data with the reference temperature using MATLAB® desktop environment by cross-correlation between Rayleigh spectra and FFT.

4.3 Experimental results

4.3.1 Relationship between temperature change and spectral shift

The elastic dispersion of light caused by the interaction of incident photons with tiny particles along the optical fibre results in RB signals. In this study, we measured the distributed RB signals along the T-cable in the specimen under various heating conditions. We observed a shift in the spectral characteristics when a local perturbation, such as a ΔT, occurred. A thorough examination of the relationship between spectral shift and ΔT across different electrical power conditions demonstrates a highly linear relationship, characterised by a slope of approximately $-\Delta T/\Delta\nu_R \sim 1.5377$ °C/GHz under all heating conditions, as demonstrated by Yan et al. (2015). To exemplify this relationship, data analysis was performed under specific working conditions of 6.2 W/m, drawing upon six data points obtained after 180 minutes of AH from section III (Fig. 14). It is noteworthy that the experimental setup employed to establish this linear correlation resembles the procedure outlined in the "Test procedure" section, i.e., embedding cables within concrete specimens and supplying water in two containers.

4.3.2 Temperature change along the specimen during heating

Figure 15 presents the temporal evolution of temperature along the specimen during a heating period of 3 hours at six different applied voltages. Table 5 summarises the range of the amplitude of ΔT distributed within five distinct sections of the specimen. The position of high-saturation was ambiguous when the sample was continuously heated at 1.6 W/m for 3 hours. However, a slight depression can be observed in sections II and IV. Due to the non-similar nature of temperature fluctuation, the amplitude of ΔT is not provided in Table 5. Thus, from the presented data, it is impossible to accurately determine the location of water within the specimen at q below 1.6 W/m. Sakaki et al. (2019) reported that for a

material with a relatively low λ of 0.26-0.56 W/mK, a q of 2 W/m induced reasonable ΔT; however, for materials with higher λ, a higher power may be necessary.

When the specimen was subjected to AH at a rate of 2.4 W/m, the location of the high-saturation zones could be distinguished clearly. The presence of water was easily identifiable within the boxes positioned along the specimen after just 30 minutes of AH. Sections II and IV exhibited two similar dips due to the water absorbing the heat generated by the heated copper wire. However, the graph trajectory seemed to have oscillated, possibly because of the non-parallel alignment of the cables inside the specimen. A significant peak at about 9.2 m is obviously due to the contact between the H- and T-cable, which can be seen in all working conditions of the power supply. These findings also indicate the considerable challenge of achieving uniformity in measurements despite attempts at parallel cable installation within the structure. For cases with higher q, including 3.5, 4.8, 6.2, and 7.8 W/m, similar temperature dips along the specimen were observed, and the water position was distinctly discernible at higher q.

While the observed temperature fluctuations may have been partially influenced by changes in the ambient temperature, the sample displayed a rapid increase in temperature reaching 60 minutes, followed by a fast increase until 120 minutes of AH. This was followed by a gradual increase in ΔT over the remaining 60 minutes of the heating period. The ΔT rate in the high-saturation zones was significantly slower than the remaining sections surrounded by air (i.e., pure conduction zones), as evidenced by the difference in ΔT detected after 30 minutes and 3 hours. The slow increase in temperature in the high-saturation zones was likely due to the heat taken up by water outside the specimen, as the λ of water is less than concrete, whereas it was difficult for the heat to transfer to the air in the no-water-supplied sections due to the lower λ of air. An examination of the pure conduction zones revealed that the temperature rise was a more significant and upward

incline with cable length in section III compared to sections I and V, which might result from the gradual proximity of the two cables in this section. Although these three sections are not supplied with water and heated with the same electrical power, the ΔT across these three sections does not follow a uniform pattern, which would be expected theoretically. For instance, considering a power input of 7.8 W/m, after 30 minutes of AH, the temperature range in section I is 7.7-17.3 °C, while in section V, it is 16.1-22.7 °C. Similarly, after 180 minutes of AH, the temperature range in section I is 25.8-39.6 °C, and in section V, it is 37.2-48.7 °C (see Table 5). Such a significant fluctuation of temperature was attributed mainly to two factors: (a) *irregularities in cable installation*: The non-parallel alignment of H- and T-cables during pouring of cement slurry, despite using cable guides, results in the measurement of different temperatures along the specimen. Keeping the two cables parallel at a fixed distance is challenging for AH experiments. Higher temperatures were detected where the cables were closer together, and lower temperatures where they were farther apart, resulting in a fluctuating ΔT graph, and (b) *material heterogeneity*: The non-uniform rate of heat transfer within the hardened mortar due to its microstructure variability and uneven ϕ developed during cement pouring, resulting in variations in the ΔT detected by the T-cable. Pores create a more complex heat flow path, increasing overall heat resistance and reducing the material's heat transfer efficiency. Additionally, variations in pore size, shape, and distribution contribute to microstructural inhomogeneity, resulting in uneven heat distribution. However, the effect of these two factors on the fluctuation of ΔT cannot be clearly distinguished because we have no information about the accurate cable array in the specimen and the distribution of material heterogeneity.

Theoretically, the amplitude of ΔT within the concrete specimen during the heating process should exhibit a rapidly increasing and a gradually increasing trend. However, at lower q, such as 2.4 W/m and 3.5 W/m, it was observed that the temperature increase

deviated from this expected behaviour and exhibited a decline after the sample had been heated for 150 minutes. Therefore, further investigation and analysis may be necessary to determine the exact cause of this deviation from the predicted trend

4.4 Discussion and key findings of feasibility study-I

The distributed temperature results in the feasibility study-I demonstrate unequivocally that the OFDR-based DFOS sensor is susceptible to temperature variations and can detect even minor ΔT. The distributed temperature along a 2 m-long grout specimen was monitored using the Rayleigh-based OFDR sensing technique to determine the location of the intervals surrounded by water. The measurement system offered a fast data acquisition time with a fine spatial and temperature resolution.

The heated copper wire embedded in the specimen actively induced temporal temperature variations along the specimen. Two water boxes surrounding the specimen in sections II and IV led to spatial variation in the temperature profile along the specimen. For such cases, the amplitude of ΔT seemed inconsistent at some points. It was observed that the supplied water in sections II and IV led to an irregular change in the local temperature fields. Therefore, the monitoring of high-saturation zones was accurately realised as distinct dips in the temperature profiles. It was also demonstrated that the applied q significantly influenced the ΔT; the higher the q, the greater the ΔT. If the copper wire embedded inside the specimen is heated, the temperature of the wire, and then the specimen, will increase as we supply more heat to it. The influence of the applied q on ΔT has been extensively studied in the literature, with notable contributions by Su et al. (2017) and Su and Kang (2013) in the context of water seepage monitoring.

The results of this study showed that a minimum q required to locate the water position should be established before conducting field research, such as groundwater monitoring

using a borehole. If the q is too low, neither the temperature rise of the optical cable nor the impact on the surrounding environment is immediately apparent. As the applied q increases, the difference becomes more prominent, and it is easier to determine the position of the water. Liu et al. (2019) highlighted that high q should be selected as far as possible within a reasonable range in engineering application monitoring. Recently, Li et al. (2022) also concluded that the heating cable with a higher power supply helps measure and judge the seepage flow. However, it should be noted that the effectiveness of the q depends greatly on the diameter of the borehole and the placement of the FO cables within the concrete anchorage relative to the surrounding rocks. Therefore, it is essential to consider the practicality of monitoring projects and determine the minimum q to generate a temperature rise with a good SNR to locate the water position using the PNC-OFDR sensing method.

More significantly, although two spans of cables (H- and T-cables) were assumed to be embedded parallel with the help of cable guides, a slight variance in the ΔT was observed (a case of 2.4 W/m in Fig. 15 as an example). Leung et al. (2015) also stated that despite the installation of numerous parallel fibres inside the structure, it is challenging to maintain uniformity in the measurements. While the OFDR sensing method promises high accuracy and repeatability, actual measurements (such as strain and temperature changes) often exhibit non-smooth curves due to environmental conditions and irregularities in sensor placement. Original data may show significant fluctuations, complicating the identification of specific temperature/strain trends and necessitating the application of appropriate data processing methods for noise reduction and curve smoothing (Gao et al., 2022).

The trend of average ΔT detected by the T-cable over the time showed three distinct phases for five kinds of power supply: rapid increase (within 60 minutes of the heating period), fast increase (between 60-120 min of the heating period), and gentle increase (last 60 minutes of the heating period) (Fig. 16). It means the rise of temperature was high in the

beginning and followed a decreasing trend over time. Furthermore, a power curve fitting for average ΔT against elapsed time was performed and obtained an equation of the form:

$$y = ax^n \tag{8}$$

where x is the elapsed time and y is the average ΔT inside the specimen. 'a' and 'n' are constants. A study carried out by Li et al. (2022) also showed the three stages of the optical fibre temperature difference with time at three kinds of electron flow (5 A, 10 A, and 15 A). The research carried out by Yan et al. (2015) also agrees with our result. However, note that the equation in this study is a rough approximation because the actual data from the OFDR showed non-smooth curves with significant fluctuations.

The heat transfer between the heated copper wire and porous media is a complex phenomenon that will differ with the variable water supply. In this study, although we have successfully monitored localised temperature variations caused by the presence of water around the concrete specimen using the PNC-OFDR sensing technique, there are still some critical factors that need to be addressed:

i. *Water absorption*: The permeability coefficient of a hardened cement mortar specimen is lower due to the presence of smaller pores. The kinetics of heat transport mechanisms are highly dependent on the pore sizes and the depth of water penetration from the surface towards the interior of the concrete, which is influenced by the rate of water absorption inside the specimen. Therefore, analysing these factors is essential to understand the heat transport mechanisms in cementitious materials comprehensively.

ii. *Heat transfer*: Due to the relatively low λ of concrete compared to other materials, the temperature inside the concrete increases slowly (Su et al., 2017). The area of the concrete specimen in contact with the heated copper wire will experience a higher heat transfer rate than the surrounding areas. This can create a temperature gradient within the

concrete specimen, with the area near the wire being hotter than the surrounding material. Therefore, the thermodynamic property of the optical fibre specimen and convective heat quantity transmitted between the copper wire and water must be evaluated.

Finally, this first experimental study demonstrated the ability of the PNC-OFDR sensing method to accurately monitor and identify the position of water-covered sections within a two-metre-long cement mortar specimen. This sensing approach to temperature monitoring is advantageous over other point-based temperature sensors since it can provide a dense array of temperature data with fine spatial resolution, short data acquisition time, and high processing speed.

The key findings obtained from the feasibility study-I are summarised as follows:

- Heating of copper wires caused a continuous temperature rise along the specimen, with clear differences between high-saturation and pure conduction zones. High-saturation zones showed slower temperature increases due to water's higher λ and specific heat capacity.
- Higher q led to greater ΔT, following three distinct phases: rapid, fast, and gentle increases. Low q of 2.4 W/m was sufficient to detect temperature variations in stagnant water zones, though higher power made water position detection clearer. Minor temperature fluctuations were observed, possibly due to ambient changes.
- Accurate temperature measurements using the PNC-OFDR method depend on key factors: heating power, cable placement, heating duration, and the position of the cables relative to the specimen surface.
- Further investigation into thermal interactions between concrete, water supply, and optical cables is crucial for improving temperature interpretation.

CHAPTER V FEASIBILITY STUDY-II

5.1 Background

The results from the feasibility study-I raised a few significant questions and led to the development of feasibility study-II. In feasibility study-I, H- and T-cables were freely inserted inside the cementitious grout, which resulted in non-uniform temperature measurements, sometimes leading to very high ΔT due to the proximity of two cables, although the high-saturation zones were clearly identified. Therefore, this study focused on investigating the effect of DFOS sensor placement relative to the heating element on temperature measurements using a grouted mock bolt, providing insights into the spatial sensitivity of the technique. The study further investigated the applicability of using a composite cable in AH applications for groundwater characterisation. Moreover, no studies have yet explored the integration of the AH-DFOS method with grouted bolts for the identification of groundwater flow and high-saturation zones. The AH-DFOS approach presented in the feasibility study-II provides a novel framework for seepage monitoring in the vicinity of grouted bolts, enhancing the capability for detecting groundwater movement and assessing structural integrity in geotechnical applications. Under realistic field conditions, this method not only provides spatially distributed information on groundwater flow but also shows strong potential for detecting moisture-induced strain, thereby broadening its effectiveness in long-term monitoring and early warning systems.

5.2 Experimental methods

5.2.1 Bolt structure, cable installation, and sample preparation

In feasibility study-II, a 20 mm × 20 mm, single-row groove aluminium frame was used to simulate the behaviour of a bolt (Fig. 17a). The frame, identified as model HFSC5-2020,

had a length of 1000 mm and a cross-sectional area of 208 mm^2. It featured a groove width of 6 mm and had a mass of 0.56 kg/m. It was assumed that this aluminium frame would be a suitable representation for the intended experimental setup for the following reasons. Despite its complex cross-section, the frame was considered suitable for experimental purposes due to its geometric adaptability for fibre-optic cable integration, enabled by the presence of a longitudinal groove and flat outer surfaces. Typically, rock bolts are made of steel due to their high strength and durability in rock reinforcement applications. However, creating a longitudinal slot in a slender steel component to embed a fibre-optic cable would impose several technical challenges, including slot orientation misalignments, variations in slot depth, inaccuracies in fibre placement, and other installation difficulties (Hoehn et al., 2020). To overcome these issues, this study utilised the above-mentioned aluminium frame with a pre-made slot, allowing for easier and more precise fibre embedding. In realistic field scenarios, similar fibre installation could be achieved by either adhering the cable onto the bolt's surface using high-strength epoxy or embedding it within a manufactured groove, while acknowledging the aforementioned technical constraints. Moreover, since aluminium has a high λ of 237 W/mK (Zhang and Li, 2023), it is suitable for AH applications on a laboratory scale. However, it is important to note that the aluminium frame does not replicate the mechanical properties or structural response of steel bolts used in situ.

In slope stability applications, rock bolts typically range from 25 to 50 mm in diameter, with grout slightly exceeding the bolt size to ensure proper filling. Assuming an inscribed square condition, the bolt in this study has a diameter of 28.28 mm, grouted in a hypothetical borehole with a diameter of 77 mm. For displacement monitoring, increasing the bolt diameter (19 mm to 50 mm) has been shown to reduce tunnel boundary displacement (Das and Singh, 2021). However, no specific guidelines exist for bolt and borehole sizes in the AH applications. In this study, the diameter difference between the

bolt and grout remains relatively large, though a smaller gap is preferable for efficient heating and quicker water influence detection. It was assumed that the grout would be sufficiently permeable so that the hydraulic conditions in the grout would reflect that in the rock mass.

A DFOS cable (Fujikura Ltd., Tokyo, Japan, FR-OG4ETINHE-SR15E × 4C) was used for both heating and temperature sensing, which is comprised of four single-mode fibres and two metallic wires (Fig. 17b). Our team has previously demonstrated its effectiveness for strain monitoring in landslide masses and laboratory AH experiments. Acharya and Kogure (2024) highlighted three FO sensor installation techniques within reinforcements: surface bonding, slot or groove embedment, and clamping. The first two installation techniques have been adopted in the present study. The heating cable, referred to as the H-cable, was embedded in the groove, while the temperature-sensing cables, referred to as the T-cables, were affixed to the outer surface of the frame. The T-cables were arranged along two different faces of the frame, forming two loops, loop (1) and loop (2) (Fig. 17c). The loop was formed by the fusion splice of fibres at the end. The section of the cable along loop (1) was designated as the T1-cable, while the section along loop (2) was designated as the T2-cable. The distances of the T_1- and T_2-cables from the H-cable were 7 mm and 13 mm, respectively. During installation, the cables were attached using epoxy resin while being tensioned to ensure proper placement. The resin used was an ultra-versatile, water-resistant, silylated urethane resin (SU premium hard) produced by Konishi Chemical Ind. Co., Ltd. After attaching the cable, a small force was applied to ensure an optimal coupling between the cable and the bolt, facilitating efficient heat transfer during monitoring.

The cable-instrumented frame (i.e., mock bolt) was centrally positioned within a high-strength PVC pipe, 1000 mm in length with an inner diameter of 77 mm, and cement slurry was poured in to encapsulate it. The grout used to secure the cable consisted of a mixture

of Portland cement and water with a water-to-cement (w/c) ratio of 0.45. After 48 hours, the outer PVC pipe was removed (hereinafter, the cement-grout with mock bolt is referred to as the specimen). According to the cement manufacturer, it develops strength quickly, and the compressive strength of the mortar matrix reached 39.2 N/mm² after 3 days and 70.2 N/mm² after 28 days. The AH experiments were carried out following a 21-day curing period. Notably, the section of the cable embedded within the bolt element, commonly referred to as the embedded length, was 1000 mm, while the fibre under test (FUT) measured 16 m in length. The position of the specimen was at a distance between 6.33 to 7.33 m along the FUT cable.

5.2.2 Active heating and heat transfer

Two experimental cases (case-I and case-II) were considered in this study (Table 6). In the case-I, the specimen was heated using the metallic armour of the H-cable at a constant q of 7.6 W/m for 150 minutes. The ΔT was monitored via T1- and T2-cables, and thermal response curves were generated. To simulate the effect of water along rock fractures within a grouted borehole, water was introduced at four specific sections of the specimen (marked in blue, Fig. 18a). In other words, the entire specimen was divided into higher and lower λ zones by the supply of stagnant water. A study also highlighted that the λ of the cementitious grout under air-dried conditions decreased by 15.56–38.30% as compared with the saturated condition (Kim and Oh, 2019). The water-supplied sections, in this study, referred to as enhanced-conduction dominant (ECD) zones, represent areas where heat transfer is influenced by the presence of water. Since the water remains stagnant, there is no significant advective heat transport; instead, heat transfer occurs primarily through conduction, with potential minimal infiltration-driven convection (Fig. 18b). The water-supplied sections are labelled as ECD-1, ECD-2, ECD-3, and ECD-4. Notably, ECD-2 and

ECD-3 were placed close to each other to replicate closely spaced hydraulically active fractures in a natural field. Water was supplied to ECD-2, ECD-3, and ECD-4 before heating began, while ECD-4 received water only after 90 minutes of continuous AH to simulate the sudden appearance of water in fractured zones. Note that the recorded water temperature before supplying was ~16.5 °C. Sections without stagnant water, represented in grey, consist of a mortar matrix and serve as pure conduction zones (i.e., conduction-dominant; CD) (Fig. 18c). These are labelled as CD-1, CD-2, CD-3, CD-4, and CD-5. In these regions, heat transfer is governed solely by the thermal properties of mortar.

In the second experimental scenario (case-II), the T1-cable was converted into a composite cable, meaning it functioned for both heating and sensing. The goal was to assess whether a single composite cable could effectively perform both tasks to detect water presence. The metallic armours of the T1-cable (composite) were looped to form a line heat source and heated at the same electrical power (7.6 W/m for 150 minutes). The ΔT was measured using optical fibres embedded within the same cable, while temperature measurements were also recorded using the adjacent T2-cable (d=17 mm). It is important to note that all of the experiments in this study were conducted in an open environment, rather than within rock or soil. The room temperature was maintained at 24 °C.

5.3 Experimental results

5.3.1 Thermal response (Case-I)

Figure 19 presents the spatial and temporal thermal response semblance plots along the axial length of the grouted bolt subjected to continuous AH for 150 minutes at a constant q of 7.6 W/m. The thermal distribution varies with the axial position of the bolt, primarily influenced by the presence of water, which induces localised thermal anomalies due to

increased heat conduction. The data recorded by two different fibre-optic cables, T1 (*d*: 7 mm) and T2 (*d*: 13 mm), illustrate the impact of distance from the heating cable on heat propagation and dissipation.

In Fig. 19a, the thermal response recorded using the T1-cable shows a non-uniform temperature distribution along the bolt length, with a clear influence of water infiltration. After 150 minutes of AH, the highest temperature rise (51.47 °C) was observed at 0.03 m (CD-1), while the lowest temperature (39.47 °C) was recorded at 0.75 m (ECD-4). The slower temperature rise at ECD-2, ECD-3, and ECD-4 suggests enhanced thermal dissipation due to water microcirculation. Notably, a sharp reduction in ΔT at ECD-1 after 90 minutes signifies the impact of water supply, simulating the appearance of groundwater flow through fractured rock zones in practical applications. During the initial heating phase (0–60 minutes), 52% of the total temperature rise measured by the T1-cable was achieved. In comparison, the T2-cable recorded 56% of its total rise during this same period. These percentages were calculated based on the ΔT between 60 minutes and 150 minutes and then averaged. This rapid initial rise is attributed to the early dominance of conductive heat transfer before the system approached a quasi-steady state.

The maximum temperature rise recorded by T1-cable at CD-1, CD-2, CD-3, CD-4, and CD-5 were 51.47 51.47 °C, 49.51, 42.61, 43.79, and 48.5 °C, respectively. Similarly, the maximum temperature rise recorded at ECD-2, ECD-3, and ECD-4 was 40.52, 39.94, and 39.47 °C, respectively. The trend of the temperature rise was quite different at ECD-1. The ΔT after 90 minutes was 44.53 °C. Since the water was supplied after 90 minutes, the temperature dropped and started to increase, reaching a maximum temperature rise of 47.69 °C after 150 minutes.

Similarly, Figure 19b displays the thermal response measured using the T2-cable. The larger distance from the heating cable results in slightly different heat distribution patterns, with lower peak temperatures and more gradual heat dissipation along the bolt. The maximum temperature rise recorded by T2-cable after 150 minutes of AH was 49.42 °C, recorded at 0.05 m, and the minimum temperature rise was 36.07 °C, recorded at 0.79 m. More specifically, the maximum temperature rise recorded at CD-1, CD-2, CD-3, CD-4, and CD-5 were 49.42 °C, 47.11, 40.34, 40.85, and 44.89 °C, respectively. Similarly, the maximum temperature rise recorded at ECD-2, ECD-3, and ECD-4 was 37.34, 37.41, and 36.07 °C, respectively. Regarding the ECD-1, where water was supplied after 90 minutes, the trend of ΔT was similar to that of T1-cable.

5.3.2 Trend of temperature rise (Case-II)

The temperature variation along the axial position of the bolt exhibited a non-uniform trend, as recorded by both T1- and T2-cables. Figure 20 illustrates the temporal evolution of temperature at different positions along the one-meter-long grouted mock bolt, subjected to 150 minutes of continuous AH.

In the conduction-dominant zones, the mode of heat transfer was governed primarily by thermal conduction, resulting in a steady increase in temperature. For instance, at CD-1, there was a gradual, non-linear increase in temperature, with T1-cable temperatures slightly higher than T2-cable (Fig. 20a). The region is primarily conduction-dominant with minor deviations between the two cable measurements. Similarly, at CD-3, a nearly identical temperature rise was recorded by both T1- and T2-cables, with maximum recorded temperatures of 40.7 °C and 37.49 °C, respectively (Fig. 20b). This zone, however, exhibited a lower overall temperature rise compared to other conduction zones, likely due

to water supply effects from adjacent sections (ECD-2 and ECD-3). The limited length (~5 cm) of CD-3 further constrained heat retention, influencing the observed thermal response.

In enhanced conduction-dominant zones, the temperature rise was influenced by minimal water infiltration, which altered the thermal transport mechanism. At ECD-1, a distinct thermal anomaly occurred after 90 minutes of AH, marked by a sharp drop in the temperature (Fig. 20c). The mode of heat transfer was solely conduction-dominated at the beginning; however, after 90 minutes, the effect of water supply led to enhanced conduction. This is evidenced by the drop in the temperature curves for T1- and T2-cables. Looking at another enhanced conduction zone, i.e. at ECD-4, a monotonic increase in temperature with time, showing no abrupt changes, except for slight fluctuations (Fig. 20d). The temperature rise in ECD-4 suggests an enhanced conduction-dominated heat transfer regime. Furthermore, the response of T1- and T2-cables is nearly identical, with slight temperature differences.

5.3.3 T1-cable as a composite cable (Case-II)

Figure 21 presents the results of AH experiments conducted for 150 minutes using the T1-cable as a composite cable. The heat was applied through the metallic wires of the T1-cable, while temperature monitoring was conducted using the optical fibre of the same T1-cable (composite) and the adjacent T2-cable. The T2-cable recorded a temperature rise with a clear indication of the position of water (Fig. 21a). This cable also detected the sudden supply of water at ECD-1 after 90 minutes of AH. On the other hand, the temperature distribution measured by the T1-cable (composite) displayed irregular and spatially inconsistent fluctuations, particularly around ECD-1 (Fig. 21b). Additionally, the temperature contrast between ECD-2 and ECD-3 was less distinct, making it difficult to pinpoint the exact location of water influence. The maximum temperature rise recorded

after 150 minutes by the T1-cable (composite) was 49.3 °C, which is ~40% higher than the maximum temperature recorded by the adjacent T2-cable.

5.4 Discussion and key findings of feasibility study-II

5.4.1 Technical strengths of the PNC-OFDR method

One of the key strengths of this study is the demonstration of the AH-OFDR method's effectiveness in identifying water effects within a remarkably short heating duration, i.e., less than 30 minutes with a power input of 7.6 W/m. This rapid response is a significant improvement over previous studies that required heating durations of up to 36 hours at a power input of 12 W/m in an 80 m-deep grouted borehole (Zhang et al., 2023). In their work, a low-permeability quartz sand grout (hydraulic conductivity = 5×10^{-5} m/s) was used, and DTS technology served as the monitoring system. The extended heating period in that study was guided by numerical simulations, which indicated that heating durations exceeding 5.6 hours were necessary to accurately estimate ground λ within acceptable error margins. However, such prolonged heating durations can significantly increase operational costs and limit the practical utility of the method in time-sensitive field conditions. By contrast, the AH-OFDR approach applied in the present study enables rapid identification of subsurface water effects and thermal anomalies with substantially reduced heating time and energy input. This efficiency is particularly valuable for engineering geological investigations, where time and resource optimisation are critical. However, recovery (cooling) data may still be necessary in practical applications to accurately identify water flow under ambient conditions, potentially extending the monitoring duration (Pehme et al., 2007). Moreover, the authors have successfully applied this method to estimate ground λ in a 50 m-deep cementitious grouted borehole, confirming its applicability not only for

localising groundwater but also for thermal property characterisation under realistic field conditions.

Another key strength of presented method is the 2 cm spatial resolution achieved by the PNC-OFDR sensing method. This is similar to the resolution achieved in feasibility study-II. For accurately detecting and delineating closely spaced fractures (as simulated by ECD-3 and ECD-4 in this study), a high spatial resolution that is finer than the distance between adjacent fractures is essential. Previous widely used and established methods, such as DTS, offer spatial resolutions in a meter range, which limit their ability to resolve closely spaced fractures precisely. Additionally, the presented method offers a rapid data acquisition time of 2.5 ms, compared to the significantly longer acquisition time of up to 5 minutes required by DTS (Hakala et al., 2022). This combination of high spatial resolution and rapid data collection makes the PNC-OFDR method particularly valuable for monitoring highly fractured aquifer zones where detailed, time-sensitive fracture mapping is crucial.

5.4.2 Effects of cable distance and aluminum bolt

The T1-cable, positioned closer to the H-cable, recorded slightly higher temperatures with smoother temporal profiles. In contrast, the T2-cable, located farther from the heat source, exhibited minor fluctuations and noise in time in its heating curve. This suggests that increasing the distance between the sensing cable and the heat source leads to a more diffused and less stable thermal response. The difference in maximum and minimum temperatures recorded by T1- and T2-cable were 2.05 °C and 3.4 °C, respectively. By comparing the results from T1- and T2-cable, it is evident that, although the difference is not very significant, the proximity of the sensing fibres to the heat source plays a crucial role in recorded temperature variations. More interestingly, both cables detected the

positions of supplied water with slight temperature variations. In comparison, the rate of temperature rise was much lower at water-supplied sections than in pure conduction regimes in our previous study, where both heating and sensing cables were freely embedded inside mortar using cable guides (Acharya et al., 2024). However, in this study, both cables recorded comparatively higher temperatures even at water-supplied sections, probably due to the high λ of the aluminum bolt.

The mock bolt used in this study is made of aluminum, which has a high λ of approximately 205 W/mK compared to other metals such as steel (approximately 50 W/mK). When the metallic armour of the H-cable is heated at a constant q, the generated heat rapidly transfers along the bolt, leading to faster heat transfer and higher ΔT recorded by the T1- and T2-cables. Cement grout has a much lower λ (1.45 W/mK; under saturation; in the case of both w/c and s/c ratio equal to 0.5) (Kim and Oh, 2019) than aluminum and behaves as a thermal barrier around the bolt. The rapid heat coming from the metallic armour accumulates around the bolt, leading to higher temperature readings around the sensing cables. Therefore, the temperature rise readings were relatively higher in this study as compared to the results reported by Acharya et al. (2024) due to the high λ of aluminum bolts and the low λ of cement grout.

5.4.3 Formation of *thermal halo* and detection limit

Small-aperture transmissive fractures may not be identifiable when using a coarse spatial resolution due to the presence of a *thermal halo*, a zone of thermal influence that extends beyond the actual width of the water-bearing fracture (Munn et al., 2020). Such a thermal halo forms due to the sharp ΔT caused by the effect of water. A *thermal halo* extends well beyond the actual fracture aperture, making it difficult to distinguish individual fractures accurately. Figure 22 illustrates the formation of a *thermal halo* as a result of thermal

anomalies induced by supplied water. Even in cases where water remains stagnant, the *halo* can develop, extending beyond the actual zone of supplied water. When multiple transmissive fractures are closely spaced, a coarse spatial resolution may detect the entire cooler region as a single *thermal halo*, masking the distinction between individual fractures (Maldaner et al., 2019). To resolve such closely spaced *thermal halos*, a fine spatial resolution, such as the one provided by the PNC-OFDR method employed in this study, is essential. This high-resolution approach enables the detection of discrete thermal anomalies, improving the accuracy of fracture identification. Therefore, it is important to note that the ability of the monitoring system to identify individual fractures is related to the spatial resolution of the individual monitoring unit used.

5.4.4 Effect of width of high-saturation zone on temperature change

The proposed PNC-OFDR sensing method demonstrated clear capability in detecting ECD zones with widths ranging from 5 to 13 cm. Given its fine spatial resolution, the method showed strong potential for identifying even narrower ECD zones, potentially down to ~2 cm in width. An interesting observation emerged from this study regarding the effect of the width of water-supplied sections (i.e., fracture width, l). Wider ECD sections allowed a greater volume of water to interact with the heat generated by the H-cable, facilitating more efficient heat transfer from the cable to the surrounding grout. This interaction explains the observed decrease in ΔT_{60} (temperature change after 60 minutes of AH) with increasing fracture width (Fig. 23). Conceptually, when an ECD zone is sufficiently wide, the *halo* occurs at both ends, and in between, temperature stabilises. In the present study, although the ECD widths varied, none were large enough to establish a clear central stabilisation zone. Further experiments with longer ECD intervals would be necessary to fully validate this behaviour. Under the conditions adopted in this study, the temperature measurements from the T1- and T2-cables showed only minor differences in ΔT_{60}. However, the T2-cable

exhibited a stronger correlation (R^2 = 0.99) compared to the T1-cable, indicating higher sensitivity. While the general trend of decreasing temperature with increasing water-contact area may hold true, the specific thermal response could differ in a more realistic rock bolt due to structural and material complexities.

5.4.5 Applicability of a composite cable

In AH applications, the measurement of temperature variations can be conducted using either separate heating and sensing cables or with a composite cable that incorporates both metallic wires and sensing fibres (Bense et al., 2016). In our previous works, the effectiveness of using two separate cables for locating the position of water using the OFDR sensing method was demonstrated (Acharya et al., 2024). However, there have been a large number of studies available in the literature that used a single cable for both objectives. Such a setup consists of electrically heating a FO cable through its steel armouring while continuously monitoring the elevation in temperature along the heated section using the fibres inside the cable (Simon et al., 2023). The experimental results suggest that while a composite cable can serve as a dual-purpose sensor, it showed, for a grouted bolt, limitations in clearly identifying the enhanced saturated zones, likely due to its self-heating nature affecting temperature sensing accuracy. Furthermore, it showed limitations in distinguishing finer-scale variations in water distribution (For instance, identifying closely spaced ECD-2 and ECD-3). Although the results of this study demonstrated the effectiveness of using a separate sensing cable, it underscores the need for further testing under varied structural configurations to better generalise the findings.

This study introduced a set of laboratory feasibility tests for a novel approach for qualitatively identifying high-saturation zones along a rock bolt installed in the ground using the AH-DFOS method with an optical fibre instrumented FGRB. The method utilised

the AH techniques, where thermal energy was applied along the metallic armour of an optical cable, and temperature responses were continuously monitored to detect localised thermal anomalies associated with different thermal conductivities due to variations in the hydraulic conditions. The key findings of this study are as follows:

- The AH-DFOS method, particularly the Rayleigh-based OFDR approach, demonstrates significant potential for rapidly detecting water saturation-related thermal anomalies, making it particularly advantageous for engineering geological applications where time-efficient assessments are critical.
- With a spatial resolution of 2 cm, this technique enables precise detection and delineation of closely spaced high-saturation zones. The presented method also showed potential to detect the sudden appearance of water flow due to rainfall infiltration along the fracture zones in natural field applications. Additionally, the data acquisition time of 2.5 ms represents a substantial improvement over traditional DTS methods, which often require tens of minutes for data collection**.**
- Temperature variations are influenced by the distance between the sensing fibres and the heat source. However, under the experimental conditions adopted, when sufficient q is applied, two widely spaced sensing cables (7 mm and 13 mm from the heat source) show minimal discrepancies, ensuring reliable detection. Larger distances result in slightly diffuse temperature readings, potentially affecting detection accuracy.
- While a composite cable can function as both a heating and sensing element, its self-heating nature introduces measurement uncertainties. This results in reduced accuracy in identifying enhanced saturated zones and closely spaced hydraulically active fractures. The findings indicate that using a separate sensing cable enhances spatial resolution and improves the detection of water-saturated zones. This may be specific to

the rock bolt application where the H- and T-cables are attached to the metallic bolt, which would require further study.

- At the location of high-saturated zones, a *thermal halo* forms on either side of the zone. Detecting closely spaced high-saturation zones and their corresponding *thermal halos* requires fine spatial resolution, such as that provided by the PNC-OFDR method employed in this study.
- The rate of ΔT decreases as the width of the high saturation zones increases, since a wider saturated zone allows a greater volume of water to interact with and dissipate the heat generated by the heat source by creating a temperature-stabilised zone.

The integration of AH-DFOS technology with a mock FGRB presented a promising approach for locating high saturation zones and transmissive fractures. This method has significant practical implications for geotechnical applications, including slope stability assessment, tunnelling, foundation monitoring, and dam reinforcement, where rock bolts are commonly employed as stabilising structures. Future research could focus on optimising the thermal properties of cement grout, the use of more realistic steel bolts, and enhancing data interpretation techniques to further improve the accuracy and reliability of this method.

CHAPTER VI FIELD DEMONSTRATION

6.1 Background

Characterising groundwater flow by the heat tracing method is important to investigate subsurface flow processes and assess the environmental risks. Numerous tools and techniques have been developed and utilised for the characterisation of hydrogeology. Despite the great amount of previous work based on AH-DFOS, the information on groundwater dynamics in highly fractured rock remains sparse and highly uncertain. There has been only one study to our knowledge reporting the application of the AH-DFOS method in low-permeability fractured media at the Grimsel Test Site in Switzerland (Klepikova et al., 2022). This highlights a critical need for further field investigations to better characterise flow and heat transport processes in such complex geological environments. Moreover, the reliability of using separately installed fibre-optic cables, freely grouted within deep boreholes for independent heating and temperature sensing, remains uncertain. To address these gaps, this study explores the integration of phase noise-compensated optical frequency-domain reflectometry (PNC-OFDR) with AH to investigate a highly fractured turbiditic rock formation under the ambient flow conditions. Temperature-depth profiles were derived from the thermal response to controlled ground heating, enabling the identification of water-bearing fracture zones and providing new insights into subsurface hydrogeological behaviour. This work is an extension of the previous two feasibility experiments presented.

6.2 Experimental methods

6.2.1 Research site and instrumentation

According to the existing material (1:50,000 geological map of "Sakaiminato" by Geological Survey of Japan, 1995), the investigated borehole (depth: 50 m and diameter: 66 mm) site is located in the Josoji Formation near mt. Misaka (latitude: 35°32'15.20"/longitude: 133°6'10.42"), in Shimane Peninsula, southwest Japan (Fig. 24a). The altitude of the borehole location is 487.34 m a.s.l., situated 15 m below the main ridge of the Mountain. The Formation was deposited during the Miocene period (17.65–16.39 million years ago) (Nomura, 2021) and characterised by the submarine slumping deposits consisting of sandstone and mudstone (Kano et al., 1991). Moreover, within the Formation, rhyolite and andesite volcanic rocks are also distributed, supporting the role of volcanic activities and hydrothermal alterations in the Shimane Peninsula during the formation of the Japan Sea (Kano et al., 1991).

Borehole cores provide a means for directly observing rock fractures, joints, and other discontinuities. In the AH-DFOS technique, a fine-scale description of the vertical core is necessary to identify the fractured zones that are responsible for the temperature anomalies during AH. Therefore, a comprehensive stratigraphic column was prepared to scrutinise the cores in detail (Fig. 24b). Thin to thick-bedded and slightly to highly weathered shale is the dominant lithofacies in the core, which has the highest net to gross of all cores (~50%). Within this dominant facies, intensely fractured zones (naturally fractured) that are hydraulically most important were identified. Additionally, thin to massive (thickness up to 1.7 m) non-stratified and less fractured sandstone layers are amalgamated with the dominant lithofacies along the core (especially between 30-45 m), with commonly sharp bed contacts. Sandstones are fine to coarse sand with an upward fining trend, internally

structureless, and poorly sorted. Such massive deposition indicates rapid and turbulent deposition from suspension. Thin bands of rhyolitic tuffs (thickness upto 5 cm) sandwiched between other pronounced lithofacies are also present. These lithofacies are distributed especially in the upper section of the core. These bands are believed to have been deposited from the eruption of volcanic ash or pyroclastic materials, transported due to turbidity currents, rapid burry and compaction by the overlying sediments.

In the uppermost shallow horizon, up to approximately 5 m-deep, the material is highly unconsolidated and retrieved mainly as rock fragments or short columnar cores. From a depth of 7.10 m onwards, the material exhibits a more prominent yellowish-grey colouration and transitions to a predominantly flaky to fragmented texture. A highly weathered zone is observed between 9.50 m and 11.10 m, where the material becomes distinctly flaky. At 16.50 m, clay infilling is observed along fracture surfaces, and interbedded clay with a yellowish-brown hue becomes apparent around 22.25 m. At approximately 25 m depth, groundwater inflow was encountered at a moderate intensity. Bedding-plane (horizontal) fractures are notably developed between 15.10 m and 25.75 m, whereas below this interval, the recovered core appears relatively fresh, suggesting reduced weathering. An intensely weathered zone occurs between 35.25 m and 35.45 m, characterised by a sandy, flaky texture with clay admixture. Flaky material persists between 35.88 m and 36.00 m. Vertical fractures with yellowish-brown staining were identified between 41.65–42.45 m and 43.75–44.45 m, while clay infilling along lithologic boundaries is noted at 44.58 m. The material becomes slightly flaky around 48.20 m. Notably, the tuffaceous rock units show fewer fractures compared to the mudstone intervals, which exhibit abundant fracturing, suggesting lithological control on fracture development.

The present study employed two different types of optical cables described in Table 2. The H-cable was the composite buffered cable (FR Fujikura cable), and the T-cable was the loose-tube gel-filled picocable. The same Fujikura cable was installed for strain sensing purposes. Two sets of H-, S-, and T-cables (i.e., H_1- and H_2-cables, S_1- and S_2-cables, and T_1- and T_2-cables) were prepared to be installed into the borehole. Among the two sets, only one set of cables (i.e., H_1-, S_1-, and T_1-cables) were connected to the heating and sensing system and the other set was not connected in case the previous set cannot provide good-quality data. Since this study focused on AH experiments, the data recorded by S-cables are not described.

Figure 25a shows the borehole configuration, including the position of cables to be installed inside the borehole. Figure 25b-d illustrates the detailed procedures of installing optical cables inside the borehole and the grouting method. Two cable guides, which are highly resistant against corrosion and impact, having six small holes in them, were used to properly align the cables. During installation, VP-20 pipes were inserted inside the guides so as to vertically install the cables. Tensile stress was applied to the cable to provide pretensioning at that moment. The use of grouted data is highly recommended for characterising natural flow system conditions, for determining accurate distribution of fluxes, and for improved depth resolution (Coleman et al., 2015). In this study, the borehole was permanently sealed with cement grout with a w/c ratio of 1:4 to prevent vertical flow within the borehole and to reestablish the natural flow conditions around the borehole.

All opto-electronic components were kept inside a container house at the ground surface. The FO cables ran from the container house to the surface of the borehole location and then to the bottom of the deep borehole, and then returned up to the container house again. The whole length of the cable was approximately 360 m. To protect cables from the container house to the top of the borehole, all cables were put inside a hard synthetic resin

cable protection pipe, which is flexible, easy to handle and has high mechanical strength, and then laid on the ground surface. After one month of stabilisation period, while well construction was completed, the PNC-OFDR sensing assembly was deployed in situ. The instruments were set in a container on the ground surface.

The electrical heating of the metallic armour in the H-cable was performed using a Takasago DC generating device described in section 3.3. The AH experiments were carried out using different electrical powers at different times. This study employs the same PNC-OFDR sensing method used in previous feasibility studies for distributed temperature sensing. We have selected a spatial resolution of 5 cm and a temperature resolution of 0.01 °C for this field monitoring.

6.2.2 Meteorological conditions at the study site

The meteorological conditions at the study site throughout 2024 are presented in Fig. 26, highlighting the daily variations in maximum, minimum, and average air temperatures, as well as 24-hour rainfall measurements. The data were retrieved from the Matsue observatory station of the automated meteorological data acquisition system (AMeDAS) run by Japan meteorological agency (JMA). The total monthly rainfall is indicated at the bottom, highlighting the major rainy periods (June–July and October–November) shaded in light blue. The timing of AH experiments is marked along the top axis. Notably, AH experiments conducted before and after the first major rainy period (i.e., May 29 and July 25) provide valuable insights into the thermal and hydraulic responses of the subsurface to pre- and post-rainfall conditions.

Figure 27 compares daily weather conditions for June 2024 and June 2025, during which targeted AH tests were conducted. The results of AH experiments carried out on these two different times are expected to provide insight into the long-term weather

influences on experimental outcomes. In June 2024 (Fig. 27a), the site received 225.5 mm of rainfall, with a notable heavy rainfall event (~95 mm) occurring just one week before the AH test on June 30. This likely resulted in increased rock moisture and groundwater flux, which would have enhanced convective heat transfer during the experiment. In contrast, June 2025 (Fig. 27b) recorded lower total precipitation (162 mm), with fewer and more dispersed rainfall events prior to the AH conducted on June 27.

6.2.3 Determination of physical and mechanical properties of rock cores

Thirty-nine cylindrical specimens were prepared from depths of 30 m to 42 m since this horizon has a rock quality designation (RQD) value ranging from 56.8 % to 90%. All the specimens underwent water saturation in a vacuum chamber, and their weight changes were continuously monitored until a constant weight was achieved. After full saturation, the specimens were carefully surface-dried using a moist cloth so that only surface water was removed and no fragments were lost. The specimens were then weighed to obtain the mass and saturated density of the specimens in the saturated conditions. The P-wave velocity (V_p) was measured immediately to avoid water evaporation. The specimens were placed inside the oven at a temperature of 105 °C for 48 hours, and the specimens were cooled in a desiccator for 30 minutes. The oven-dried specimens were then weighed to obtain the mass and density (ρ_{dry}) of the specimens.

The water absorption (w) was obtained by calculating the difference between the weights at saturated and dry states. Specific gravity (G_s) for all specimens was determined using powder specimens (pycnometer method) according to the Japanese Industrial Standards (JIS) A 1202 (JSA, 2020). Void ratio (e) and porosity (ϕ) were also calculated by using the following equations:

$$e = \frac{G_s \times \gamma_w}{\gamma_d} - 1 \quad (9)$$

$$\phi = \frac{e}{1+e} \times 100 \quad (10)$$

where γ_w is the unit weight of water, and γ_d is the dry unit weight of the specimens.

The V_p at room temperature and ambient pressure was measured on all thirty-nine specimens under fully saturated and dry (air-dry and oven-dry) states using Sonic Scope developed by Marui and Co., Ltd., Japan. The ultrasonic frequencies of 50 kHz were employed, with a reading accuracy of ±0.1 μsec, following the standard described in ASTM C597-16 (ASTM, 2023a). P-wave travel times (Δt) were recorded three times for a specimen by rotating it, and velocity was determined with a predefined specimen length (H) ($V_p = H/\Delta t$). The measured V_p values were classified based on the ANON's classification.

The *UCS* test followed the standard defined by the ASTM-D2938-95 (ASTM, 2017) using a loading machine with a loading capacity of 600 kN and a constant loading rate of 0.20 kN/s. A total of 15 specimens were examined under dry conditions, while 16 specimens were tested under full saturation. Out of 15 dried specimens, 13 specimens underwent *UCS* testing. Unfortunately, we encountered technical issues with the strain gauge during the *UCS* tests of two dried specimens (A7 and A36), which prevented us from obtaining deformation data. Nevertheless, we were able to record the peak compressive strength in these cases. For those specimens whose length-to-diameter ratio was not on the order of two, *USC* was corrected for standardising those non-standard sizes defined by the ASTM-D2938-79. The tangent Young's modulus obtained from the *UCS* test is the static elastic modulus (E_{static}). Moreover, eight samples were analysed for the *BTS* test and equally divided into two groups for testing under fully saturated and dry states. The planar loading platen established by the ASTM D3967-16 and ISRM 2018 was utilised (ASTM, 2023b;

ISRM, 2018). *BTS* tests were carried out using the same loading machine used to determine *UCS*.

6.2.4 Calculation of thermal conductivity

a) Effective thermal conductivity

In the AH-DFOS sensing method, conductive heat transfers through the rock matrix and forced convective heat transfers from advection through fractures. Therefore, knowing the effective thermal conductivity of the rock, λ_r, is essential. Lab measurements were made on eight specimens taken from a depth between 32 to 40 m to develop a baseline profile of λ_r, which defines the condition with no groundwater flow but minimal infiltration. The λ_r was determined using the transient heat pulse method based on the line-source theory using a TEMPOS thermal properties analyser (TTPA) (METER Group, Inc., Pullman, WA, USA) following ASTM 5334-22 (ASTM, 2022) (Fig. 28). An RK-3 sensor (60 mm in length and 3.9 mm in diameter) designed for rocks was used to obtain λ_r within ten minutes after inserting the sensor into rock cores. The ϕ of the studied specimens, measured using the pycnometer tests, was generally low and ranges from 0.24 to 6.33%, with an average of 2.82%.

b) Apparent thermal conductivity

The apparent thermal conductivity (λ_a) across various layers inside the borehole was calculated using AH-DFOS thermal response, which suggests the vertical heterogeneity of the geological media (Maldaner et al., 2019). The geometry of the AH-DFOS sensing method in a grouted borehole can be approximated as a continuous line source problem that allows the estimation of λ_a along the borehole. The q=9.4 W/mK was selected to determine λ_a , which is in the range suggested by (Hakala et al., 2022). After a sufficiently long time

of heating, the rise in cable temperature, plotted as a function time, will approach an asymptotic straight line with slope. The λ_a can be calculated from that slope (Munn et al., 2020):

$$\lambda_{\mathrm{a}}=\frac{q}{4\pi m} \tag{11}$$

where q (W/m) represents the heat input per unit length of the H-cable and m denotes the temperature vs. natural logarithm of time plot. To calculate the λ_a, the slope of a linear regression line through all of the data points was used rather than simply the difference between the start and end temperature of the test. We calculated λ_a for each sampling interval (i.e., 0.05 m spatial resolution) along the length of the borehole. The recovery data after ceasing the heat are much less noisy than the heating data and yield more consistent estimates of λ_a (Pehme et al., 2007). Therefore, λ_a was calculated using recovery data.

6.3 Results

6.3.1 Physico-mechanical and thermal parameters of rock cores

The average saturated density (ρ_{sat}) of the studied core specimens was 2.64 g/cm³. The value of ρ_{sat} varied, with the lowest recorded at 2.61 g/cm³ and the highest at 2.69 g/cm³, with a standard deviation of 0.02. Similarly, the dry density (ρ_{dry}) ranged from 2.56 g/cm³ to 2.67 g/cm³, with an average value of 2.62 g/cm³ and a standard deviation of 0.03. The w of the studied sandstone rocks ranged from 0.52 to 1.80%, with a mean value of 1.00%. The G_{s} values range from 2.62 to 2.81, with an average value of 2.70. The ϕ of the studied specimens is generally low and ranges from 0.24 to 6.33%, with an average of 2.82%. Moreover, the void ratio is relatively low, ranging from 0.03 to 0.07 (Table 7). This means that the specimens are characterised by their low permeability and limited ability to transmit

fluids due to the presence of clay minerals and tiny pore spaces that represent a higher degree of compaction and cementation.

The saturated V_p (V_{psat}) values range from 4.59 to 5.52 km/s with an average value of 5.01 km/s, while the values of V_p in a dry state, V_{pdry}, fall between 4.45 and 5.35 km/s with an average value of 4.85 km/s (Table 7). It is evident from the data that the V_{psat} is 1.02-1.09 times the V_{pdry}. These V_p values are higher than those of typical sandstones, in general, and fall in the "*high*" and "*very high*" classes in ANON's P-wave classification. Specifically, under saturated conditions, 55% of specimens (n=11) were classified as "*high*" and 45% of specimens (n=9) as "*very high*" in V_p. Likewise, in dry conditions, 74% of specimens (n=14) fall into the "*high*" category, and 26% of specimens (n=5) fall into the "*very high*" category of V_p. The data reveal that V_p is higher in the presence of water saturation compared to when the rock is dry. To assess the relationship between saturated and dry conditions, approximate equations were established between ρ_{sat} and ρ_{dry}, and V_{pdry} and V_{psat}, revealing a strong positive correlation.

For saturated specimens, the *UCS* varied between 103.77 and 206.96 MPa, with an average value of 150.28 MPa. Similarly, this range was between 109.00 to 246.11 MPa for dry specimens with an average of 191.68 MPa. The overall dataset shows that the UCS_{dry} was higher than UCS_{sat}. The static E_{static} was calculated in this study from the stress-strain diagram (Fig. 29). For saturated conditions, $E_{staticsat}$ ranged between 14.9 to 25.84 GPa with an average value of 20.63 GPa. For dry conditions, $E_{staticdry}$ ranged between 12.1 to 29.06 GPa with an average value of 24.18 GPa. A plot of $E_{staticsat}$ against UCS_{sat} and $E_{staticdry}$ against UCS_{dry} showed that they were moderately correlated with an R^2 value of 0.59 and 0.54, respectively (Fig. 30a and b). The data on V_{psat} viewed against UCS_{sat} indicates a slight scatter in the results but with a definite increasing trend (i.e., R^2=0.32) (Fig. 30c). However,

in the dry condition, data points are highly scattered like a cloud of points with no correlation (Fig. 30d).

The *BTS* values for specimens under full saturation ranged from 6.62 to 6.93 MPa with a mean value of 6.79 MPa, whereas the dried specimens exhibited a slightly wider range spanning from 7.67 to 12.57 MPa with a mean value of 10.12 MPa. Figure 31 presents a graphical representation of the interrelationship between V_p and *BTS* of specimens. Employing the power law function, V_p correlated with *BTS* under saturated and dry conditions. Although the number of data points was limited, notably, both scenarios demonstrated a pronounced strong positive correlation with R^2 values amounted to 0.95 and 0.97 under saturated and dry conditions, respectively.

The results of transient heat pulse method indicate that the average λ_r of the specimens under saturated, air-dried, and oven-dried conditions are 2.66 (2.58-2.86) W/mK, 2.31 (2.18-2.37) W/mK, and 2.23 (2.09-2.32) W/mK, respectively (Fig. 32). The λ_r values decreased by 9.45-17.23% in air-dried conditions and by 13.92-19.03% in oven-dried conditions compared to saturated conditions. Although there is a minor difference between air-dried and oven-dried λ_r (i.e., 0.078 W/mK), the difference between fully saturated and oven-dried λ_r is comparatively high (i.e., 0.429 W/mK). The results depict variations in λ_r depending on the moisture content, suggesting the need for careful consideration of these factors in thermal analysis studies.

6.3.2 Spatio-temporal thermal response along the borehole

The heating curves resulted in a set vertically distributed along the deep borehole. Since the cable was installed in a "*U*" shape and the acquisition configuration ("duplexed") allowed for forward and reverse data, two heating curves are available per monitoring location. However, only the results from forward data are presented here. Figure 33a

illustrates the spatio-temporal thermal response over depth and time collected over 6 hours monitoring period under natural gradient conditions. The x-axis represents heating time in minutes, with two distinct phases: the heating phase (0–180 minutes) and the recovery phase (180–360 minutes). One of the interesting results found was the highly variable ΔT during the heating phase as compared to the recovery phase (Fig. 33b), which might have been generated due to three effects: (a) active groundwater flow, or (b) variable moisture content, or (c) non-unifrom cable alignment. Therefore, with the combination of a smoother thermal response curve from the recovery phase and a variable curve of the heating phase, numerous zones of accelerated heat dissipation were identified.

With a constant heat input (9.4 W/mK) into the grouted fractured aquifer system, thermal response at each depth was observed to be governed by conduction and convection. Low temperature zones detected by AH-DFOS likely result from active groundwater flow in a single fracture or group of fractures, which accelerates heat dissipation. High-temperature zones correspond to low transmissivity or pure conduction regions. Given the strong surface influence, data above 1.2 m were excluded from analysis to avoid anomalies caused by the fluctuations in surface temperatures of near-surface sediments (Selker and Selker, 2018; Zhang et al., 2023). A recent study has also shown that the seasonal influence on temperature variations could be up to tens of meters (Violante et al., 2024).

After 3 hours of AH, the maximum ΔT of 26.7 °C was recorded at a depth of 47.67 m, and the minimum ΔT of 3.7 °C was recorded at a depth of 3.57 m. A closer examination of both the heating and recovery data reveals that low-temperature zones can be categorised into two types: (i) water flow zones, characterised by rapid groundwater movement, and (ii) high-saturation zones, associated with elevated moisture content. Several thin and closely spaced hydraulically active zones were identified using a 5 cm spatial resolution of

the PNC-OFDR sensing method. However, only selected major water flows and high-saturation zones are described in Table 8.

The rate of temperature increase also varied across these zones due to differences in heat dissipation. For example, in a water flow zone at a depth of 8.97 m, the average temperature increase over the 3-hours heating period was 0.64 °C. Similarly, at another water flow zone located at 39.47 m, the rate was 0.78 °C. In contrast, in high-saturation zones, the temperature rose slightly more, for instance, 0.82 °C at 6.47 m and 0.91 °C at 20.67 m. In regions unaffected by groundwater movement, the rate of temperature rise was notably higher. At a depth of 26.67 m, for instance, the temperature increased at a rate of 1.02 °C. This indicates that in such zones, heat transfer is predominantly governed by conduction through the grout material, with minimal influence from advective heat loss due to water movement.

A preferential low-temperature zone between 2 and 7.3 m is attributed to higher moisture content within loose surface sediments, as reported by Zhang et al. (2023). From 10.77 to 11.52 m, a transition to gravel and soil-like material marks the high-saturation zone. A distinct cooler zone observed between 21.07 and 25.47 m during the recovery phase suggests enhanced convective heat transfer within highly fractured sandy shale, as confirmed by core sample analysis. Between 31.32 and 35 m, stratified low heat dissipation zones were identified, and the recovery data revealed the presence of six distinct water-flow zones, each associated with accelerated heat loss. When there is a set of fractures, it enhances the ability to transfer heat away from the borehole, as highlighted by Maldaner et al. (2019). Additionally, several vertically distributed warm bands, characterised by significantly elevated temperature responses, were observed, especially below 26 m. Among them, four prominent warmer zones at depths of 34.92, 45.72, 46.67, and 47.67 m

showed maximum temperature increases of 24.7°C, 25.1°C, 25.3°C, and 26.7°C, respectively. These zones are predominantly composed of hard sandstone and less fractured shale. The elevated temperatures in these regions may have resulted due to the proximity of H- and T-cable. Such elevated temperatures can be expected during AH experiments when cables are freely embedded inside the grout, as evidenced from our previous study (Acharya et al., 2024). In such cases, the close spacing of the two cables can result in higher apparent temperatures during the heating phase; however, a rapid temperature decline may occur during the recovery phase in the presence of water flow or high moisture content.

6.3.3 Changes in flow field in response to localized recharge

Figure 34 presents a comparative analysis of subsurface ΔT over time during two AH-DFOS heating events conducted on May 29, 2024 and July 25, 2024. Between these two dates, the site experienced 569 mm of cumulative rainfall, while in the three weeks leading up to May 29, only 89 mm of rainfall was recorded (see Fig. 26). In Fig. 34 (a), the May 29 results showed a relatively stratified pattern of ΔT with well-defined warmer and cooler zones. Most depths exhibit a steady increase in temperature with time, and several thermal barriers or conductive layers appear as horizontal transitions. In contrast, Fig. 34 (b), from July 25, highlights distinct changes in the thermal behavior of the subsurface. An increased thermal dissipation was observed between 21 and 26 m (marked by a dashed ellipse), indicating increased moisture effect in that interval. Below this, at approximately 27 and 38 m depth, a new water-flow zone is inferred due to the sudden appearance of cooler response, which was less evident in the the result of May 29. Additionally, near the bottom of the borehole around 45.5 m, a widening of cooler zones is seen, possibly seasonal saturation effects in deeper fractured Shale formations.

6.3.4 Long-term hydraulic change effects on temperature rise

The monitoring results of both times showed a similar kind of stratified thermal response except at a few depths (Fig. 35a and b). The appearance and widening of water-affected zones can be seen at specific intervals. For instance, at depths of approximately 16, 30, 36, and 41 m, the results from June 27, 2025, revealed slightly wider cooler zones, which might be attributed to increased moisture content or the influence of vertical groundwater flow. At a depth of 46 m, the June 30, 2024, result indicated a water flow zone characterized by high heat dissipation, which was absent in the later 2025 measurement. These observations suggest a dynamic redistribution of subsurface water, where some previously active zones may have dried out or experienced reduced flow, while others became more saturated. This change indicates increased hydraulic connectivity and groundwater level change, likely driven by seasonal recharge or evolving saturation patterns within the fractured formation. The depth-wise ΔT line profiles on the right (Fig. 35c and d) further support this interpretation, showing more pronounced fluctuations in the June 30, 2024 data, while the 2025 profile appears smoother and generally lower in ΔT values. Overall, the results reveal a notable shift in subsurface moisture dynamics over the year, demonstrating the capability of AH-DFOS to capture subtle but significant changes in groundwater behavior and fracture-controlled flow pathways.

Figure 36 illustrates the seasonal effects on temperature measurements obtained using AH-DFOS throughout 2024 (January to December). The detailed metereological data can be seen in Fig. 26. The lower diagram presents a thermal response heat map showing the variation of ΔT recorded after 120 minutes of AH with depth and time.

The changing ΔT patterns throughout time clearly showed the seasonal influence. Because of surface temperature buffering, shallow zones (0–10 m) often showed fairly

constant ΔT values, with somewhat higher values in September. On July 25, the highest measured ΔT at shallow depth was 29.3 °C at 8 m. On the other hand, the deeper and mid-depth zones (particularly those between 30 and 47 m) exhibit more noticeable temporal fluctuations, which could be due to seasonal recharge effects, or variations in groundwater flow. Notably, some zones exhibit consistently high or low ΔT values, indicating either persistent hydraulic features or lithological control at those levels.

The top diagram further supports this interpretation by showing ΔT trends over time at selected depths (23.95 m, 31.16 m, 45.91 m, and 47.65 m). For instance, the high and stable ΔT at 47.65 m implies a dry or low-permeability zone with minimal seasonal variation, whereas the more fluctuating trend at 45.91 m may indicate seasonal groundwater flow or heat advection. Together, the result effectively demonstrates how seasonal recharge and subsurface properties jointly influence thermal responses captured by AH-DFOS, providing valuable insights for hydrogeological characterization.

6.3.5 Effective thermal conductivity

The results of laboratory measurements showed that the average λ_r of the core specimens was 2.66 W/mK, ranging from 2.58 to 2.86 W/mK. This represents the baseline value when heat transfer occurs by enhanced conduction only (i.e., no water flow but minimal infiltration). The detailed thermal conductivity determined from AH-DFOS measurements during the recovery phase, i.e., λ_a, is shown in Fig. 37. The maximum and minimum λ_a values calculated for the entire borehole depth using Eq. (11) are 7.70 and 1.51 W/mK, respectively, with an average value of 3.38 W/mK. Since λ_r values were measured using core specimens from a depth between 32 to 40 m, the average λ_a value was determined from the same depth range for comparison. The result showed an average λ_a value of 2.70 W/mK, demonstrating agreement with the laboratory-measured λ_r values (an average of 2.66

W/mK), although there were a limited number of data points (Table 7). Two core specimens showed slightly higher values than the AH-DFOS values, which might be attributed to the buoyancy-driven natural convective heat transfer in the drill hole. The anisotropy of rock core specimens might also have affected the λ_r. This consistency confirms the reliability of the AH-DFOS method for in-situ thermal characterisation of the rock mass. A comparison between the AH-DFOS-measured and laboratory-measured λ values showed the proximity of data points to the 1:1 line, further validating the accuracy of the AH-DFOS approach (Fig. 38). The results further indicate minor variations across different depths, with slightly higher thermal conductivity values observed in shale layers. This variation may be attributed to differences in mineralogical composition, ϕ, and grain size, which can subtly affect the conductive heat transfer properties of the rocks. Similar to the results reported by Maldaner et al. (2019), in our case as well, the ϕ may have a lesser influence than mineralogy because of the specimen`s low ϕ and heterogeneity.

6.4 Discussions

6.4.1 Performance highlights of the AH-OFDR method

One of the key strengths of this study is the demonstration of the AH-DFOS method's effectiveness in identifying saturation zones in a deep borehole under ambient conditions within a remarkably short monitoring period (right after 20 minutes of 3 hours-long heating ceased) with a q of 9.4 W/m. This rapid response is a significant improvement over previous studies that required extended heating times, ranging from 10 hours to 96 hours, even with comparable q of 7.5 W/m (Hakala et al., 2022). Test duration for AH experiments has become an unexpectedly controversial subject since some previous authors recommended sufficiently long heating durations to get sufficient accuracy. Such longer heating durations mean an additional cost. Therefore, the rapid detection of thermal anomalies presented in

this study is particularly advantageous for engineering geological field applications where minimising operational time is crucial. However, it is important to note that such technical parameters may vary according to the specific test site conditions and largely depend upon several factors such as borehole geometry, fracture distribution, and lithological heterogeneity. Although previous studies have used an extended heating period, they lack the discussion of thermal interference from surrounding structures, which might lead to potential signal degradation. Therefore, the shorter heating period used in this study reduces thermal diffusion effects, allowing more localised detection of active fractures by limiting the spread of heat into the surrounding medium.

Another key strength of field demonstration is the 5 cm spatial resolution achieved by the PNC-OFDR sensing method. For accurately detecting and delineating closely spaced transmissive fractures, a high spatial resolution that is finer than the distance between adjacent fractures is essential (Munn et al., 2020). Previous widely used and established methods, such as DTS, offer spatial resolutions in a meter range, which limit their ability to resolve closely spaced fractures precisely (Bense et al., 2016). Additionally, the presented method offers a rapid data acquisition time of 2.5 ms, compared to the significantly longer acquisition time of up to 5 minutes required by DTS (Hakala et al., 2022). This combination of high spatial resolution and rapid data collection makes the PNC-OFDR method particularly valuable for monitoring highly fractured aquifer zones where detailed, time-sensitive fracture mapping is crucial.

6.4.2 Analysis of spatio-temporal thermal response

The visual examination of thermal response plots generated from AH experiments provides qualitative insights as to what discrete fractured zones are hydraullically active (Coleman et al., 2015; Munn et al., 2020). The results presented in this study also demonstrated the

effect of active groundwater flow and high-saturation zones on temperature rise. The natural gradient fracture flow is highly variable throughout the bedrock aquifer, with the bulk of the ambient fracture flow occurring in the upper sequence at transmissive fractures.

Below a 15 m depth of borehole (excluding upper shallow loose and highly fractured layers), approximately 291 fractures were identified in the rock cores, indicating 6.4 fractures per meter. It further shows a mean fracture spacing of ~15.6 cm. Out of 291 fractures, only 25% fractures are found to be hydraulically active as indicated by the thermal response of the recovery phase. This suggests that groundwater flow, while variable, is likely distributed throughout the borehole rather than concentrated in isolated fracture zones. The high spatial resolution (5 cm) of the PNC-OFDR sensing method enables to resolve of discrete fracture flow and the detection of groundwater movement within densely fractured zones, making it a valuable tool for characterising subsurface hydrodynamics. Although the drilled cores, in some sections, show no indication of open fractures, the results of AH provided evidence of the presence of small fractures or fracture-prone zones. For instance, from 39 to 40 m, there is only one fracture found in the core within the sandstone. However, three high heat dissipation zones are identified in the recovery profiles, which might be due to the occurrence of thin seams of secondary ϕ (vuggy or permeable seams) (Fig. 39). Such porous layers alter heat conduction during AH experiments, allowing the method to detect even subtle variations. Therefore, future studies should also focus on the presence of porous microfractures and secondary ϕ. From Fig. 39, it is further evident that while highly fractured, not all fractures are hydraulically active, aligning with previous findings that transmissive fractures do not always support groundwater flow under natural conditions (Munn et al., 2020). For instance, at 44.6 m, there is a clearly visible fracture zone filled with yellowish clay (10YR 8/6 category according to Munsell color system) as observed in the drilled core.

In this study, the effect of the cable materials and the surrounding installation on the heat transport and temperature curves measured by the T-cable is neglected. Del Val et al. (2021) also mentioned that in the case of the use of separate heating and sensing cables, this effect is negligible. However, it becomes important when dealing with a single heating and sensing line. Our feasibility study-II on DFOS cable-instrumented fully grouted bolt monitoring also raises questions regarding the use of a composite cable for detecting the high-saturation zones. Moreover, the effect of a grouted borehole on strata flow is neglected. Such a negligible effect of grouted borehole on AH applications was also reported by Zhang et al. (2023).

At the zone of active groundwater flow, the temperature profile typically showed a convex pattern (due to the effect of *thermal halo*). The formation of such halos due to high saturation was also described in feasibility study-II, where stagnant water was introduced along the specific position of a grouted bolt and ΔT was monitored using the OFDR method.

The trend of temperature rise and decline during heating and recovery phases is demonstrated in Fig. 40. The heating curves followed a positive exponential trend approaching a maximum limit. The temperature rise over the 180-minute heating period exhibited three distinct phases: rapid, moderate, and gentle. During the initial phase (0–60 minutes), a rapid increase in temperature was observed, likely due to the initial thermal gradient and strong heat conduction from the heater to the surrounding medium. Between 60 and 120 minutes, the temperature continued to increase at a moderate rate, indicating ongoing heat diffusion into the surrounding material. In the final phase (120–180 minutes), the rate of increase became gentle, suggesting a gradual approach to thermal equilibrium. Heating was terminated at 180 minutes, after which the system was allowed to cool under ambient conditions. After terminating heat, the temperature decreases over time, initially dropping faster, then slowing down. The recovery curves followed a negative exponential

decay trend. Nearly 53% of the maximum temperature was decreased within 20 minutes of recovery. Figure 40 further depicts that the ΔT did not come to its original state (i.e., zero) even after 180 minutes of cooling.

6.4.3 Borehole grout and relative cable positions

This study highlights the effectiveness of borehole cementitious grouting for AH applications. The heating curves exhibited no signs of non-lateral water movement (i.e., vertical flow), a common issue in open boreholes (Coleman et al., 2015; Munn et al., 2020). The complete grouting of the borehole likely facilitated optimal coupling between the sensing cables, grout, and surrounding rock, effectively minimising vertical flow interference and preserving the integrity of lateral thermal profiles. Additionally, grouting may have helped restore the natural groundwater gradient, as previously suggested by Selker and Selker (2018). The effectiveness of using permanent cementitious grout can be highlighted to seal the borehole as compared to the sealing with liners, which could make the installation and removal of liners in poorly consolidated rock or unstable boreholes problematic, as reported by Munn et al. (2020). Although recent work suggests a negligible impact of grouted boreholes on strata flow (Zhang et al., 2023), they may overlook critical differences in hydraulic conductivity between grout and the surrounding rock. Addressing these variations is essential for accurate, quantitative assessments of subsurface water flow rates.

The λ of cement mortar with a w/c of 0.50 under natural conditions is 2.67 W/mK (Stolarska and Strzałkowski, 2020). This similarity suggests that the grout used in the borehole behaves thermally similar to the surrounding rock (the average λ_r value is 2.66 W/mK for shaley sandstone in this study), thereby justifying the assumption that the heat

source in the AH-DFOS measurements can be treated as being embedded within a homogeneous rock mass.

One inherent challenge with the AH method is the uncertainty in the precise relative positioning of installed cables (H- and T-cables) within the borehole. This can lead to inconsistent temperature readings, with some measurements registering anomalously high values due to cable overlap, while others may underestimate temperatures. Similar inconsistencies were observed in our previous study (Acharya et al., 2024). To improve the reliability of flow zone identification, monitoring temperature decline during the recovery phase can provide valuable insights. A promising solution to mitigate temperature measurement inconsistencies is the parallel embedment of H- and T-cables as demonstrated in the feasibility study-II. However, implementing parallel cable embedment in deep borehole monitoring presents significant technical challenges.

6.4.4 Need for recovery data

Figure 41 illustrates the evolution of temperature during a 3-hours heating period followed by a 3-hours recovery (cooling) period within the 2-meter bottom section of the borehole (48–50 m depth). The thermal response curves during heating (Fig. 41a) exhibit significant noise that increases over time. In contrast, the cooling phase (Fig. 41b) shows a much smoother trend with decreasing noise, consistent with observations reported by Pehme et al. (2007).

As mentioned earlier, the relative position between H- and T-cables inside the grout was uncertain. Since AH-OFDR temperature measurements are highly sensitive to the spacing between these cables, the resulting heating data can be inconsistent. Consequently, several studies have recommended using cooling (recovery) data instead for characterising groundwater flow (Freifeld et al., 2008; Hakala et al., 2022). Additionally, if λ is inferred

from the heating phase, it may lead to significant discrepancies, even within the same borehole section, due to the variability introduced by cable positioning. The λ_a values, in this study, calculated from recovery data, were in excellent agreement with the laboratory-measured λ_r values. Hakala et al. (2022) also emphasised that recovery data yield more reliable estimates of λ_r. Thus, incorporating recovery data is essential for accurately identifying water-saturated zones and estimating subsurface thermal properties.

An additional observation is highlighted in Fig. 41c and d. While the T-cable recorded high temperatures forming a concave profile during heating, the recovery phase exhibited rapid heat dissipation, resulting in a slight convex temperature decrease. This suggests that interpreting groundwater presence based solely on heating data may lead to erroneous conclusions. For example, in the depth interval between 12.9 and 13.8 m, a low rate of temperature increase was observed in the heating curves. However, this did not correspond to a water-influenced zone, as clarified by the recovery data. This further supports the argument that heating data alone is insufficient for delineating groundwater flow zones.

6.4.5 Impact of lithological heterogeneity on heat transfer

The employed AH-DFOS sensing method provided detailed insights into small-scale heterogeneities. Closely looking at Fig. 33, the stratified thermal response closely matches the lithological layers. The thermal response observed during AH experiments is governed not only by groundwater flow but also by intrinsic rock properties such as λ, ϕ, permeability, and degree of fracturing (Violante et al., 2024; Zhang et al., 2020; Zhang et al., 2023). As reported in section 6.3.1, the sandstone and shale horizons below 30 m depth are relatively fresh and compact with high *UCS*, *BTS*, V_p, and low ϕ. This deep horizon corresponds to higher ΔT during AH-DFOS experiments with maximum ΔT reaching up to ~27 °C (Fig. 33). The ΔT were recorded comparatively low within shallow horizons, which corresponds

to highly fractured shale, tuffaceous layers, and gravel like materials, although the physical amd mechanical properties of rocks above 30 m depth were not investigated. This clearly shows that variations in properties across different lithologies result in depth-dependent differences in temperature profiles. The heating curves reveal pronounced temperature fluctuations in the shallow subsurface, where loose soil-like materials are highly susceptible to environmental temperature variations. Tuffaceous layers show less consistent heating, possibly due to higher ϕ. In contrast, deeper sections (below 45 m) exhibit more stable and higher ΔT, corresponding to compacted and less fractured black shale formations. This pronounced thermal response in shale is attributed to its relatively high λ_r. Laboratory measurements indicated that shale specimens had higher λ_r values, ranging from 2.73 to 2.86 W/mK, compared to muddy sandstone specimens (between 32 m to 35 m and 38 to 40 m), which ranged from 2.58 to 2.68 W/mK. The higher λ_r enabled more efficient heat conduction and storage within the shale due to its compact and fine-grained nature, leading to greater observable ΔT during the heating phase of the AH-OFDR experiment. After AH stops, the recovery rate also shows that the shale zones cool more slowly, retaining heat longer. Similar results of non-homogeneous rate of heat dissipation with depth were reported by McDaniel et al. (2018).

A particular observation occurs at 40.2 m, where heating curves indicate a lithological boundary between coarse sandstone and shale, characterised by a loose tuffaceous layer. Such abrupt gradient shifts highlight significant changes in λ at formation contacts. Similarly, the interval between 35–37 m shows a loose soil and gravel layer sandwiched between compact sandstone, evident from distinct heating and recovery responses. The faster cooling in this zone suggests the influence of active groundwater flow, highlighting the combined effect of lithological contrast and fluid movement on heat transfer. Overall, the qualitative visualisation of AH results reinforces the role of lithological heterogeneities

in governing subsurface thermal behaviour, essential for interpreting distributed temperature data in geotechnical and hydrogeological investigations.

6.5 Key findings of field demonstration

In conclusion, the application of the AH-DFOS based on the Rayleigh scattering technique in a deep downhole environment has effectively demonstrated its strong potential for high-resolution groundwater flow characterisation in fractured aquifers. The method demonstrated the ability to identify saturated zones in relatively short monitoring time, significantly reducing operational time compared to previous methods that required up to tens of hours. The use of PNC-OFDR provided a high spatial resolution of 5 cm, enabling precise detection of closely spaced transmissive fractures, an advantage over traditional DTS systems with meter-scale resolution. The rapid data acquisition time of 2.5 milliseconds and the ability to resolve fine-scale thermal anomalies make AH-DFOS well suited for real-time monitoring of complex subsurface flow systems. Under natural gradient conditions, the technique identified several zones of elevated saturation and groundwater movement, providing valuable insights into preferential flow pathways.

The study also established the effectiveness of using a q=9.4 W/m for detecting high-saturation and water flow zones, showing clearer thermal responses compared to lower power levels. However, in shallow, unconsolidated sediments, fluctuating environmental temperatures introduced irregular temperature signals. The inclusion of recovery (cooling) data alongside heating data proved essential for distinguishing high-dissipation (i.e., flow-active) zones, especially in low-permeability rocks. The λ_a values were in good agreement with λ_r and showed depth-dependent variation, with higher values in compacted shale and sandstone units. The long-term monitoring of grouted borehole provided valuable information about the hydraulic changes due to seasonal variations and localised rainfall.

Given the sensitivity of heat dissipation to volumetric groundwater flow rates through fractures in low-permeability formations, future work should aim to quantitatively evaluate this relationship. Additionally, challenges related to the positioning of heating and sensing cables suggest that future designs may benefit from parallel cable installation to improve heat distribution and data reliability. Overall, the field study underscores the broad applicability of the AH-DFOS sensing method across various sectors, including geothermal energy, carbon sequestration, hydraulic fracturing, and environmental remediation, where understanding subsurface flow and contaminant transport is critical. With continued advancements in grouted borehole AH applications, this approach is poised to become a powerful tool for site characterisation and long-term hydrogeological monitoring.

CHAPTER VII CHALLENGES AND FUTURE PROSPECTS

7.1 Challenges

While the literature analysis has revealed extensive research on DFOS methodologies for temperature/strain monitoring, this technology is still in the developmental stages. Despite the numerous advantages offered by applying these techniques, considerable technical constraints hinder their practical use in geotechnical monitoring. Only a few universities and industries have started testing this sensing technique in small-scale laboratory setups and field applications, indicating the need for wider commercialisation. Our literature survey, feasibility studies, and field investigations have identified specific limitations associated with these sensing techniques, particularly concerning cables, devices, cost, and data processing.

Optical fibres are typically made of glass (SiO_2 fibre as a sensor medium), whose ultimate strain is only about 5%, making them fragile and susceptible to breakage under mechanical stress (Wu et al., 2020). Various studies have explored the fragility of bare sensors compared to traditional transducers, indicating a potentially high failure rate in challenging environmental conditions without proper sensor packaging and protection methods. For structural health monitoring, bare FO sensors are often directly affixed to structures and covered with epoxy resin. However, extra caution is necessary during installation due to the vulnerability of bare fibres to excessive external loading and bending. Consequently, in most instances, it is imperative to encapsulate the bare fibre adequately to ensure survival in harsh field installation and operational environments (Gong et al., 2019).

The precise positioning of the H- and T-cable inside a borehole is challenging to control, yet it is a critical factor in accurately estimating thermal properties (Acharya et al., 2024). The cable placement can be visualised in two key ways: (a) the distance between the H-

and T-cables, and (b) the distance of each cable from the borehole wall. In the first case, a shorter distance between the H- and T-cables allows the T-cable to detect heat more quickly during a short heating period. Conversely, a greater separation between the cables may require a longer heating duration for the heat to be detected. However, as the AH time increases, the effect of cable spacing gradually diminishes (Zhang et al., 2023). In the second case, as the distance between a cable and the centre of the borehole increases, the cable moves closer to the borehole wall. In such scenarios, the surrounding ground absorbs more heat from the H-cable. When both the H- and T-cables are positioned near the borehole wall, groundwater movement effects can be detected more rapidly. Our feasibility study-I highlighted the influence of cable spacing on temperature rise trends (Acharya et al., 2024). Although cable guides were used to align the H- and T-cables within a 2-meter-long cement mortar, the heating results revealed that the cables were not perfectly parallel, leading to localised high-temperature readings where the cables were in close proximity. This finding underscores that even minor deviations from the assumed cable positions can introduce significant errors in thermal property analysis (Acharya et al., 2024; Moscoso Lembcke et al., 2016).

When considering integrating FO sensors in reinforcement materials, an important task is ensuring the precise transmission of mechanical quantities, specifically strain, from the rock/soil to the reinforcements and, ultimately, the fibre core. In the field installation of FO cables for monitoring unstable slopes, the entire strain transfer mechanism can be divided into two components: (i) from rock/soil to cable and (ii) within the multiple layers of the FO cable (Zhang et al., 2020). In certain instances, cables may necessitate additional protective measures to endure challenging geological conditions and adhere to reinforcements through the use of adhesives. However, these protective layers and adhesive materials typically result in a loss of strain transfer as they absorb a portion of the strain

(Alj et al., 2020). Additionally, in the context of subsurface thermal characterisation, the quantitative heat transfer analysis from H-cable to the T-cable and the influence of coatings, grout, and heterogeneous formations on heat transfer are challenging. Therefore, a comprehensive investigation into the strain/temperature transfer mechanism from rock/soil to the FO core becomes imperative in hydro-mechanical monitoring of slopes.

Being a novel sensing technology, the FOS technique is more expensive than traditional electrical monitoring equipment. Although FBGs are widely employed for measuring temperature and mechanical strain, the predominant drawback lies in the elevated costs of the associated interrogation systems, limiting their widespread commercial utilisation. Furthermore, DFOS sensors and their interrogators incur relatively higher costs than conventional systems. For example, systems such as Luna ODiSI-B, operating on DFOS principles, may range from €80,000 to €100,000, representing a substantial difference compared to vibrating wire and FBG technologies (Ivanov et al., 2021). Beyond the costs associated with cables and interrogators, additional expenses related to the installation and maintenance of equipment required for data collection and analysis contribute to the overall financial investment. In certain situations, the financial outlay for field applications may surpass the benefits derived from real-time monitoring, especially in projects with limited budgets or smaller-scale applications (Abedi et al., 2023). Despite the potential for prolonged reuse of analysers, the primary hindrance to the widespread adoption of optoelectronic components in monitoring geo-structures, such as slope reinforcements, remains the cost factor (Xu et al., 2018). However, with the rapid advances in FOS technologies, the cost associated with an FO monitoring system is expected to decrease dramatically in the years ahead.

DFOS methods occasionally yield extensive data with significant fluctuations and noise, which cannot be overlooked during analysis. Sun et al. (2020) mentioned that despite the high accuracy and good repeatability of DFOS technology, the measured data in tests often do not exhibit smooth curves due to factors such as the testing environment, soil deformation disparities, and irregularities in sensor installation. On occasions, there are considerable fluctuations in the original data, making it challenging to discern the specific trend of strain changes. In such instances, appropriate data processing methods are necessary to denoise and smooth the original data (Gao et al., 2021b, 2022). Despite the OFDR method having a significantly higher number of sampling points than other DFOS methods, the noise in the data measured with OFDR tends to be more pronounced (Gao et al., 2022). Our feasibility studies and field investigation employing the PNC-OFDR sensing method also yielded significant data fluctuation. Larger uncertainties occurred in the high-saturation zones due to the smaller temperature differences and data fluctuations, also reported by Munn et al. (2020). We utilised the adjacent-averaging method to smooth the data and remove the outliers. Sun et al. (2020) employed polynomial curve fitting based on the least squares method to process measured strain data. Gao et al. (2021a) utilised the wavelet analysis toolbox of MATLAB software (moving average method) to mitigate noise generated during BOTDR monitoring. Gao et al. (2022) utilized a combination of db wavelet function and adjacent-average method to denoise and smooth data collected from monitoring pile foundation deformation. Therefore, our experience and the literature analysis underscore the challenge of establishing effective data management protocols for FOS data processing can be a challenge.

7.2 Future directions

DFOS methods are well-known for generating large datasets due to their large sensing ranges and comparatively small spatial resolution. There is a need to develop efficient data compression algorithms to process raw sensor data streams and compress them to retain important information. Robust AI-enabled FOS technologies have emerged as a valuable tool for improving the performance of future FOS systems in handling extensive data gathered from vast distances (Venketeswaran et al., 2022). By integrating FO-generated data with AI-driven analysis, it is possible to achieve highly precise and comprehensive spatial coverage in predicting slope deformation, as exemplified by the research conducted by Wei et al. (2022).

Artificial neural networks (ANN) deliver lower data errors and speed up the signal processing 270 times faster than the conventional approach (Karapanagiotis et al., 2023). This approach also significantly reduces the data extraction time in the case of Rayleigh-based DFOS. Furthermore, convolutional neural networks (CNNs) denoise the dynamic DFOS signal, extend the measurement length, and allow up to 100 km of distributed sensing. In the case of Brillouin-based DFOS, the CNNs contributed significantly towards faster measurement times, achieving a nine-fold time reduction compared to the classic system (Karapanagiotis et al., 2023). We anticipate the development of more innovative AI-assisted sensing methods for the precise and convenient analysis of extensive data collected over long distances in the near future.

Utilising hybrid sensors that exploit at least two scattering mechanisms for multiparameter sensing can offer more valuable information and facilitate the comprehensive identification of geological hazards. FBG sensors are known for quasi-distributed, highly accurate, and dynamic measurements, while DFOS methods excel in

long-distance and large-scale measurements compared to FBG sensors. Combining these two sensing methods holds great significance for slope deformation monitoring and advancing the advanced EW system. Two options exist for hybrid sensing: (i) utilising two separate fibres and interrogators and (ii) combining two fibres in a single fibre (Li et al., 2019). The first option invariably complicates the monitoring system and adds to the cost. Few studies have established an integrated monitoring system based on discrete and distributed sensing methods. An innovative hybrid sensor system for the multiparameter monitoring scheme for slope safety is introduced by Li et al. (2019), which combines a stimulated Brillouin scattering-based distributed sensor with XFG [FBG and long-period fibre grating (LPFG)] sensors on a single fibre for the measurement of strains/temperatures. Gao et al. (2022) investigated the deformation of pile foundations using a combination of OFDR and BOTDR methods employing two different data demodulators for the two sensing methods. This joint FOS technology proves useful in situations where the length of the object to be measured exceeds the sensing range of OFDR and high sensing precision is required. Hybrid silica/POFs are relatively new and emerging sensors because of their extraordinary mechanical properties. These sensors possess a distinctive capability to measure substantial strain distributed across the fibre. Yi and Changyuan (2019) proposed a hybrid silica/polymer optical fibre sensor capable of enduring extraordinarily large strains. Experimental results demonstrated that the structure could withstand an ultimate tensile strain of 35%, 35 times larger than traditional fibres. Hence, future research should focus on advancing and deploying hybrid sensor systems to enable comprehensive monitoring of slope conditions.

More significantly, there is a notable absence of definitive guidance regarding the encapsulation of FO sensors, their integration into reinforcements and boreholes, and the provision of technical instructions. While global standards for utilising optical components

in data communication and telecommunications have been available for over three decades, there is no established global standard for the practical application of strain and temperature monitoring. Several companies offering FOS solutions provide proprietary guidelines; however, there is a distinct lack of standards or appropriate specifications from manufacturers of sensor components (Habel, 2018). A few standards have already been published, such as IEC 61757:2018 Fibre optic Sensors – Generic Specification, IEC 61757-1-1 Strain measurement – Strain sensors based on fibre Bragg gratings, ASTM Standard F3092-14 and Standard Terminology Relating to Optical Fibre Sensing Systems. However, standards specifically addressing the reliable application of sensors and interrogators in harsh environmental conditions are still lacking (Habel, 2018). Consequently, developing guidelines and specifications for system deployment and administration and technical instructions for the installation team should be a focus of future work, as also emphasised by Acharya and Kogure (2022).

Previous studies have mainly focused on monitoring slope reinforcement materials' mechanical performance, specifically strain monitoring, through various FOS methods. However, a detailed investigation is lacking regarding developing an FO-based landslide early-warning system (FO-LEWS) to take essential actions to prevent significant engineering disasters. The strain information provides valuable insights for identifying early warning signs at various stages of slope stability. Limited studies have delved into establishing FO-LEWS (Arslan Kelam et al., 2022; Costrada et al., 2021; Hu et al., 2018).

CHAPTER VIII CONCLUSIONS

This study demonstrated the applicability of the PNC-OFDR-based AH-DFOS technique for detecting water-saturated zones in various experimental configurations. Two feasibility studies and a field study were conducted to progressively evaluate the method's performance under controlled laboratory and field conditions.

Feasibility study-I validated the ability of AH-DFOS to detect water presence in a 2 m-long cement grout specimen. Heating a metallic cable induced a temperature gradient, with water-supplied sections exhibiting a slower rise due to water's higher λ and specific heat capacity. Temperature evolution showed three distinct phases: rapid, fast, and gentle increase. Although higher q enhanced temperature contrast, a low q (2.4 W/m) was still effective in detecting stagnant water zones. The results emphasise the importance of optimising q, heating duration, cable positioning, and embedding procedure to ensure reliable detection.

Feasibility study-II explored the method's performance in identifying high-saturation zones along a grouted FGRB. The AH-DFOS approach achieved 2 cm spatial resolution and 2.5 ms data acquisition time, far exceeding conventional DTS systems. It successfully detected closely spaced saturation zones. Temperature readings were influenced by the relative position between H- and T-cables; however, when sufficient power was applied, discrepancies between sensing cables spaced at 7 mm and 13 mm remained minimal. The findings indicate that using a separate sensing cable rather than a composite one enhances spatial resolution and improves the detection of water-saturated zones. At the location of high-saturated zones, a *thermal halo* forms on either side of the zone. Detecting closely spaced high-saturation zones and their corresponding *thermal halos* requires fine spatial resolution, such as that provided by the PNC-OFDR method employed in this study. The

rate of ΔT decreases as the width of the high saturation zones increases, since a wider saturated zone allows a greater volume of water to interact with and dissipate the heat generated by the heat source by creating a temperature-stabilised zone.

Field study applied the method in a 50 m-deep borehole, revealing strong potential for in-situ groundwater flow characterisation in fractured aquifers. The system identified saturated zones within short monitoring durations, surpassing the efficiency of traditional methods. A spatial resolution of 5 cm enabled detection of closely spaced transmissive fractures, and the rapid acquisition time of 2.5 ms allowed real-time monitoring of thermal anomalies. The method effectively identified preferential flow pathways under natural gradient conditions. A q of 9.4 W/m provided clearer thermal signals, and recovery-phase data (cooling) were essential for distinguishing active flow zones, especially in low-permeability formations. The λ estimates from AH-DFOS closely matched laboratory values and varied with lithology, being higher in compacted shale and sandstone. In addition, the hydraulic changes due to the influence of localised rainfall and yearly seasonal variations were investigated.

This study showed that AH-DFOS is a powerful tool for detecting groundwater movement with high accuracy and can help geoscientists better understand complex underground water systems. Future research should focus on quantifying the relationship between heat dissipation and groundwater flux in low-permeability fractured systems. Improved cable installation techniques, such as parallel layouts demonstrated in feasibility study-II, may enhance heat transfer efficiency and data reliability. Ongoing seasonal monitoring will further elucidate temporal changes in subsurface hydrology. Broader application areas include slope stability assessment, geothermal energy, hydraulic fracturing, and environmental remediation, where accurate characterisation of subsurface flow and contaminant transport is crucial. With further advancements, AH-DFOS is poised

to become a robust tool for high-resolution, long-term hydrogeological monitoring and site characterisation.

REFERENCES

Abedi, M., Fangueiro, R., Correia, A.G., Shayanfar, J., 2023. Smart geosynthetics and prospects for civil infrastructure monitoring: a comprehensive and critical review. Sustainability 15, 9258. https://doi.org/10.3390/su15129258

Acharya, A., Kogure, T., 2024. Advances in fibre-optic-based slope reinforcement monitoring: a review. J. Rock Mech. Geotech. Eng. 17(2), 1263-1284 https://doi.org/10.1016/j.jrmge.2024.03.022

Acharya, A., Kogure, T., 2022. Application of novel distributed fibre-optic sensing for slope deformation monitoring: a comprehensive review. Int. J. Environ. Sci. Technol. 20, 8217–8240. https://doi.org/10.1007/s13762-022-04697-5

Acharya, A., Tanimura, D., Zhang, C., Ito, F., Sakaki, T., Komatsu, M., Doi, I., Kogure, T., 2024. Assessing water position through distributed temperature sensing using Rayleigh-based optical frequency-domain reflectometry: a laboratory feasibility study. Can. Geotech. J. 62, 1-14. https://doi.org/10.1139/cgj-2023-0345

Addanki, S., Amiri, I.S., Yupapin, P., 2018. Review of optical fibers-introduction and applications in fiber lasers. Results Phys. 10, 743–750. https://doi.org/10.1016/j.rinp.2018.07.028

Alj, I., Quiertant, M., Khadour, A., Grando, Q., Terrade, B., Renaud, J.C., Benzarti, K., 2020. Experimental and numerical investigation on the strain response of distributed optical fiber sensors bonded to concrete: influence of the adhesive stiffness on crack monitoring performance. Sensors 20, 5144. https://doi.org/10.3390/s20185144

Amer, R., Xue, Z., Hashimoto, T., Nagata, T., 2021 Distributed fibre optic strain sensing for geomechanical monitoring: insights from field measurements of ground surface deformation. Geosciences 11(7):285. https://doi.org/10.3390/geosciences11070285

Arslan Kelam, A., Akgün, H., Koçkar, M.K., 2022. Application of an optical fiber-based system for mass movement monitoring. Environ. Earth Sci. 81, 170. https://doi.org/10.1007/s12665-022-10289-w

ASTM, 2023a. Standard test method for pulse velocity through concrete. URL https://www.astm.org/c0597-16.html (accessed 5.5.25).

ASTM, 2023b. Standard test method for splitting tensile strength of intact rock core specimens. URL https://www.astm.org/d3967-16.html (accessed 5.5.25).

ASTM, 2022. Standard test method for determination of thermal conductivity of soil and rock by thermal needle probe procedure. URL https://www.astm.org/d5334-22.html (accessed 5.5.25).

ASTM, 2017. Standard test method for unconfined compressive strength of intact rock core specimens. URL https://www.astm.org/d2938-95.html (accessed 5.5.25).

Bado, M.F., Casas, J.R., 2021 A review of recent distributed optical fibre sensors applications for civil engineering structural health monitoring. Sensors 21(5):1818. https://doi.org/10.3390/s21051818

Bakker, M., Caljé, R., Schaars, F., van der Made, K.J., de Haas, S., 2015. An active heat tracer experiment to determine groundwater velocities using fiber optic cables installed with direct push equipment. Water Resour. Res. 51, 2760–2772. https://doi.org/10.1002/2014WR016632

Bakx, W., Doornenbal, P.J., van Weesep, R.J., Bense, V.F., Oude Essink, G.H.P., Bierkens, M.F.P., 2019. Determining the relation between groundwater flow

velocities and measured temperature differences using active heating-distributed temperature sensing. Water 11, 1619. https://doi.org/10.3390/w11081619

Banks, E.W., Morgan, L.K., Sai Louie, A.J., Dempsey, D., Wilson, S.R., 2022. Active distributed temperature sensing to assess surface water–groundwater interaction and river loss in braided river systems. J. Hydrol. 615, 128667. https://doi.org/10.1016/j.jhydrol.2022.128667

Bao, X., Wang, Y., 2021. Recent aadvancements in Rayleigh scattering-based distributed fiber sensors. Adv. Devices X0026 Instrum. 2021. https://doi.org/10.34133/2021/8696571

Barrias, A., Casas, J., Villalba, S., 2016. A review of distributed optical fiber sensors for civil engineering applications. Sensors 16, 748. https://doi.org/10.3390/s16050748

Benítez-Buelga, J., Rodríguez-Sinobas, L., Sánchez Calvo, R., Gil-Rodríguez, M., Sayde, C., Selker, J.S., 2016. Calibration of soil moisture sensing with subsurface heated fiber optics using numerical simulation. Water Resour. Res. 52, 2985–2995. https://doi.org/10.1002/2015WR017897

Bense, V.F., Read, T., Bour, O., Le Borgne, T., Coleman, T., Krause, S., Chalari, A., Mondanos, M., Ciocca, F., Selker, J.S., 2016. Distributed temperature sensing as a downhole tool in hydrogeology. Water Resour. Res. 52, 9259–9273. https://doi.org/10.1002/2016WR018869

Briggs, M.A., Buckley, S.F., Bagtzoglou, A.C., Werkema, D.D., Lane Jr, J.W., 2016. Actively heated high-resolution fiber-optic-distributed temperature sensing to quantify streambed flow dynamics in zones of strong groundwater upwelling. Water Resour. Res. 52, 5179–5194. https://doi.org/10.1002/2015WR018219

Campanella, C.E., Ai, G., Ukil, A., 2016 Distributed fibre optics techniques for gas network monitoring. 2016 IEEE International Conference on Industrial Technology (ICIT), 646–651. https://doi.org/10.1109/ICIT.2016.7474825

Cao, D., Shi, B., Zhu, H., Inyang, H.I., Wei, G., Duan, C., 2018. A soil moisture estimation method using actively heated fiber Bragg grating sensors. Eng. Geol. 242, 142–149. https://doi.org/10.1016/j.enggeo.2018.05.024

Chen, C., Gao, S., Chen, L., Bao, X., 2020. Distributed high temperature monitoring of SMF under electrical arc discharges based on OFDR. Sensors 20, 6407. https://doi.org/10.3390/s20226407

Cheng, L., Zhang, A., Cao, B., Yang, J., Hu, L., Li, Y., 2021. An experimental study on monitoring the phreatic line of an embankment dam based on temperature detection by OFDR. Opt. Fiber Technol. 63, 102510. https://doi.org/10.1016/j.yofte.2021.102510

Coleman, T.I., Parker, B.L., Maldaner, C.H., Mondanos, M.J., 2015. Groundwater flow characterization in a fractured bedrock aquifer using active DTS tests in sealed boreholes. J. Hydrol. 528, 449–462. https://doi.org/10.1016/j.jhydrol.2015.06.061

Costrada, A.N., Harmadi, Kemal, B.M., Marzuki, 2021. Landslide monitoring system based on fiber optic sensor and CCD TSL1401CL linear sensor array. J. Phys. Conf. Ser. 1876, 012002. https://doi.org/10.1088/1742-6596/1876/1/012002

Das, R., Singh, T.N., 2021. Effect of rock bolt support mechanism on tunnel deformation in jointed rockmass: A numerical approach. Undergr. Space 6, 409–420. https://doi.org/10.1016/j.undsp.2020.06.001

Del Val, L., Carrera, J., Pool, M., Martínez, L., Casanovas, C., Bour, O., Folch, A., 2021. Heat dissipation test with fiber-optic distributed temperature sensing to estimate

groundwater flux. Water Resour. Res. 57, e2020WR027228. https://doi.org/10.1029/2020WR027228

Ding, Z., Wang, C., Liu, K., Jiang, J., Yang, D., Pan, G., Pu, Z., Liu, T., 2018. Distributed optical fiber sensors based on optical frequency domain reflectometry: a review. Sensors 18, 1072. https://doi.org/10.3390/s18041072

Fan, X., Koshikiya, Y., Ito, F., 2007. Phase-noise-compensated optical frequency domain reflectometry with measurement range beyond laser coherence length realized using concatenative reference method. Opt. Lett. 32, 3227. https://doi.org/10.1364/OL.32.003227

Farahani, M.A., Gogolla, T., 1999. Spontaneous Raman scattering in optical fibers with modulated probe light for distributed temperature Raman remote sensing. J. Light. Technol. 17, 1379–1391. https://doi.org/10.1109/50.779159

Forbes, B., Vlachopoulos, N., Hyett, A.J., 2018. The application of distributed optical strain sensing to measure the strain distribution of ground support members. FACETS 3, 195–226. https://doi.org/10.1139/facets-2017-0093

Freifeld, B.M., Finsterle, S., Onstott, T.C., Toole, P., Pratt, L.M., 2008. Ground surface temperature reconstructions: using in situ estimates for thermal conductivity acquired with a fiber-optic distributed thermal perturbation sensor. Geophys. Res. Lett. 35. https://doi.org/10.1029/2008GL034762

Gao, L., Cao, Y., Liu, H.L., Zhao, Z.X., Ye, Y.F., Fan, C.J., Zhang, L.Z., Tu, W.J., 2021a. Experiment and numerical study on the monitoring of super long cast-in-place pile temperature based on BOTDR technology. Measurement 179, 109481. https://doi.org/10.1016/j.measurement.2021.109481

Gao, L., Han, C., Abdulhafidh, O., Gong, Y., Jin, Y., 2021b. An Application of BOTDR to the Measurement of the Curing of a Bored Pile. Appl. Sci. 11, 418. https://doi.org/10.3390/app11010418

Gao, L., Qian, J., Han, C., Qin, S., Feng, K., 2022. Experimental study of deformation measurement of bored pile using OFDR and BOTDR joint optical fiber sensing technology. Sustainability 14, 16557. https://doi.org/10.3390/su142416557

Ghafoori, Y., Maček, M., Vidmar, A., Říha, J., Kryžanowski, A., 2020. Analysis of seepage in a laboratory scaled model using passive optical fiber distributed temperature sensor. Water 12, 367. https://doi.org/10.3390/w12020367

Gómez, J., Casas, J.R., Villalba, S., 2020. Structural health monitoring with distributed optical fibre sensors of tunnel lining affected by nearby construction activity. Automation in Construction 117:103261. https://doi.org/10.1016/j.autcon.2020.103261

Gong, H., Kizil, M.S., Chen, Z., Amanzadeh, M., Yang, B., Aminossadati, S.M., 2019. Advances in fibre optic based geotechnical monitoring systems for underground excavations. Int. J. Min. Sci. Technol. 29, 229–238. https://doi.org/10.1016/j.ijmst.2018.06.007

Guo, X., Wang, B., Wang, Z., Yu, W., Ma, Z., Yang, T., 2020. Application of the microclamped fiber Bragg Grating (FBG) sensor in rock bolt support quality monitoring. Adv. Civ. Eng. 2020, e3419835. https://doi.org/10.1155/2020/3419835

Habel, W.R., 2018. Optical fiber methods in nondestructive evaluation, in: Ida, N., Meyendorf, N. (Eds.), Handbook of Advanced Non-Destructive Evaluation. Springer International Publishing, Cham, pp. 1–49. https://doi.org/10.1007/978-3-319-30050-4_39-1

Hakala, P., Vallin, S., Arola, T., Martinkauppi, I., 2022. Novel use of the enhanced thermal response test in crystalline bedrock. Renew. Energy 182, 467–482. https://doi.org/10.1016/j.renene.2021.10.020

Hill, K.O., Fujii, Y., Johnson, D.C., Kawasaki, B.S., 1978. Photosensitivity in optical fiber waveguides: Application to reflection filter fabrication. Appl. Phys. Lett. 32, 647–649. https://doi.org/10.1063/1.89881

Hill, K.O., Meltz, G., 1997. Fiber Bragg grating technology fundamentals and overview. J. Light. Technol. 15, 1263–1276. https://doi.org/10.1109/50.618320

Hoehn, K., Spearing, A.J.S. (Sam), Jessu, K.V., Singh, P., Pinazzi, P.C., 2020. The design of improved optical fibre instrumented rockbolts. Geotech. Geol. Eng. 38, 4349–4359. https://doi.org/10.1007/s10706-020-01246-0

Hu, T., Hou, G., Li, Z., 2020. The field monitoring experiment of the roof strata movement in coal mining based on DFOS. Sensors 20, 1318. https://doi.org/10.3390/s20051318

Hu, Y., Hong, C., Zhang, Y., Li, G., 2018. A monitoring and warning system for expressway slopes using FBG sensing technology. Int. J. Distrib. Sens. Netw. 14, 155014771877622. https://doi.org/10.1177/1550147718776228

ISRM, 2018. Suggested method on Brazilian tension test (2018) [WWW Document]. URL https://isrm.net/page/show/1339 (accessed 3.4.24).

Ivanov, V., Longoni, L., Ferrario, M., Brunero, M., Arosio, D., Papini, M., 2021. Applicability of an interferometric optical fibre sensor for shallow landslide monitoring – Experimental tests. Eng. Geol. 288, 106128. https://doi.org/10.1016/j.enggeo.2021.106128

JSA, 2020. JIS A 1202 : Test method for density of soil particles [WWW Document]. URL

https://global.ihs.com/doc_detail.cfm?&input_search_filter=JSA&item_s_key=00227098&item_key_date=790906&input_doc_number=JIS%20A%201202&input_doc_title=&org_code=JSA (accessed 3.4.24).

Kang, W., 2023. Understanding Seepage in levees and exploring the applicability of using an optical-fiber distributed temperature system and smoothing technique as a monitoring method. Sensors 23, 4780. https://doi.org/10.3390/s23104780

Kano, K., Takeuchi, K., Yamamoto, T., Hoshizumi, H., 1991. Subaqueous rhyolite block lavas in the Miocene Ushikiri Formation, Shimane Peninsula, SW Japan. J. Volcanol. Geotherm. Res. 46, 241–253. https://doi.org/10.1016/0377-0273(91)90086-F

Karapanagiotis, C., Hicke, K., Krebber, K., 2023. A collection of machine learning assisted distributed fiber optic sensors for infrastructure monitoring. Tm - Tech. Mess. 90, 177–195. https://doi.org/10.1515/teme-2022-0098

Kim, D., Oh, S., 2019. Relationship between the thermal properties and degree of saturation of cementitious grouts used in vertical borehole heat exchangers. Energy Build. 201, 1–9. https://doi.org/10.1016/j.enbuild.2019.07.017

Kishida, K., Yamauchi, Y., Guzik, A., 2014. Study of optical fibers strain-temperature sensitivities using hybrid Brillouin-Rayleigh system. Photonic Sens. 4, 1–11. https://doi.org/10.1007/s13320-013-0136-1

Klepikova, M., Brixel, B., Roubinet, D., 2022. Analysis of thermal dilution experiments with distributed temperature sensing for fractured rock characterization. J. Hydrol. 610, 127874. https://doi.org/10.1016/j.jhydrol.2022.127874

Kogure, T., Okuda, Y., 2018. Monitoring the vertical distribution of rainfall-induced strain changes in a landslide measured by distributed fiber optic sensing with

Rayleigh Backscattering. Geophys. Res. Lett. 45, 4033–4040. https://doi.org/10.1029/2018GL077607

Leung, C.K.Y., Wan, K.T., Inaudi, D., Bao, X., Habel, W., Zhou, Z., Ou, J., Ghandehari, M., Wu, H.C., Imai, M., 2015. Review: optical fiber sensors for civil engineering applications. Mater. Struct. 48, 871–906. https://doi.org/10.1617/s11527-013-0201-7

Li, F., Qin, W., Hu, H., 2022. Experimental investigation monitoring the saturated line of slope based on distributed optical fiber temperature system. Adv. Mater. Sci. Eng. 2022, e9243361. https://doi.org/10.1155/2022/9243361

Li, F., Zhao, W., Xu, H., Wang, S., Du, Y., 2019. A highly integrated BOTDA/XFG sensor on a single fiber for simultaneous multi-parameter monitoring of slopes. Sensors 19, 2132. https://doi.org/10.3390/s19092132

Li, H., Yang, M., 2024. Application study of distributed optical fiber seepage monitoring technology on embankment engineering. Appl. Sci. 14, 5362. https://doi.org/10.3390/app14135362

Li, J., Zhang, M., 2022. Physics and applications of Raman distributed optical fiber sensing. Light Sci. Appl. 11, 128. https://doi.org/10.1038/s41377-022-00811-x

Liu, G., Knobbe, S., Butler Jr., J. j., 2013. Resolving centimeter-scale flows in aquifers and their hydrostratigraphic controls. Geophys. Res. Lett. 40, 1098–1103. https://doi.org/10.1002/grl.50282

Liu, J., Cui, Y.J., Sun, M.Y., Gu, K., Yao, J.C., Tang, C.S., Shi, B., 2024. Field investigation of unsaturated hydraulic conductivity using actively heated fiber-optic technology. J. Hydrol. 639, 131596. https://doi.org/10.1016/j.jhydrol.2024.131596

Liu, T., Sun, W., Kou, H., Yang, Z., Meng, Q., Zheng, Y., Wang, H., Yang, X., 2019. Experimental study of leakage monitoring of diaphragm walls based on distributed optical fiber temperature measurement technology. Sensors 19, 2269. https://doi.org/10.3390/s19102269

Lu, P., Lalam, N., Badar, M., Liu, B., Chorpening, B.T., Buric, M.P., Ohodnicki, P.R., 2019. Distributed optical fiber sensing: review and perspective. Appl. Phys. Rev. 6, 041302. https://doi.org/10.1063/1.5113955

Maldaner, C.H., Munn, J.D., Coleman, T.I., Molson, J.W., Parker, B.L., 2019. Groundwater flow quantification in fractured rock boreholes using active distributed temperature sensing under natural gradient conditions. Water Resour. Res. 55, 3285–3306. https://doi.org/10.1029/2018WR024319

McDaniel, A., Tinjum, J., Hart, D.J., Lin, Y.F., Stumpf, A., Thomas, L., 2018. Distributed thermal response test to analyze thermal properties in heterogeneous lithology. Geothermics 76, 116–124. https://doi.org/10.1016/j.geothermics.2018.07.003

Mikolajek, M., Martinek, R., Koziorek, J., Hejduk, S., Vitasek, J., Vanderka, A., Poboril, R., Vasinek, V., Hercik, R., 2020. Temperature measurement using optical fiber methods: overview and evaluation. J. Sens. 2020, 1–25. https://doi.org/10.1155/2020/8831332

Minardo, A., Catalano, E., Coscetta, A., Zeni, G., Zhang, L., Di Maio, C., Vassallo, R., Coviello, R., Macchia, G., Picarelli, L., Zeni, L., 2018. Distributed fiber optic sensors for the monitoring of a tunnel crossing a landslide. Remote Sens. 10, 1291. https://doi.org/10.3390/rs10081291

Munn, J.D., Maldaner, C.H., Coleman, T.I., Parker, B.L., 2020. Measuring fracture flow changes in a bedrock aquifer due to open hole and pumped conditions using active

distributed temperature sensing. Water Resour. Res. 56, e2020WR027229. https://doi.org/10.1029/2020WR027229

Moscoso Lembcke, L. G., Roubinet, D., Gidel, F., Irving, J., Pehme, P., and Parker, B. L. (2016). Analytical analysis of borehole experiments for the estimation of subsurface thermal properties. Advances in Water Resources, 91, 88–103. https://doi.org/10.1016/j.advwatres.2016.02.011

Nakazawa, M., 1983. Rayleigh backscattering theory for single-mode optical fibers. J. Opt. Soc. Am. 73, 1175. https://doi.org/10.1364/JOSA.73.001175

Nomura, R., 2021. Geologic age of the lower Josoji Formation, Shimane Peninsula, Southwest Honshu, Japan: Implications for an abrupt change to deep-water during the earlier opening stage of the Japan Sea. Isl. Arc 30, e12421. https://doi.org/10.1111/iar.12421

Nyarko-Boateng, O., Xedagbui, F.E.B., Adekoya, A.F., Weyori, B.A., 2020. Fiber optic deployment challenges and their management in a developing country: a tutorial and case study in Ghana. Eng. Rep. 2, e12121. https://doi.org/10.1002/eng2.12121

Pehme, P.E., Greenhouse, J.P., Parker, B.L., 2007. The active line source temperature logging technique and its application in fractured rock hydrogeology. J. Environ. Eng. Geophys. 12, 307–322. https://doi.org/10.2113/JEEG12.4.307

Puzrin AM, Iten M, Fischli F (2020) Monitoring of ground displacements using borehole-embedded distributed fibre optic sensors. Q. J. Eng. Geol. Hydrogeol. 53(1):31–38. https://doi.org/10.1144/qjegh2018-166

Read, T., Bour, O., Selker, J.S., Bense, V.F., Borgne, T.L., Hochreutener, R., Lavenant, N., 2014. Active-distributed temperature sensing to continuously quantify vertical flow in boreholes. Water Resour. Res. 50, 3706–3713. https://doi.org/10.1002/2014WR015273

Ren, L., Jiang, T., Jia, Z., Li, D., Yuan, C., Li, H., 2018. Pipeline corrosion and leakage monitoring based on the distributed optical fiber sensing technology. Measurement 122, 57–65. https://doi.org/10.1016/j.measurement.2018.03.018

Sakaki, T., Firat Lüthi, B., Vogt, T., Uyama, M., Niunoya, S., 2019. Heated fiber-optic cables for distributed dry density measurements of granulated bentonite mixtures: Feasibility experiments. Geomech. Energy Environ. 17, 57–65. https://doi.org/10.1016/j.gete.2018.09.006

Schenato, L., 2017. A review of distributed fibre optic sensors for geo-hydrological applications. Appl. Sci. 7, 896. https://doi.org/10.3390/app7090896

Schenato, L., Palmieri, L., Camporese, M., Bersan, S., Cola, S., Pasuto, A., Galtarossa, A., Salandin, P., Simonini, P., 2017. Distributed optical fibre sensing for early detection of shallow landslides triggering. Sci. Rep. 7, 14686. https://doi.org/10.1038/s41598-017-12610-1

Selker, F., Selker, J.S., 2018. Investigating water movement within and near wells using active point heating and fiber optic distributed temperature sensing. Sensors 18, 1023. https://doi.org/10.3390/s18041023

Shiratsuchi, T., Imai, T., 2021. Development of fiber Bragg grating strain sensor with temperature compensation for measurement of cryogenic structures. Cryogenics 113, 103233. https://doi.org/10.1016/j.cryogenics.2020.103233

Simon, N., Bour, O., Lavenant, N., Porel, G., Nauleau, B., Klepikova, M., 2023. Monitoring groundwater fluxes variations through active-DTS measurements. J. Hydrol. 622, 129755. https://doi.org/10.1016/j.jhydrol.2023.129755

Stolarska, A., Strzałkowski, J., 2020. The thermal parameters of mortars based on different cement type and w/c ratios. Materials 13, 4258. https://doi.org/10.3390/ma13194258

Su, H., Hu, J., Yang, M., 2015. Dam seepage monitoring based on distributed optical fiber temperature system. IEEE Sens. J. 15, 9–13. https://doi.org/10.1109/JSEN.2014.2335197

Su, H., Kang, Y., 2013. Design of system for monitoring seepage of levee engineering based on distributed optical fiber sensing technology. Int. J. Distrib. Sens. Netw. 9, 358784. https://doi.org/10.1155/2013/358784

Su, H., Tian, S., Kang, Y., Xie, W., Chen, J., 2017. Monitoring water seepage velocity in dikes using distributed optical fiber temperature sensors. Autom. Constr. 76, 71–84. https://doi.org/10.1016/j.autcon.2017.01.013

Sun, C., Tang, C.S., Vahedifard, F., Cheng, Q., Dong, A., Gao, T.F., Shi, B., 2024. High-resolution monitoring of soil infiltration using distributed fiber optic. J. Hydrol. 640, 131691. https://doi.org/10.1016/j.jhydrol.2024.131691

Sun, Y., Cao, S., Xu, H., Zhou, X., 2020. Application of distributed fiber optic sensing technique to monitor stability of a geogrid-reinforced model slope. Int. J. Geosynth. Ground Eng. 6, 29. https://doi.org/10.1007/s40891-020-00209-y

Tang, B., Cheng, H., 2018. Application of distributed optical fiber sensing technology in surrounding rock deformation control of TBM-excavated coal mine roadway. J. Sens. 2018, 1–10. https://doi.org/10.1155/2018/8010746

Tyler, S.W., Selker, J.S., Hausner, M.B., Hatch, C.E., Torgersen, T., Thodal, C.E., Schladow, S.G., 2009. Environmental temperature sensing using Raman spectra DTS fiber-optic methods. Water Resour. Res. 45. https://doi.org/10.1029/2008WR007052

Ukil, A., Braendle, H., Krippner, P., 2012. Distributed temperature sensing: review of technology and applications. IEEE Sens. J. 12, 885–892. https://doi.org/10.1109/JSEN.2011.2162060

Venketeswaran, A., Lalam, N., Wuenschell, J., Ohodnicki Jr., P.R., Badar, M., Chen, K.P., Lu, P., Duan, Y., Chorpening, B., Buric, M., 2022. Recent advances in machine learning for fiber optic sensor applications. Adv. Intell. Syst. 4, 2100067. https://doi.org/10.1002/aisy.202100067

Violante, A.C., Guidi, G., Proposito, M., Mataloni, S., Spaziani, F., 2024. Use of distributed temperature sensing (DTS) coupled to ground source heat exchangers for geological thermo-stratigraphic correlation. Renew. Energy 225, 120242. https://doi.org/10.1016/j.renene.2024.120242

Vlachopoulos, N., 2023. The use of fiber optics for ground and tunnel support monitoring – Two decades of lessons learned, in: Expanding Underground - Knowledge and Passion to Make a Positive Impact on the World. CRC Press.

Wei, C., Deng, Q., Yin, Y., Yan, M., Lu, M., Deng, K., 2022. A machine learning study on internal force characteristics of the anti-slide pile based on the DOFS-BOTDA monitoring technology. Sensors 22, 2085. https://doi.org/10.3390/s22062085

Wu, H., Yao, C., Li, C., Miao, M., Zhong, Y., Lu, Y., Liu, T., 2020. Review of application and innovation of geotextiles in geotechnical engineering. Materials 13, 1774. https://doi.org/10.3390/ma13071774

Xu, D., Yin, J., Liu, H., 2018. A new measurement approach for deflection monitoring of large-scale bored piles using distributed fiber sensing technology. Measurement 117, 444–454. https://doi.org/10.1016/j.measurement.2017.12.032

Xu, D.S., Liu, H.B., Luo, W.L., 2018. Evaluation of interface shear behavior of GFRP soil nails with a strain-transfer model and distributed fiber-optic sensors. Comput. Geotech. 95, 180–190. https://doi.org/10.1016/j.compgeo.2017.10.005

Yan, J.F., Shi, B., Zhu, H.H., Wang, B.J., Wei, G.Q., Cao, D.F., 2015. A quantitative monitoring technology for seepage in slopes using DTS. Eng. Geol. 186, 100–104. https://doi.org/10.1016/j.enggeo.2015.01.001

Yanes, J.L., Jiménez-Bonilla, A., Martínez-Caro, M., Fernández-Ayuso, A., Rodríguez-Rodríguez, M., 2025. Groundwater/surface water temperature variations and hydrogeological implications in Doñana National Park. Environments 12, 83. https://doi.org/10.3390/environments12030083

Ye, X.W., Su, Y.H., Han, J.P., 2014. Structural health monitoring of civil infrastructure using optical fiber sensing technology: a comprehensive review. Sci. World J. 2014, 1–11. https://doi.org/10.1155/2014/652329

Yi, L., Changyuan, Y., 2019. Highly stretchable hybrid silica/polymer optical fiber sensors for large-strain and high-temperature application. Opt. Express 27, 20107–20116. https://doi.org/10.1364/OE.27.020107

Zhan, Y., Li, N., Wang, H., Zheng, P., Zhang, J., Liu, Q., 2020. The mechanism of interface dilatancy of cement mortar rockbolts. Adv. Civ. Eng. 2020, 8838488. https://doi.org/10.1155/2020/8838488

Zhang, A., Li, Y., 2023. Thermal conductivity of aluminum alloys—a review. Materials 16, 2972. https://doi.org/10.3390/ma16082972

Zhang, B., Gu, K., Bayer, P., Qi, H., Shi, B., Wang, B., Jiang, Y., Zhou, Q., 2023. Estimation of groundwater flow rate by an actively heated fiber optics based thermal response test in a grouted borehole. Water Resour. Res. 59, e2022WR032672. https://doi.org/10.1029/2022WR032672

Zhang, B., Gu, K., Shi, B., Liu, C., Bayer, P., Wei, G., Gong, X., Yang, L., 2020. Actively heated fiber optics based thermal response test: A field demonstration.

Renew. Sustain. Energy Rev. 134, 110336. https://doi.org/10.1016/j.rser.2020.110336

Zhang, C.C., Shi, B., Zhang, S., Gu, K., Liu, S.P., Gong, X.L., Wei, G.Q., 2021 Microanchored borehole fibre optics allows strain profiling of the shallow subsurface. Sci. Rep. 11(1):9173. https://doi.org/10.1038/s41598-021-88526-8

Zhang, C., Shi, B., Zhu, H., Wang, B., Wei, G., 2020. Toward distributed fiber-optic sensing of subsurface deformation: a theoretical quantification of ground-borehole-cable interaction. J. Geophys. Res. Solid Earth 125. https://doi.org/10.1029/2019JB018878

Zhu, H.H., Ye, X., Pei, H.F., Zhang, W., Cheng, G., Li, Z.L., 2023. Probing multi-physical process and deformation mechanism of a large-scale landslide using integrated dual-source monitoring. Geosci. Front. 101773. https://doi.org/10.1016/j.gsf.2023.101773

Tables

Table 1 Relative performance characteristics of each type of distributed sensing (based on Barrias et al. 2016; Lu et al. 2019; Schenato 2017).

Distributed sensing technique	Sensing Range	Spatial resolution	Measurement time	*T* and *ε*	Fibre type
Coherent Rayleigh OFDR (COFDR)	10 m	1.3 mm	42 ms	Yes	SMF
	70 m	1 cm	10-20 s		
Coherent Rayleigh OTDR (COTDR)	Up to 40 km	4 m	20-500 μs	Yes	SMF
	100 km	5 m	n/a		
BOTDR	45 km	5 m	1800 s	Yes	SMF or few-mode
	20-50 km	1 m	n/a		
BOTDA	10 km	1.5 m	4 s	Yes	SMF or few-mode
	60 km	4 m	600 s		
Raman OTDR	1-37 km	1 cm-17 m	n/a	*T* only	SMF/MMF

Table 2 Technical specifications and functional comparison of the two types of cables used in this study.

Cable name	Buffered composite cable	Loose-tube picocable
	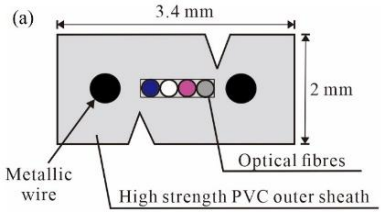	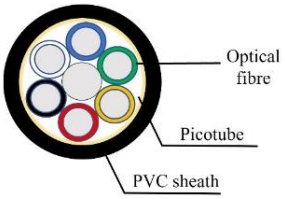
Purpose	Heating for feasibility-I, feasibility-II, and field demonstration study	Temperature sensing
	Tight buffered	Loose tube (surrounds fibre with hydrophobic gel)
Manufacturer	Fujikura 2014, Tokyo, Japan	Nippon Steel Trading Corporation, Tokyo, Japan
Dimension	Length: 3.4 mm; width: 2 mm	Coating outer diameter ⌀3.5 (PE coating)
Cladding diameter	ϕ 0.25	ϕ0.25 mm (same for both SMF and MMF)
Core diameter	ϕ 0.125	ϕ 0.125
Allowable strength (N)	230	147
Allowable bending radius (mm)	70	40
Wavelength (μm)	1310	1310
Transmission loss (dB/km)	0.165	≦0.35
Reason for selection	High insulation resistance, high dielectric strength, enhanced safety due to oxygen and temperature index properties; dual functionality for heating and sensing	Superior water resistance, airtightness, lateral pressure resistance, lightweight, high efficiency

Table 3 Different stages of electrical power used for heating.

	Voltage (V)	Current (A)	Heating cable length (m)	Cable resistivity per unit length (ohm/m)	Power per unit length, Q, (W/m)
Feasilibity study-I	8	1.22	6.3	1.04	1.6
	10	1.53	6.3	1.04	2.4
	12	1.83	6.3	1.04	3.5
	14	2.14	6.3	1.04	4.8
	16	2.44	6.3	1.04	6.2
	18	2.75	6.3	1.04	7.8
Feasilibity study-II	18	2.75	6.4	1.04	7.6
Field demonstration	200	2.04	110	1.04	3.7
	250	2.94	110	1.04	5.8
	320	3.22	110	1.04	9.4

Table 4 Composition of the cement grout used in this study.

Item	Name	Mixing ratio (%)	Density (g/cm^3)
Binding material	Ordinary Portland cement	37.1	3.16
Aggregate	Processed sand (crushed granitic sand of <3.0 mm)	59.7	2.60
Admixture	Calcium oxide (or quicklime) (expansive agent to improve compressive strength and reduce shrinkage)	3.2	3.12
w/c ratio		0.45	

Table 5 ΔT at different times detected at five different sections along the specimen.

Voltage (V)	Power per unit length, Q, (W/m)	Sections along the specimen	Elapsed time (min)					
			30	60	90	120	150	180
10	2.4	I	5.9-10.3	8.7-13.4	9.2-13.4	9.5-15.4	6.8-12.1	7.8-13.3
		II	4.1-8.8	5.1-10.7	4.8-10.7	5.8-11.4	2.3-6.1	4.4-8.6
		III	9.6-11.4	11.2-14.6	10.9-15.8	11.3-17.8	8.4-15.1	8.9-17.1
		IV	3.4-5.2	4.4-7.4	4.4-7.7	5.4-9.2	2.4-6.1	4.6-8.2
		V	6.9-9.1	9.6-13.1	10.5-14.6	12.4-17.1	7.1-14.8	12.1-17.5
12	3.5	I	8.7-12.8	13.9-16.9	16.5-19.9	17.6-21.2	15.8-18.8	15.3-18.5
		II	6.2-9.5	7.7-13.1	9.3-14.4	10.3-15.2	8.7-13.9	8.8-13.7
		III	11.1-16.2	13.5-20.8	16.1-24.2	16.5-26.1	12.9-24.2	12.1-24.5
		IV	5.8-8.1	7.5-10.3	9.3-13.1	10.5-14.1	9.2-12.6	9.4-12.9
		V	10.1-15.4	14.3-20.2	16.3-23.4	17.9-25.5	17.5-25.1	17.4-25.4
14	4.8	I	10.2-17.7	15.6-22.1	16.6-22.8	21.6-28.2	24.3-29.8	26.1-30.6
		II	5.9-13.1	6.2-18.4	5.7-17.2	7.3-18.5	8.1-21.4	9.4-23.3
		III	17.5-19.8	20.5-26.1	19.4-28.4	25.9-33.9	25.3-36.3	25.1-38.1
		IV	5.1-9.7	6.1-11.2	6.2-11.7	7.6-12.1	8.3-15.1	10.1-17.8
		V	8.8-15.5	17.2-22.7	18.6-25.8	18.7-30.7	23.4-33.5	27.8-36.6
16	6.2	I	10.2-19.4	15.8-25.9	19.1-29.6	17.6-29.8	19.6-31.9	20.2-32.7
		II	6.8-16.8	8.2-21.5	9.3-21.3	7.9-21.6	9.8-21.9	9.8-22.2
		III	20.2-22.7	24.7-29.8	28.3-34.3	26.4-36.1	28.3-39.2	28.6-40.8
		IV	6.1-10.7	7.9-13.1	9.6-18.5	8.5-16.1	10.6-19.3	9.7-16.8
		V	9.8-16.6	16.7-24.5	16.8-30.1	18.2-32.3	19.2-35.4	22.6-35.4
18	7.8	I	7.7-17.3	16.3-27.1	21.3-32.7	25.6-35.7	28.1-36.7	25.8-39.6
		II	8.5-12.4	11.4-19.51	12.1-19.5	14.1-19.6	4.2-19.6	16.1-25.3
		III	15.5-24.8	26.8-35.9	32.1-43.1	34.2-48.3	35.6-50.5	38.9-52.2
		IV	7.9-12.1	10.9-18.8	12.2-20.1	14.5-21.7	14.6-21.7	16.9-25.9
		V	16.1-22.7	26.1-39.5	30.9-41.1	33.6-45.1	33.4-45.2	37.2-48.7

Table 6 Cables and heating strategies in two different experimental cases.

	Case-I (Separate cables)	Case-II (Composite cable)
Heating cable	H-cable	T1-cable
Sensing cable	T1- and T2-cables	T1- and T2-cables
Heating power	7.6 W/m	7.6 W/m
Heating time	150 minutes	150 minutes

Table 7 Results of destructive and non-destructive tests.

Group	Sample ID	Top (mbsl)	Bottom (mbsl)	ρ_{sat}	ρ_{dry}	V_{psat} (km/s)	ϕ	w (%)	V_{pdry} (km/s)	*UCS* (MPa)	*BTS* (MPa)
Group-A	A1	33.83	33.93	2.64	×	4.87	×	×	×	103.77	×
	A2	34.12	34.22	2.61	×	4.87	×	×	×	144.31	×
	A3	34.42	34.52	2.63	×	4.82	×	×	×	124.78	×
	A4	34.52	34.62	2.62	×	4.75	×	×	×	142.09	×
	A5	37.20	37.30	2.63	×	4.83	×	×	×	107.38	×
	A6	37.30	37.40	2.66	2.62	4.55	1.33	1.33	4.47	109.00	×
	A7	37.44	37.54	2.64	2.61	5.05	0.28	0.90	4.67	170.00	×
	A8	37.54	37.64	2.65	2.62	4.83	2.68	1.08	4.67	178.00	×
	A9	37.64	37.74	2.64	2.61	4.89	3.67	1.03	4.75	192.30	×
	A10	37.74	37.84	2.63	2.61	4.87	4.15	1.05	4.75	182.63	×
Average				2.64	2.61	4.83	2.42	1.08	4.66	145.43	
Group-B	A11	38.38	38.43	2.66	×	5.28	×		×	×	6.88
	A12	38.43	38.48	2.63	×	4.86	×		×	×	6.72
	A13	38.48	38.53	2.63	×	4.78	×		×	×	6.62
	A14	38.53	38.58	2.64	×	5.28	×		×	×	6.93
	A15	38.59	38.64	2.67	2.65	5.29	0.44	0.69	5.09	×	11.35
	A16	38.73	38.78	2.67	2.65	5.08	0.87	0.79	4.95	×	8.89
	A17	38.78	38.83	2.67	2.66	5.43	0.46	0.52	5.32	×	12.57
	A18	38.93	38.98	2.61	2.58	4.82	2.68	1.21	4.70	×	7.67
Average				2.65	2.64	5.10	1.11	0.80	5.02		8.45
Group-C	A19	39.10	39.16	2.65	2.63	5.39	0.24	0.74	5.19	175.34	×
	A20	39.16	39.23	2.63	2.60	4.96	2.61	1.12	4.86	111.91	×
	A21	39.24	39.30	2.70	2.67	4.90	0.63	0.97	4.63	186.48	×
	A22	39.30	39.37	2.68	2.66	5.51	2.52	0.60	5.34	154.35	×
	A23	39.37	39.43	2.63	2.60	5.04	4.63	1.02	4.93	141.08	×
	A24	39.47	39.54	2.65	2.62	5.06	6.33	0.96	4.89	246.11	×
	A25	39.83	39.90	2.69	2.67	5.43	4.82	0.55	5.35	115.51	×
	A26	40.00	40.07	2.67	2.65	5.33	0.34	0.69	5.18	176.50	×
	A27	42.52	42.58	2.61	2.57	4.81	5.41	1.42	4.71	241.05	×
	A28	44.70	44.76	2.62	2.58	4.90	5.05	1.33	4.76	230.90	×
Average				2.65	2.63	5.13	3.26	0.94	4.98	177.92	
Group-D	A29	31.83	31.87	2.66	2.63	4.96	3.17	1.04	4.81	170.03	×
	A30	31.87	31.92	2.66	2.64	5.44	0.46	0.69	5.13	206.96	×
	A31	32.45	32.49	2.65	2.62	4.76	2.87	1.22	4.52	116.37	×
	A32	32.78	32.82	2.65	2.63	4.94	3.44	0.99	4.66	127.07	×
	A33	32.82	32.86	2.67	2.65	5.06	1.97	0.82	4.83	193.00	×
	A34	32.90	32.94	2.67	2.65	5.05	3.34	0.91	4.84	199.60	×
	A35	33.60	33.64	2.61	2.56	4.59	4.80	1.80	4.45	188.87	×
	A36	33.64	33.68	2.64	2.61	4.90	3.87	1.04	4.69	180.00	×
	A37	33.70	33.74	2.67	2.65	5.34	1.63	0.75	5.04	229.04	×
	A38	33.74	33.78	2.61	2.57	4.69	4.91	1.74	4.50	197.27	×
	A39	33.79	33.83	2.65	2.63	4.97	5.14	1.01	4.69	238.11	×
Average				2.65	2.62	4.97	3.24	1.09	4.74	186.03	
Maximum (A1-A39)				2.70	2.67	5.51	6.33	1.80	5.35	206.96 (sat) 246.11 (dry)	6.93 (sat) 12.57 (dry)
Minimum (A1-A39)				2.61	2.56	4.55	0.24	0.52	4.45	103.77 (sat) 109.00 (dry)	6.62 (sat) 7.67 (dry)
Average (A1-A39)				2.65	2.62	5.00	2.82	1.00	4.85	150.28 (sat) 191.68 (dry)	6.79 (sat) 10.12 (dry)

Table 8 Description of selected water flow and high-saturation zone.

Zones	Depth (mbgs)	Maximum temperature change (ΔT_{max}) after 180 minutes of heating (°C)	Fractures and lithological description
Water-flow	8.87-9.12	7.3	Vertical fracture, boundary between muddy sand and black shale
	15.47-15.57	14.7	Vertical fracture within sandy shale
	29.92-30.17	8.9	Vertical and horizontal fracture within shale
	35.47-35.72	6.3	Loose gravel and soil
	38.02-38.27	11.4	Vertical fracture within sandy shale
	41.475-41.675	10.9	Horizontal fracture within pure black shale
	43.075-43.175	11.2	Highly weathered and fractured sandy shale
	46.025-46.325	6.5	Fractured black shale
High-saturation zone	2.0-7.3	3.5	Highly weathered and fractured sandy shale, thin clay layers intercalated, presence of loose materials
	10.77-11.52	6.5	Gravel and soil-like material
	20.32-20.67	8.7	Horizontal fracture within shale
	21.07-25.47	9.2	Intense horizontal cracks within sandy shale

Table 9 Thermal conductivity values of rocks determined from laboratory measurements and AH-DFOS tests.

Depth (m)	λ_r [W/mK]	λ_a [W/mK]	Lithological description
32.32─32.43	2.73	2.74	Sharp boundary between shale and sandstone
32.55─32.65	2.86	2.97	Shale
33.50─33.59	2.63	2.7	Fine- to medium-grained sand
39.00─39.09	2.58	2.63	Medium-grained fresh sandstone
39.55─39.64	2.58	2.71	Medium-grained fresh sandstone
39.65─39.74	2.63	2.65	Medium-grained fresh sandstone with scattered mud clasts
39.75─39.83	2.58	2.52	Coarse-grained sandstone with mud balls
39.90─40.0	2.68	2.67	Coarse sandstone with scattered mud clasts and mud balls

Figures

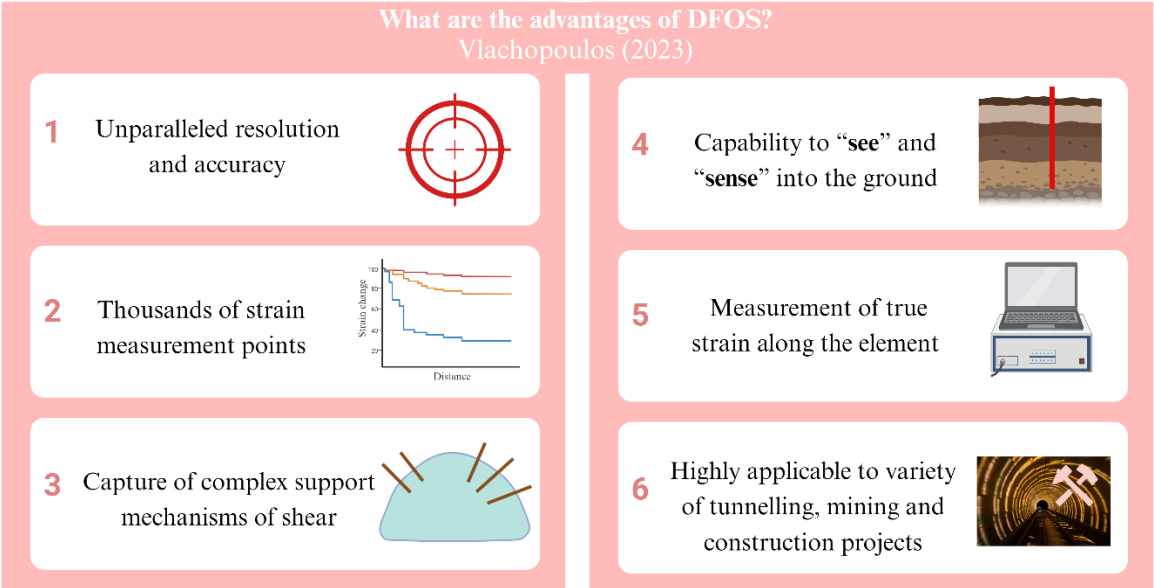

Figure 1 Various advantages of DFOS sensing methods summarised by Vlachopoulos (2023) after two decades of laboratory and field experiences.

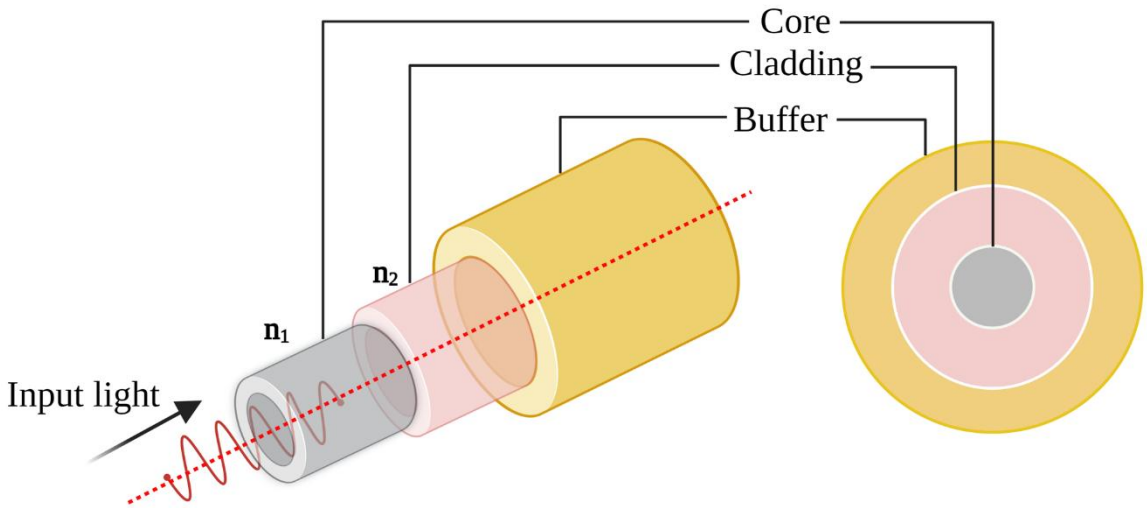

Figure 2 Structure of an optical fibre (n1 and n2 represent the core and cladding refractive index, respectively).

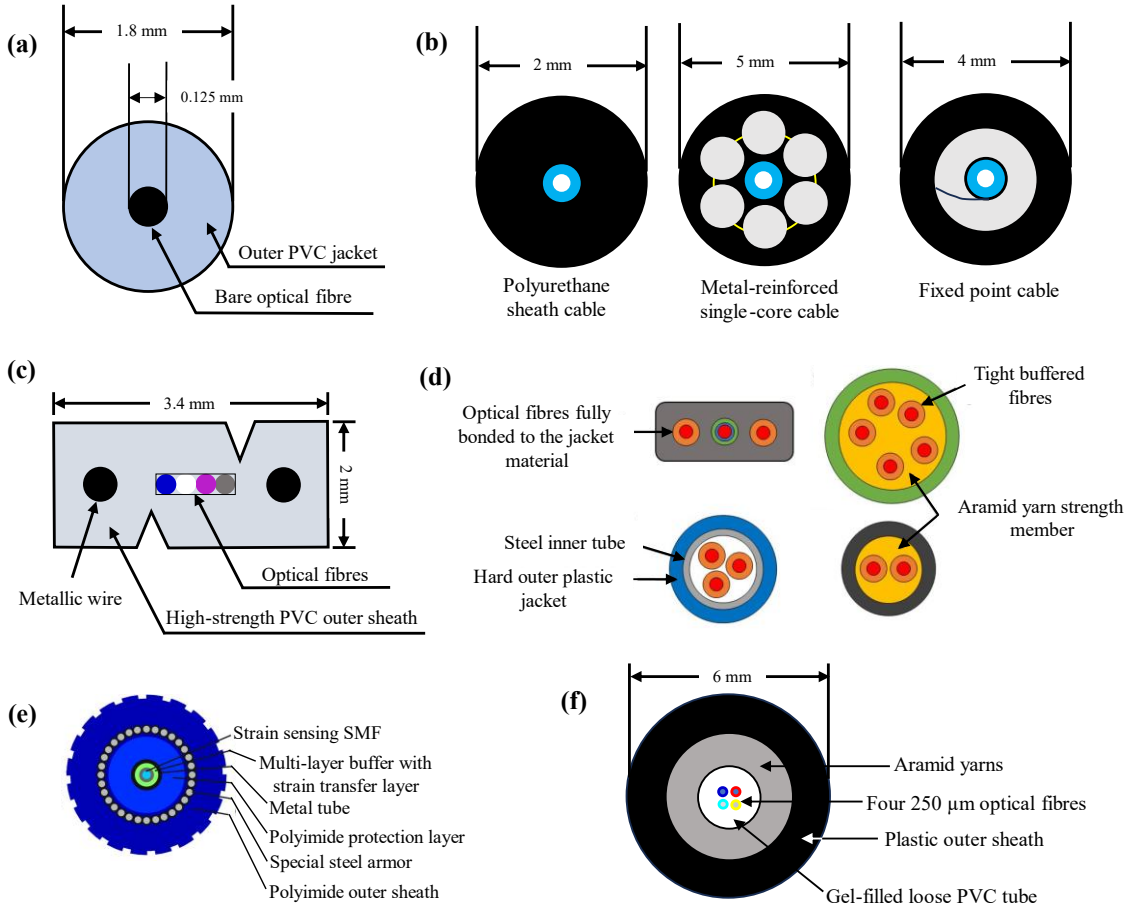

Figure 3 Schematic diagram of various FO cables employed in previous studies. (a) deformation monitoring of GFRP bar (a material composed of glass fibres, polymeric resins, and matrix materials) soil nails employing the BOTDA approach (Hong et al., 2016); (b) investigating the mechanism of land subsidence and the evaluation of soil compression deformation using BOTDR and FBG sensing methods (Wu et al., 2015); (c) monitoring strain changes in a landslide corresponding to rainfall using COTDR approach (Kogure and Okuda, 2018); (d) monitoring strain profile and crack growth in rock, cement, and brittle media employing BOTDA sensing techniques (Nowak et al., 2022); (e) driven ductile pile monitoring using Rayleigh backscattering principle (outer surface of this cables is structured to provide a solid connection with the surrounding grout material) (Monsberger et al., 2020); and (f) thermal integrity measurement of piles using BOTDR sensing method (Rui et al., 2017).

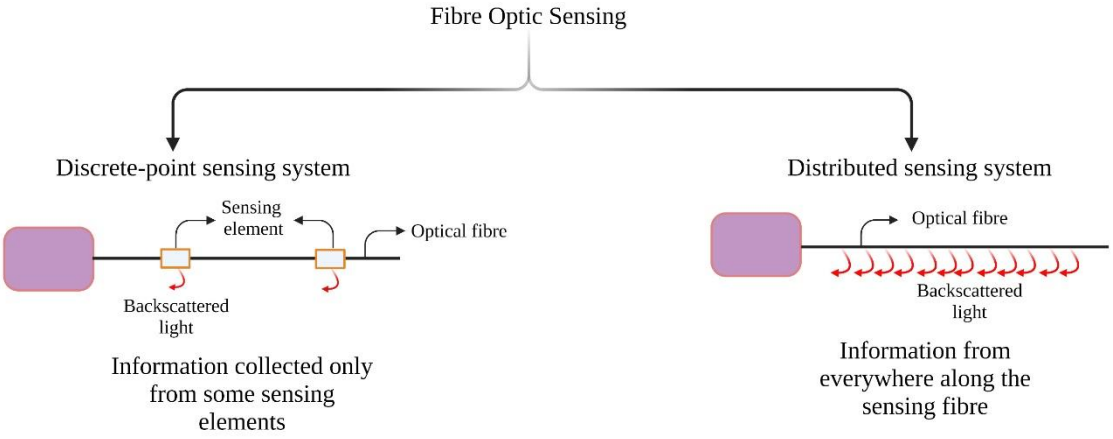

Figure 4 Types of FOS techniques.

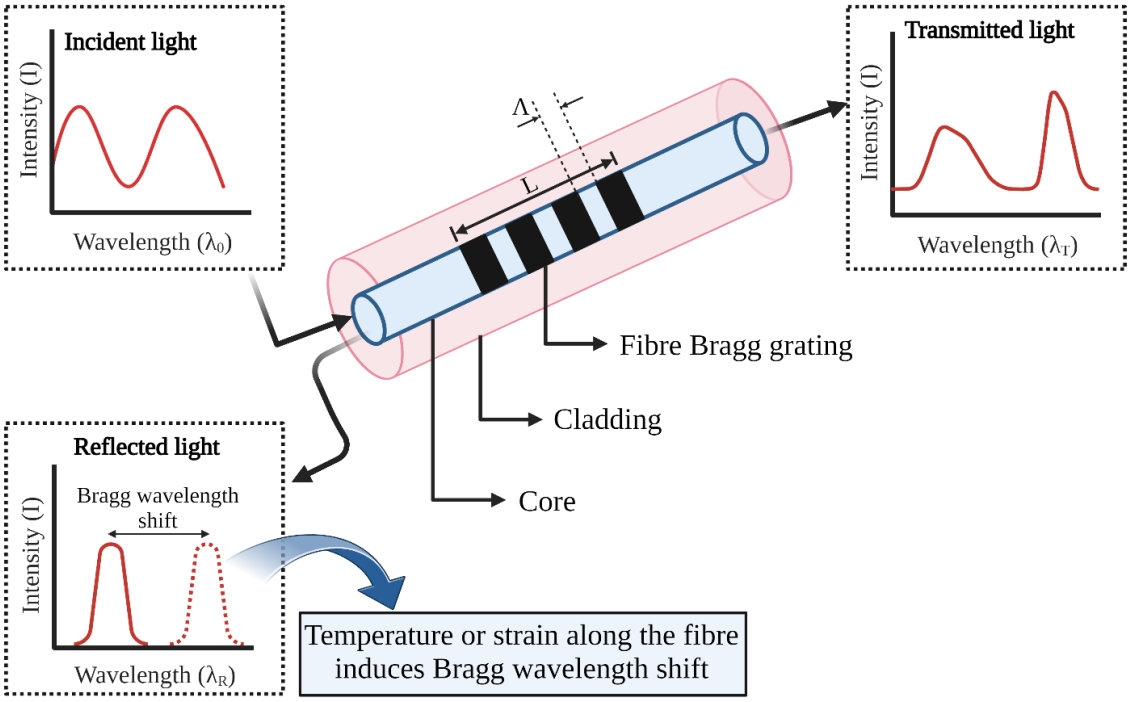

Figure 5 Working principle of an FBG sensor (Λ represents Bragg width; λ_0, λ_R, and λ_T are the wavelength of the incident, reflected, and transmitted light, respectively) (modified from Guo et al., 2020) (modified from Guo et al., 2020).

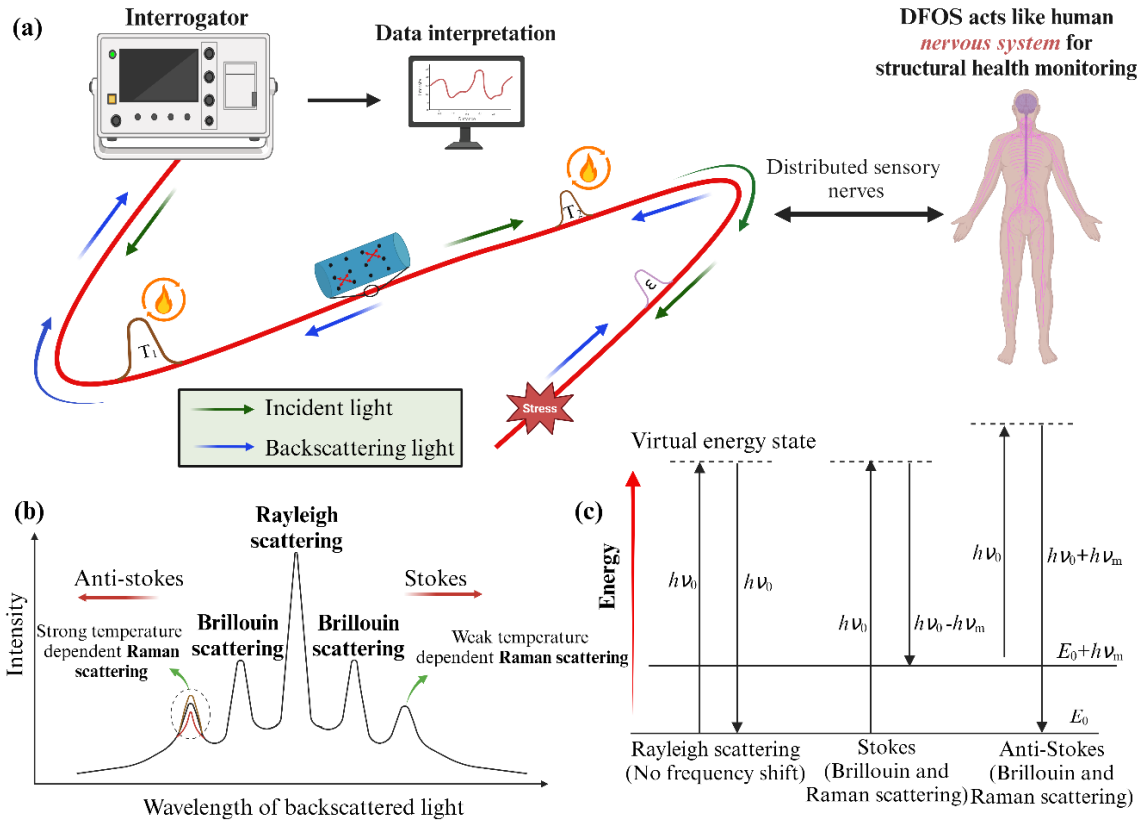

Figure 6 (a) Basic illustration of the DFOS method (Zhu et al., 2023); (b) three different backscattering components along the fibre core; and (c) change of energy states during backscattering processes.

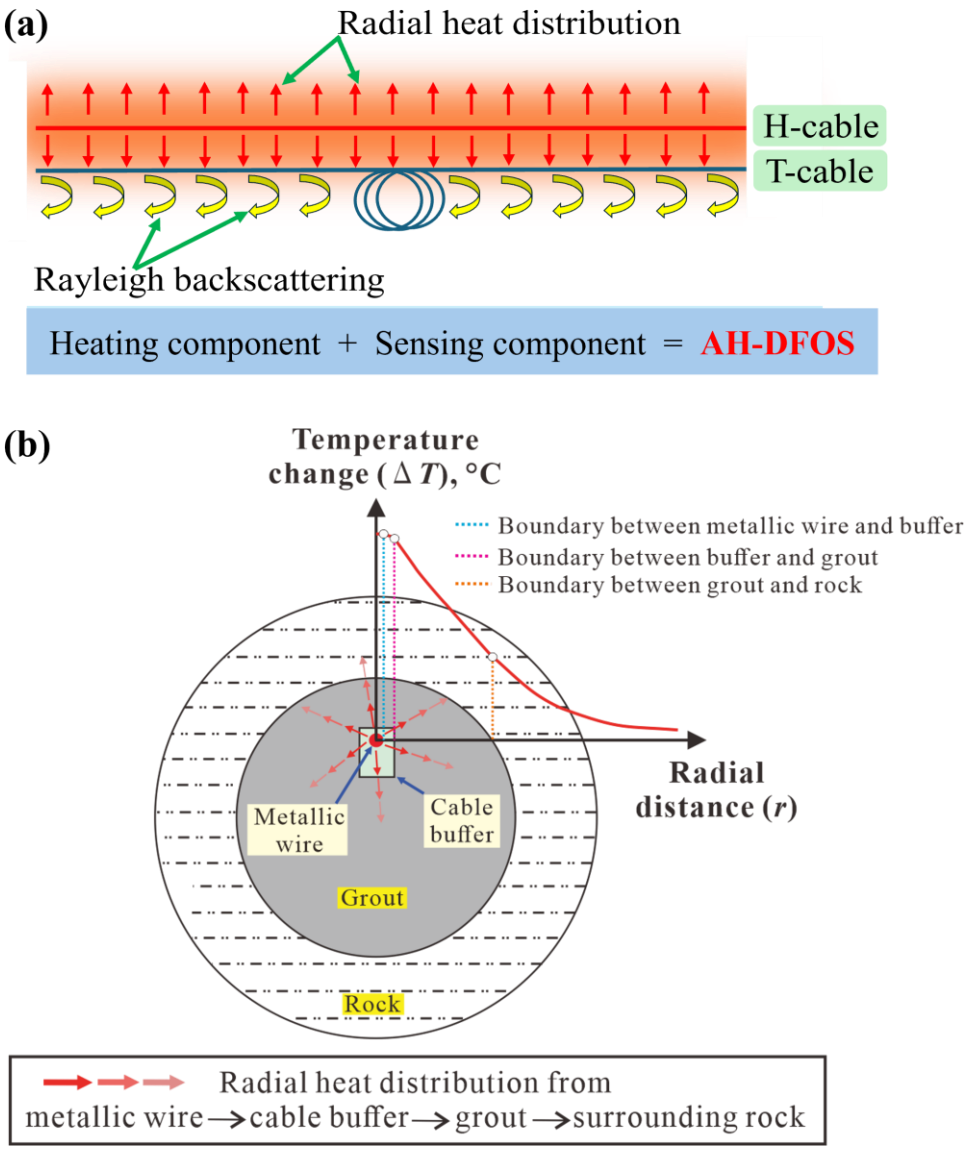

Figure 7 (a) Schematic diagram showing the AH-DFOS sensing method; and (b) sequential path of heat transfer from the metallic wire to the surrounding rocks.

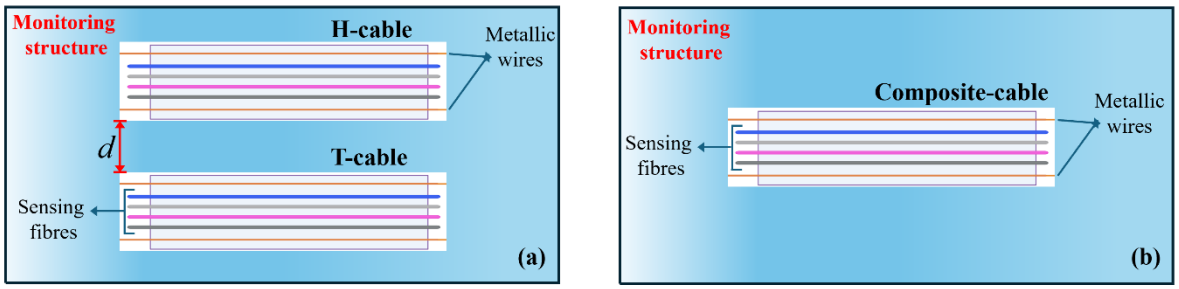

Figure 8 Schematic illustration showing the AH-DFOS sensing method (a) dual cable arrangement (*d* represents the relative distance between two cables); and (b) a composite cable configuration.

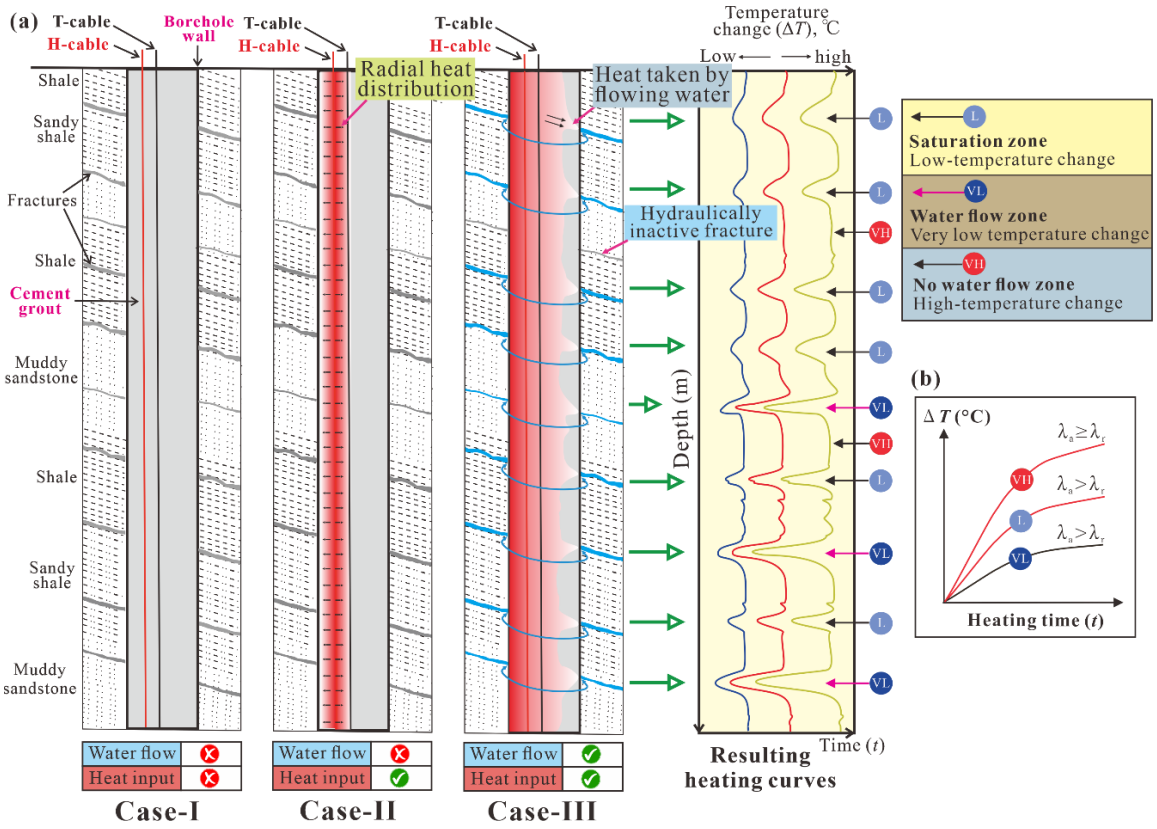

Figure 9 Conceptual illustration of a grouted borehole in a fractured sedimentary basin, demonstrating the application of the AH-DFOS method for characterising fractured aquifers.

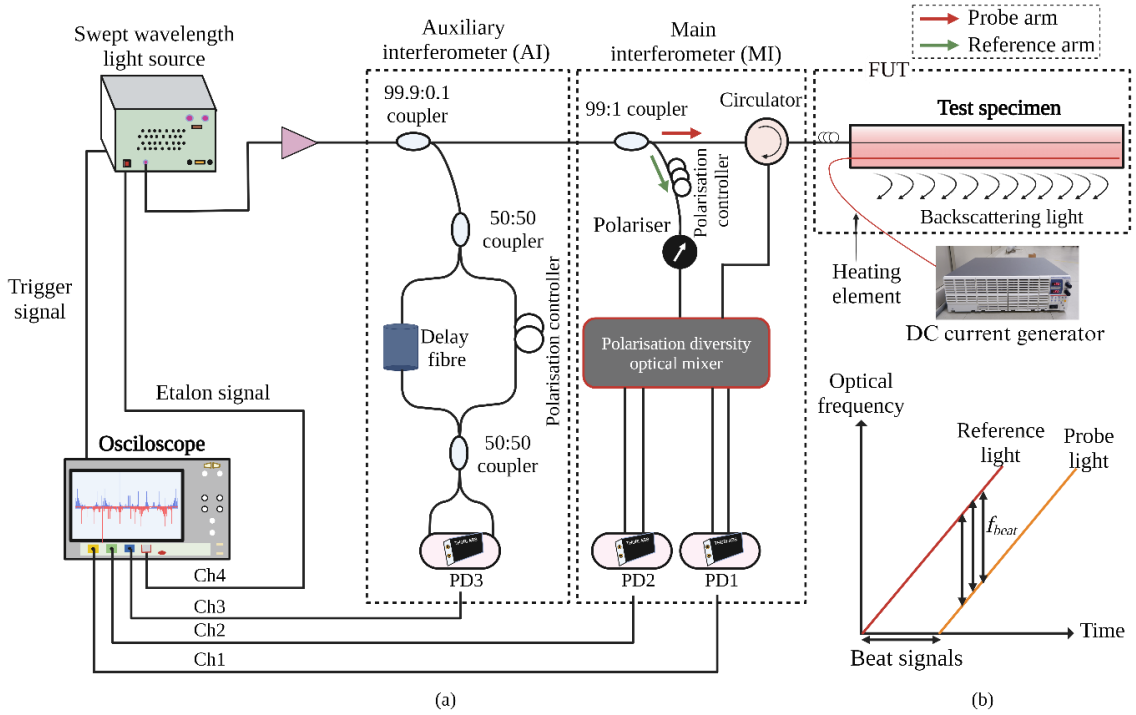

Figure 10 Configuration of the proposed OFDR sensing system: (a) operational principle of the PNC-OFDR sensing system; and (b) generation of beat signals.

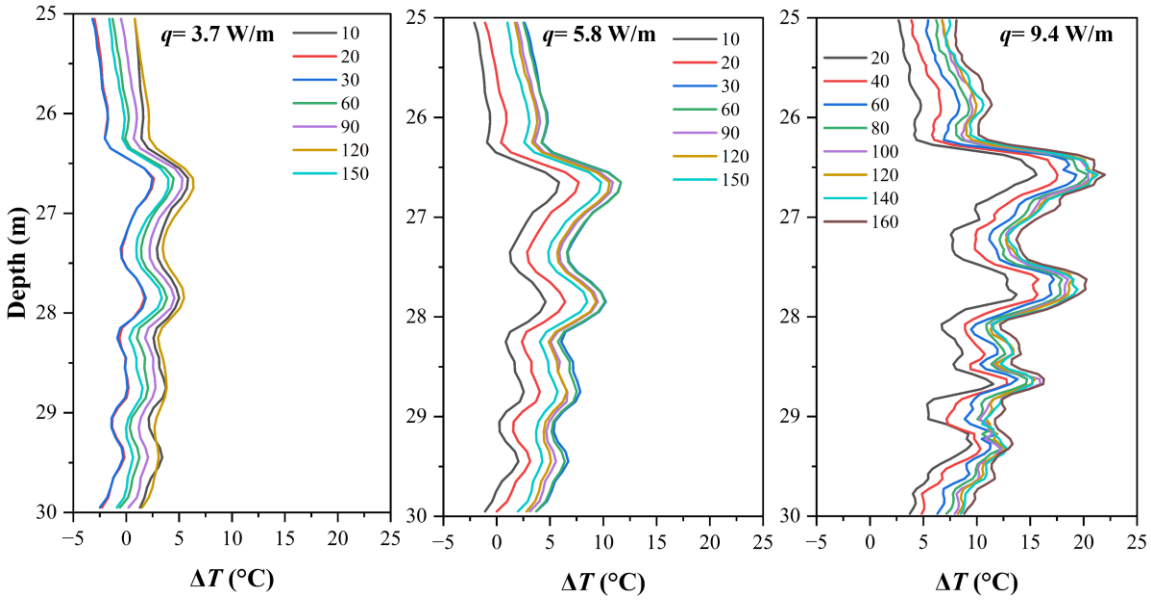

Figure 11 Heating curves resulting from three different heating powers (q=3.7, 5.8, and 9.4 W/m) (note that experiments were conducted at three different hydraulic conditions).

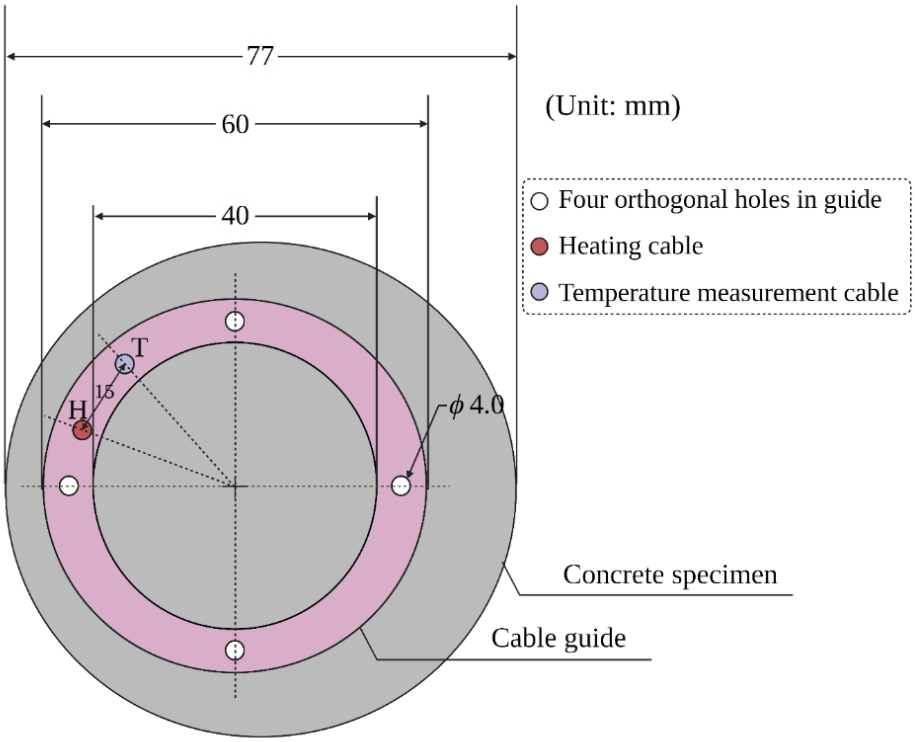

Figure 12 Cross-section of the concrete specimen with installed cables and cable guide.

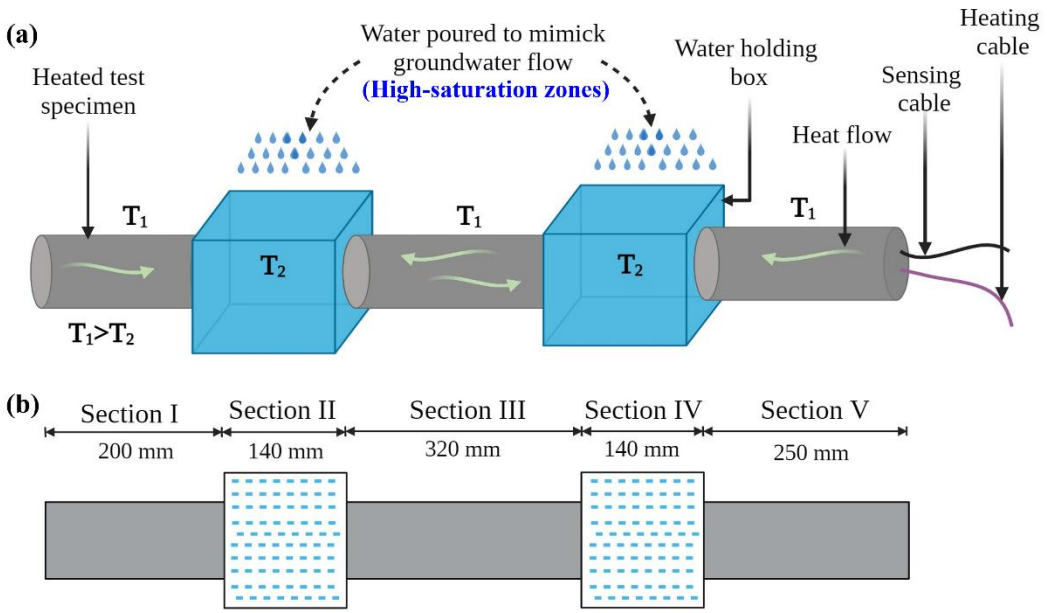

Figure 13 (a) Filling water inside the PET boxes (T1 and T2 represent the temperature of the water-supplied (high-saturation zones) and no-water-supplied sections (pure condution zones), respectively; T1>T2); and (b) top-view sketch of the specimen.

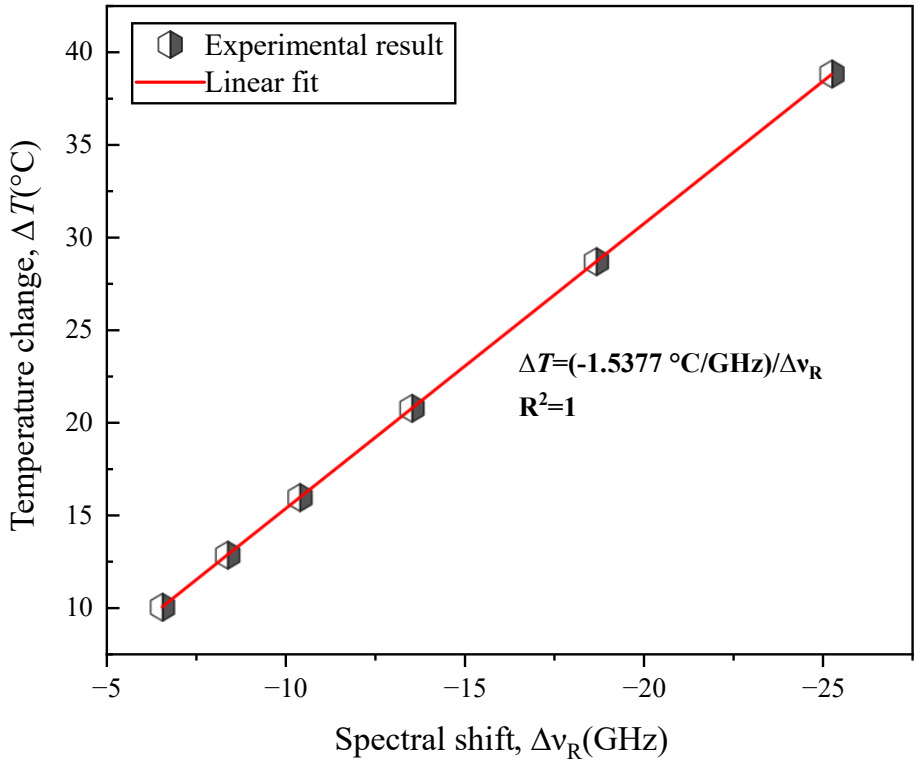

Figure 14 Rayleigh spectral shift measured by the PNC-OFDR system as a function of ΔT.

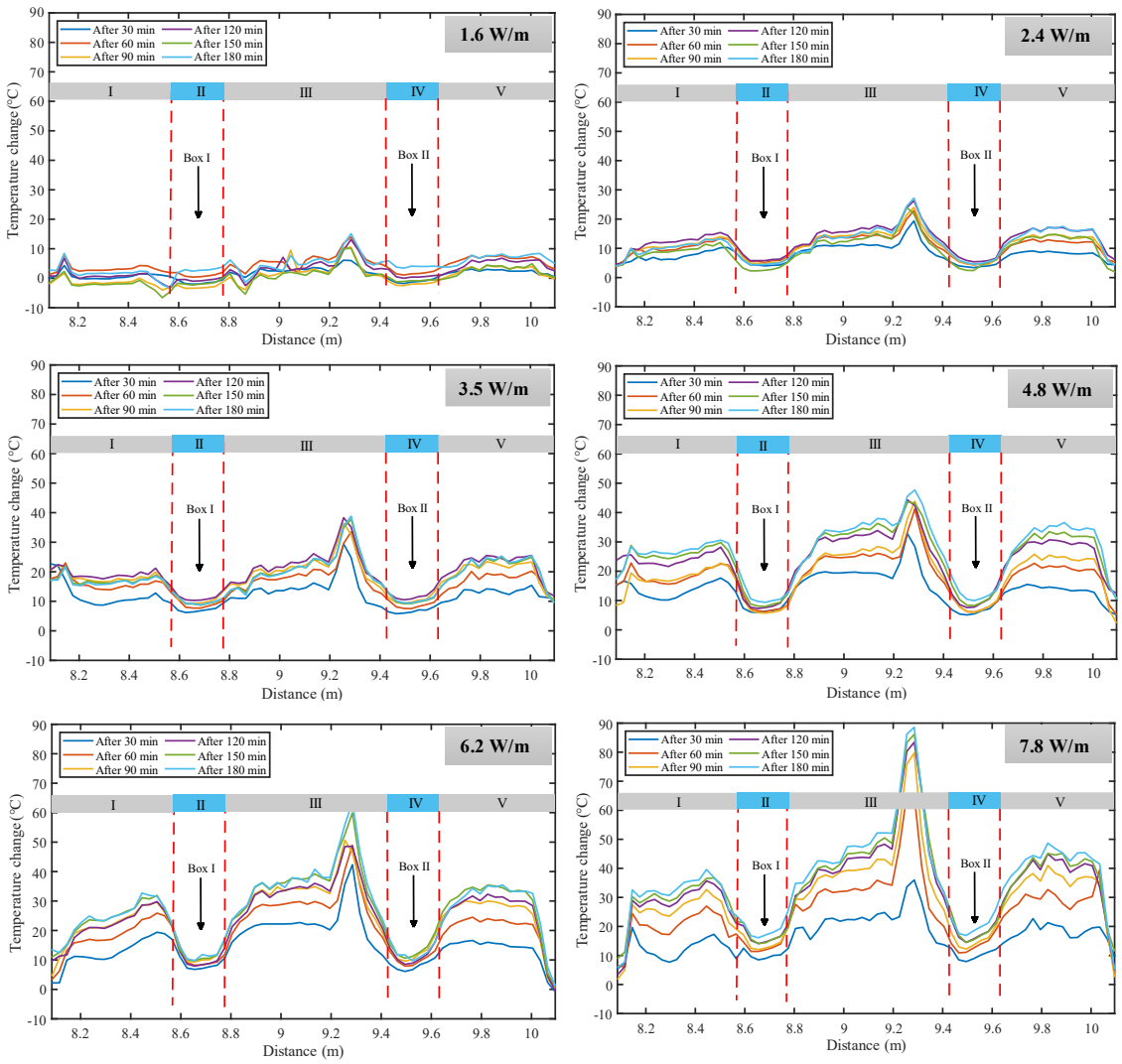

Figure 15 ΔT along the specimen detected by the PNC-OFDR system at six different heating powers for 3 hours.

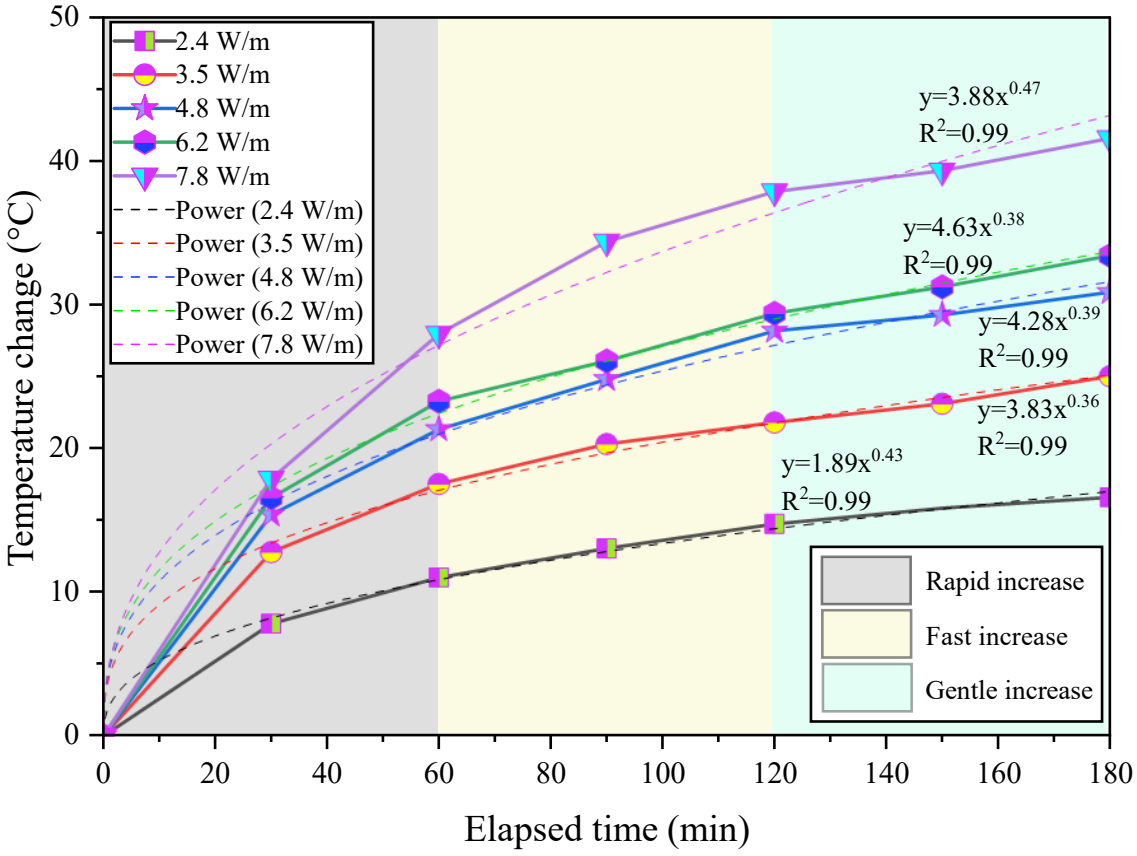

Figure 16 Trend of ΔT with time at different heating power (the average ΔT in section III was considered for the analysis, and a heating power of 1.6 W/m was excluded due to its tendency to induce random temperature fluctuations).

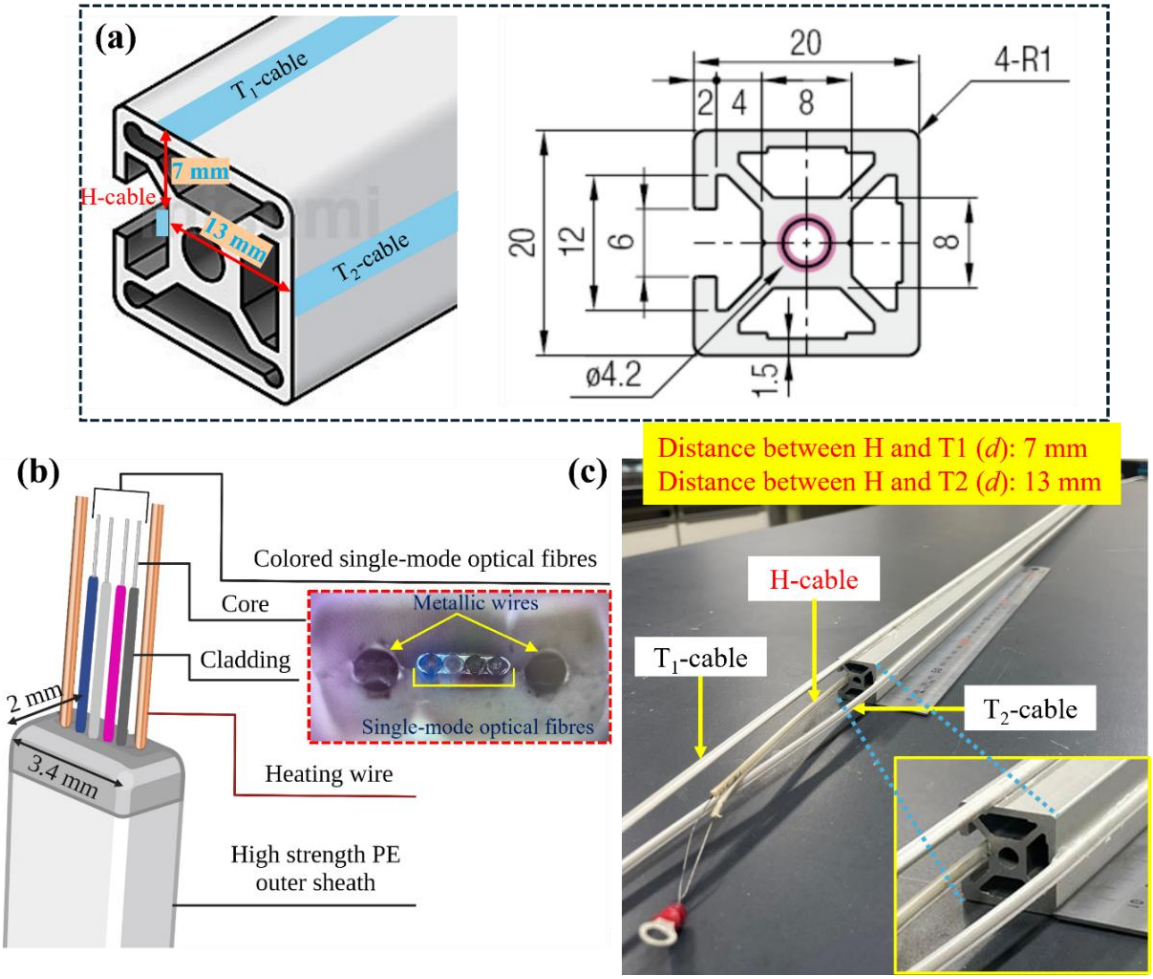

Figure 17 (a) 3D and cross-sectional view of the aluminium frame including the groove details that simulate the bolt in this study; (b) structure of the optical cable, and (c) final view of the instrumented bolt.

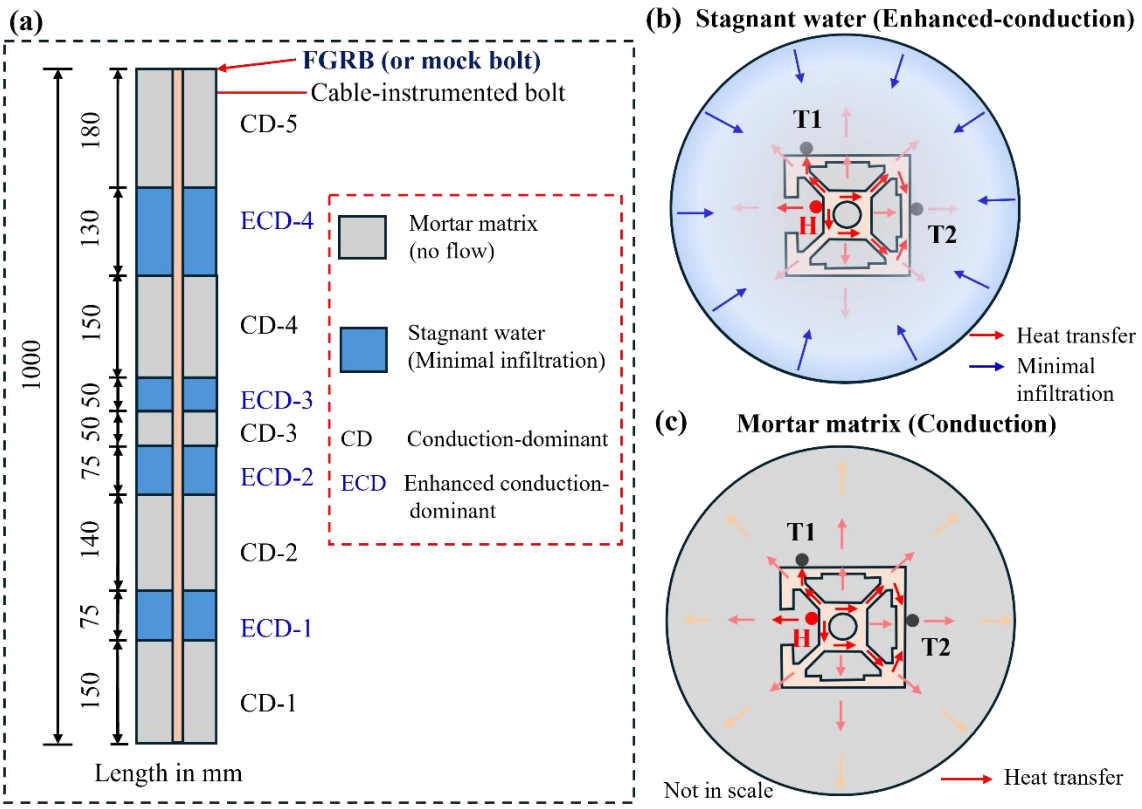

Figure 18 (a) Schematic representation of the experimental setup; (b) heat transfer dynamics in the presence of stagnant water (Case-I); and (c) radially distributed heat within mortar matrix in Case-II.

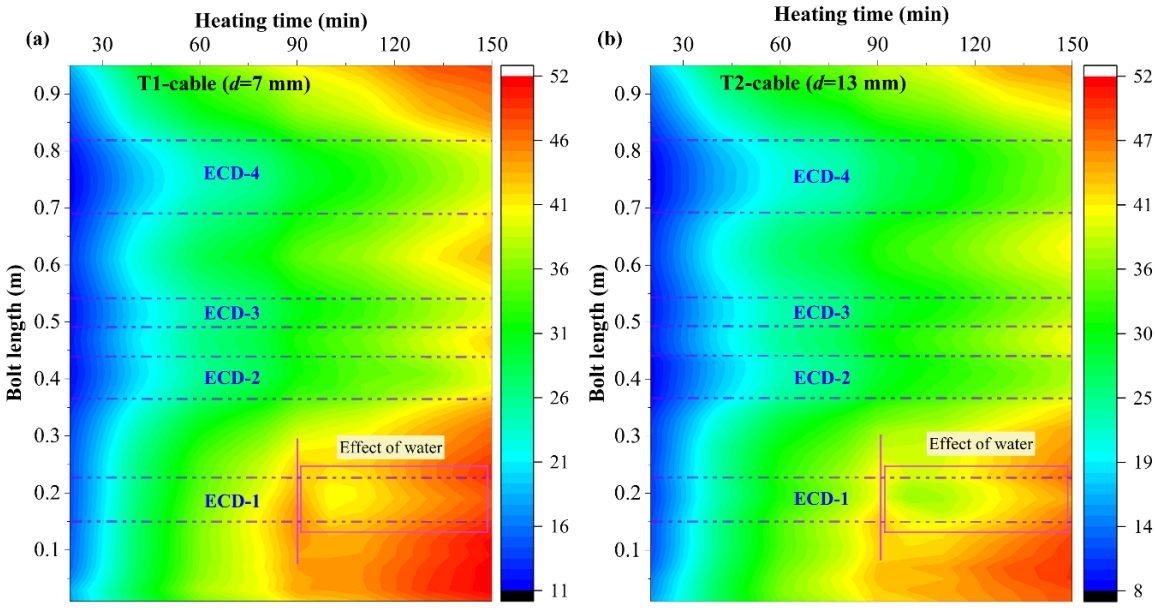

Figure 19 Thermal response in Case-I recorded by (a) T1-cable; and (b) T2-cable over 150 minutes of continuous heating. The parameter *d* represents the radial distance of T1- and T2-cables from the H-cable.

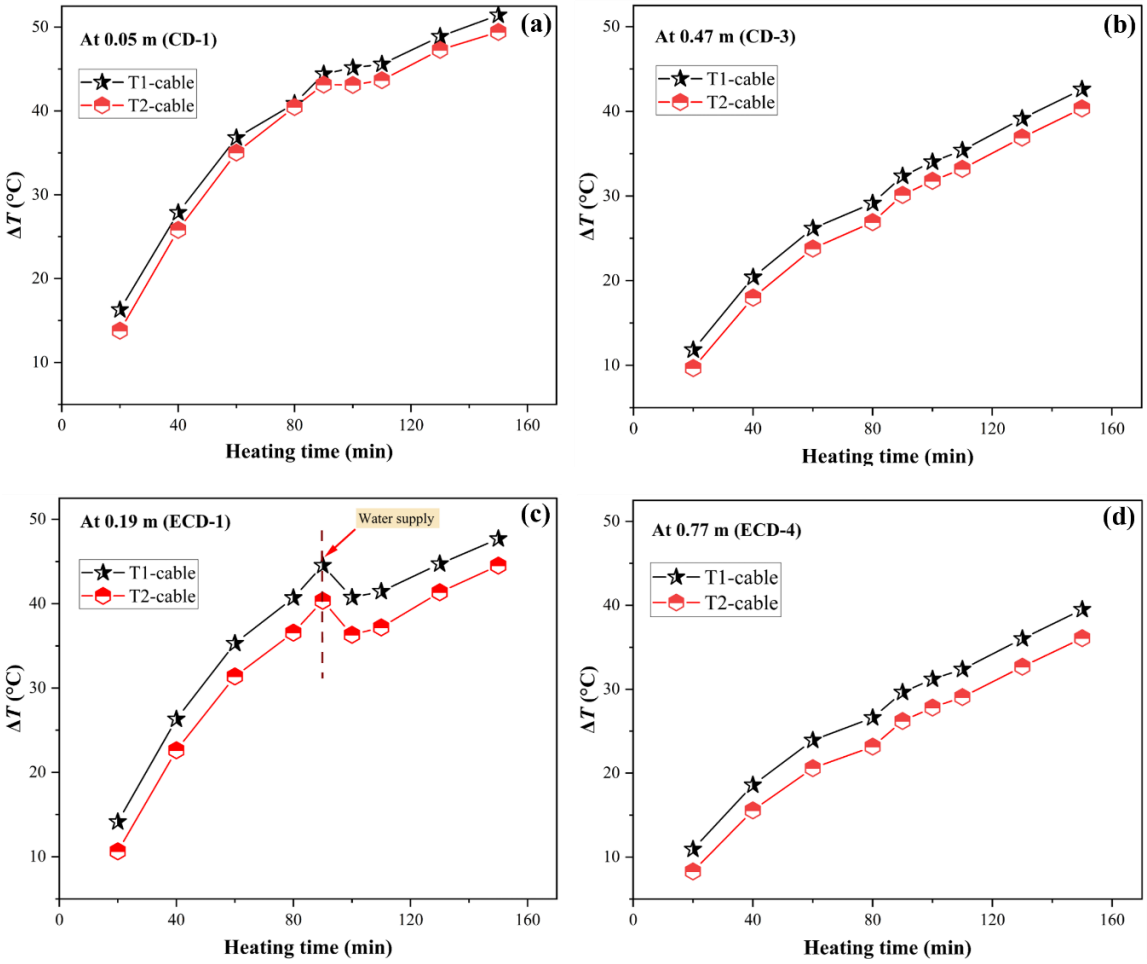

Figure 20 Temporal evolution of temperature during 150 minutes of active heating in Case-I at (a) CD-1; (b) CD-3; (c) ECD-1; and (d) ECD-4.

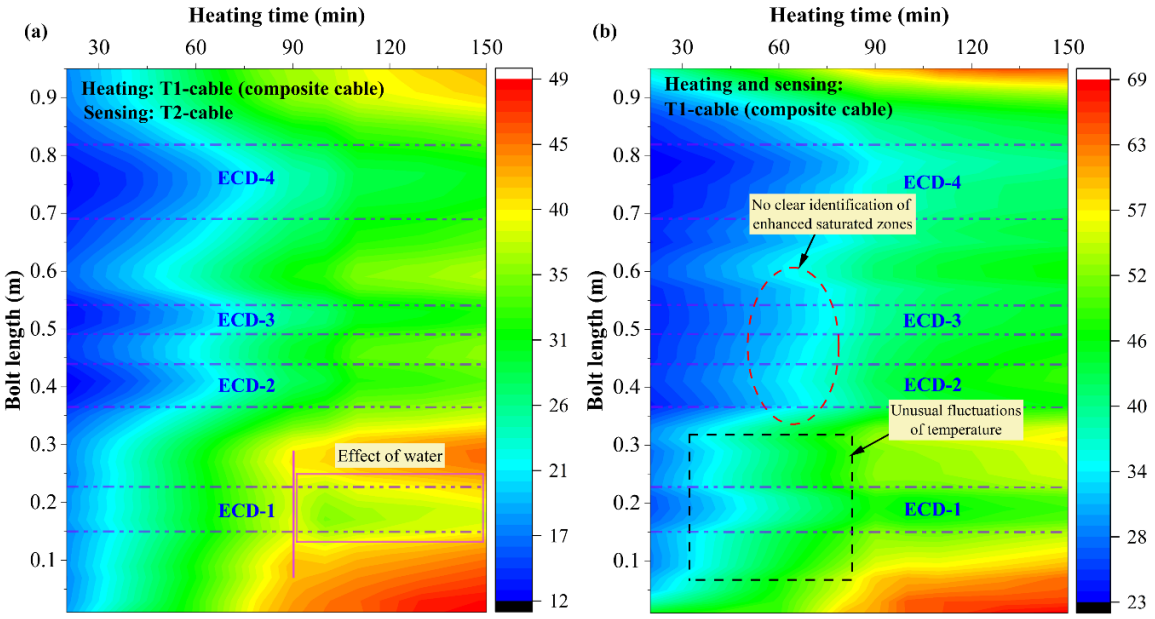

Figure 21 Thermal response curves in Case 2 recorded by (a) T2-cable; and (b) T1-cable (composite) over 150 minutes of continuous heating.

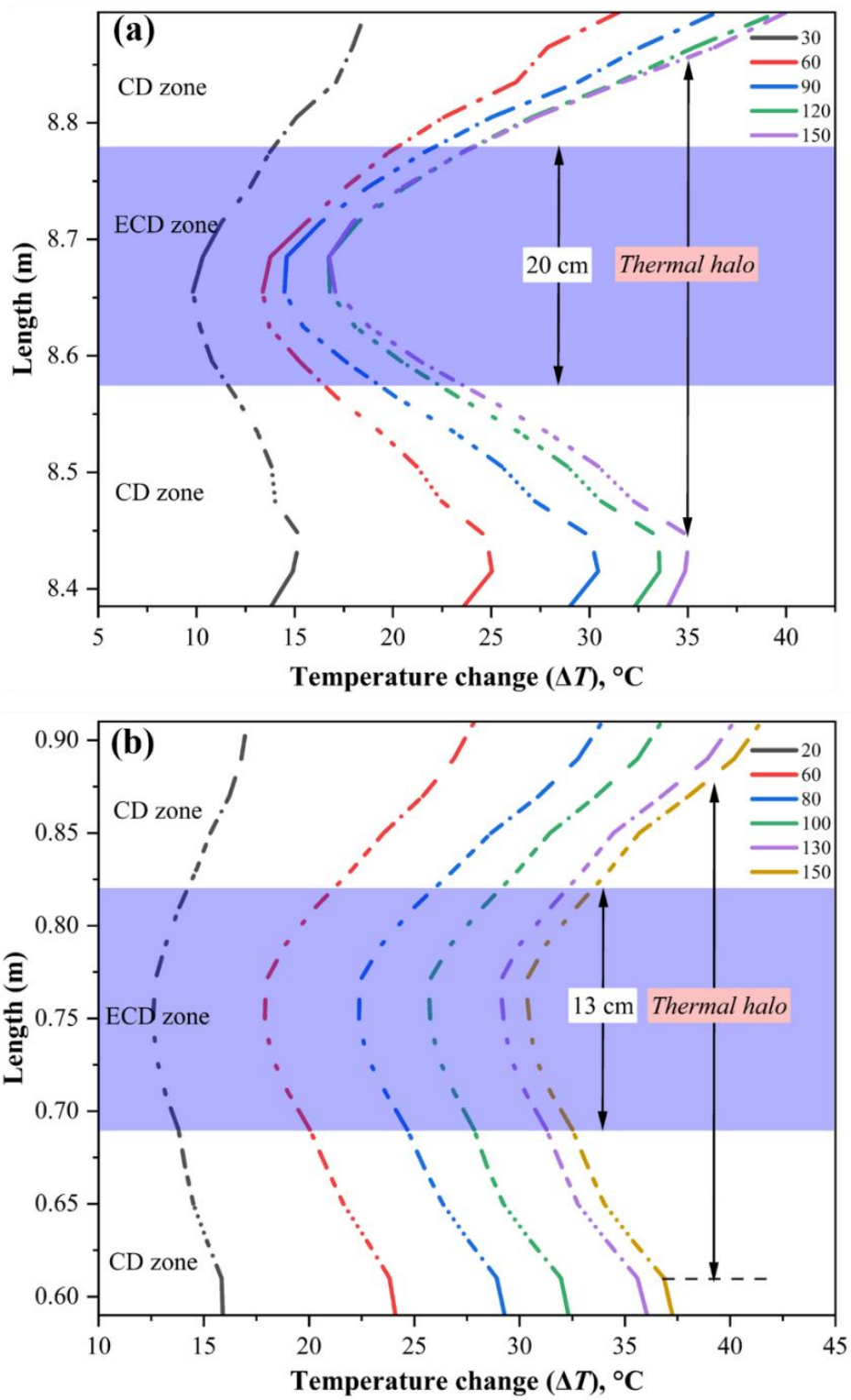

Figure 22 Thermal halo with low temperature rise: (a) from our previous study (Acharya et al., 2024); and (b) in this study (ECD-4).

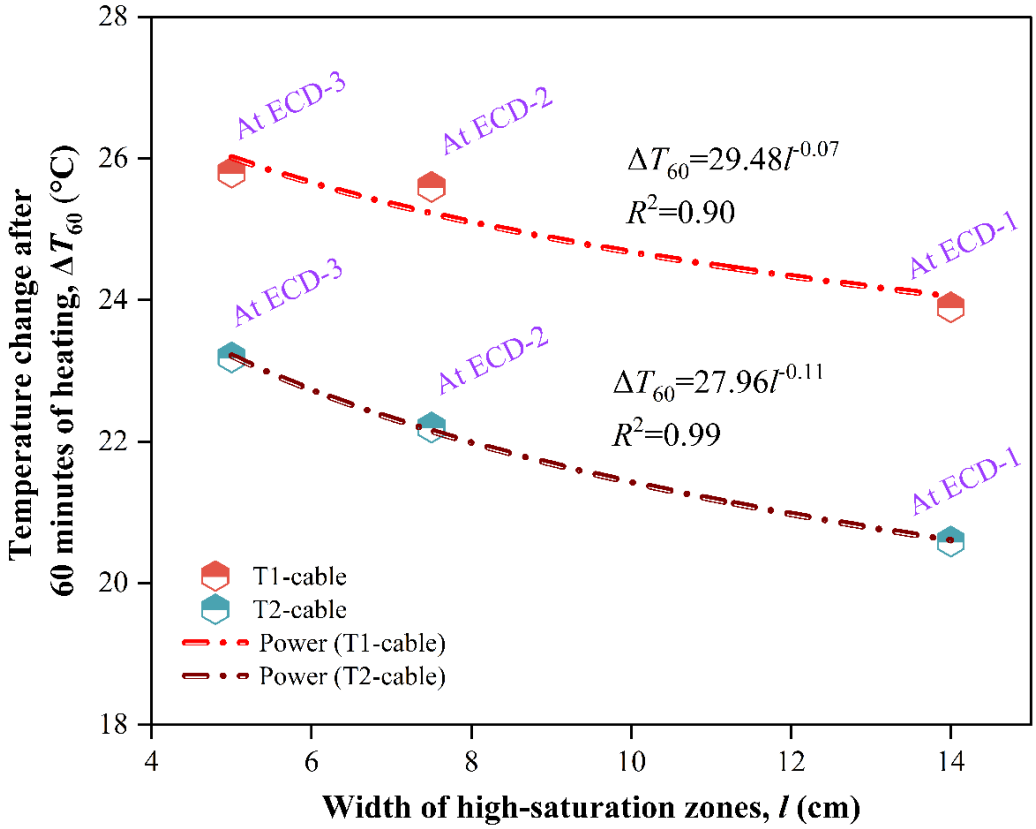

Figure 23 Relationship between the width of high-saturation zone (or fracture width in natural field applications) and ΔT after 60 minutes of heating.

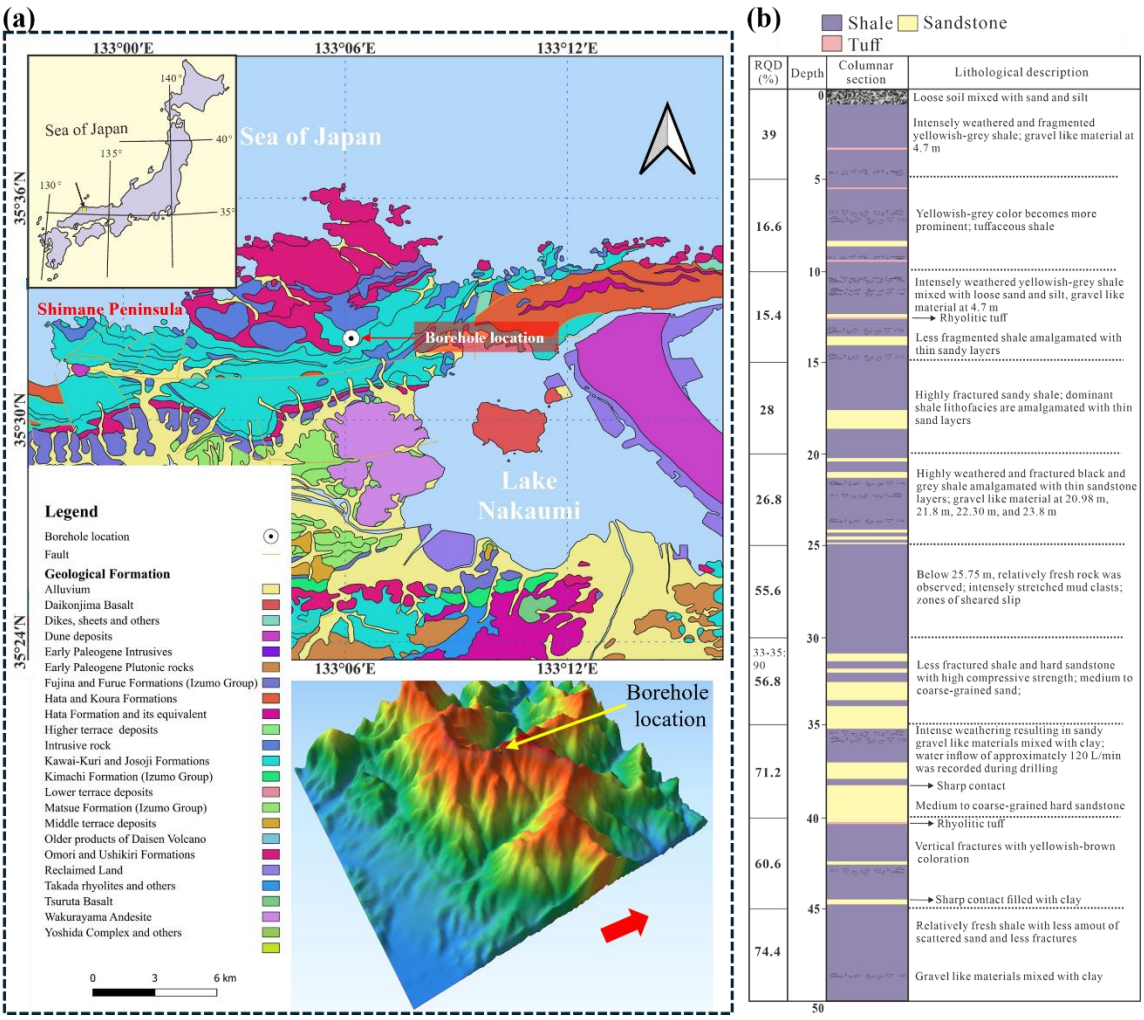

Figure 24 (a) Geological maps around the study site and the location of the borehole (source: Geological Society of Japan); and (b) columnar section of the borehole.

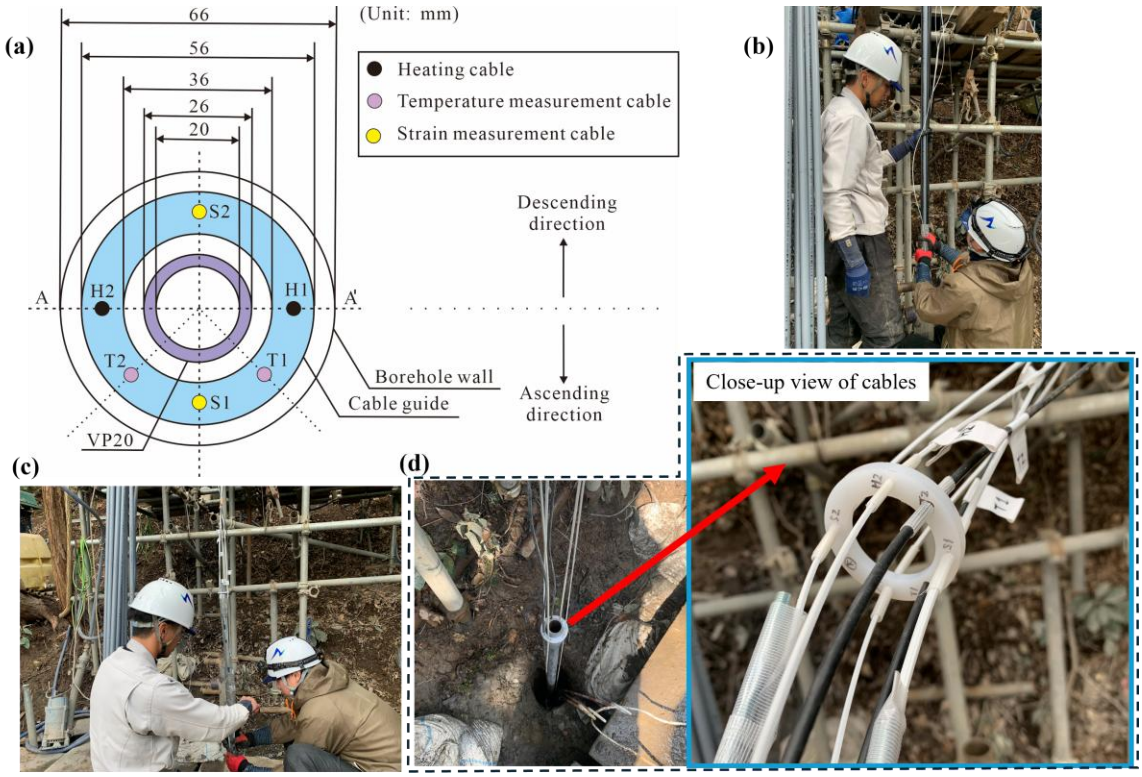

Figure 25 Various methods of FO cable installation for AH-DFOS method: (a) cross-section of borehole including cable configuration; (b) installation of cables inside borehole; (c) cement grouting; and (d) final close-up view of cables on the ground surface.

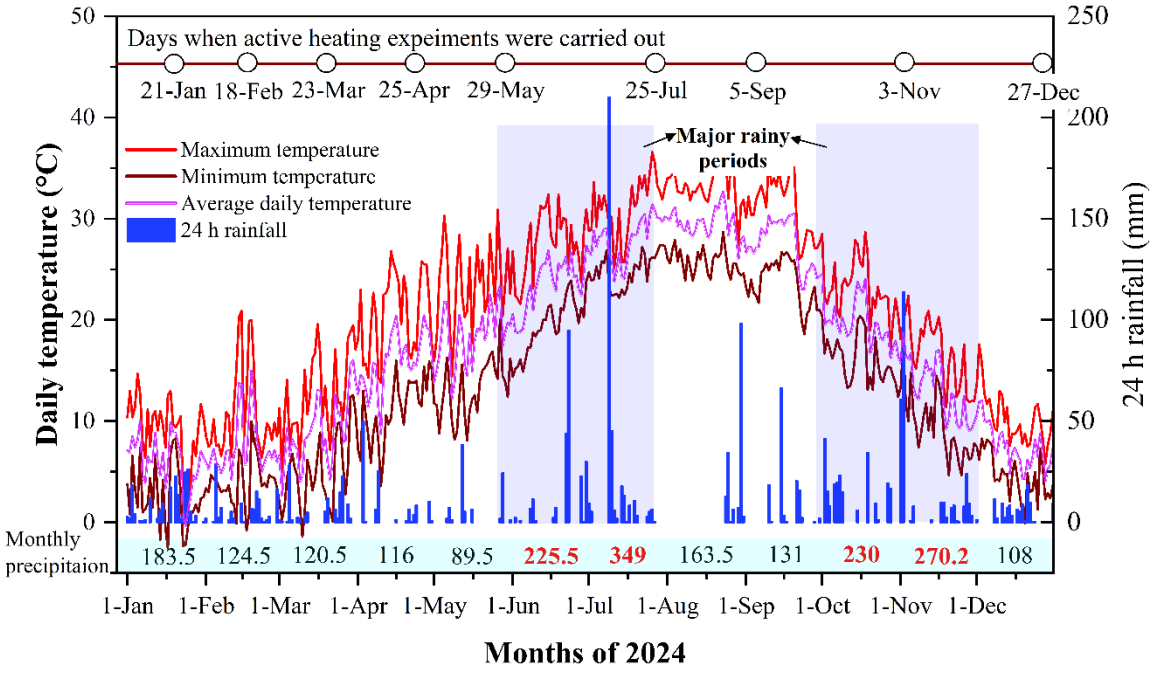

Figure 26 Daily weather conditions at the test site throughout 2024, including maximum, minimum, and average air temperatures (°C), along with 24-hour rainfall (mm).

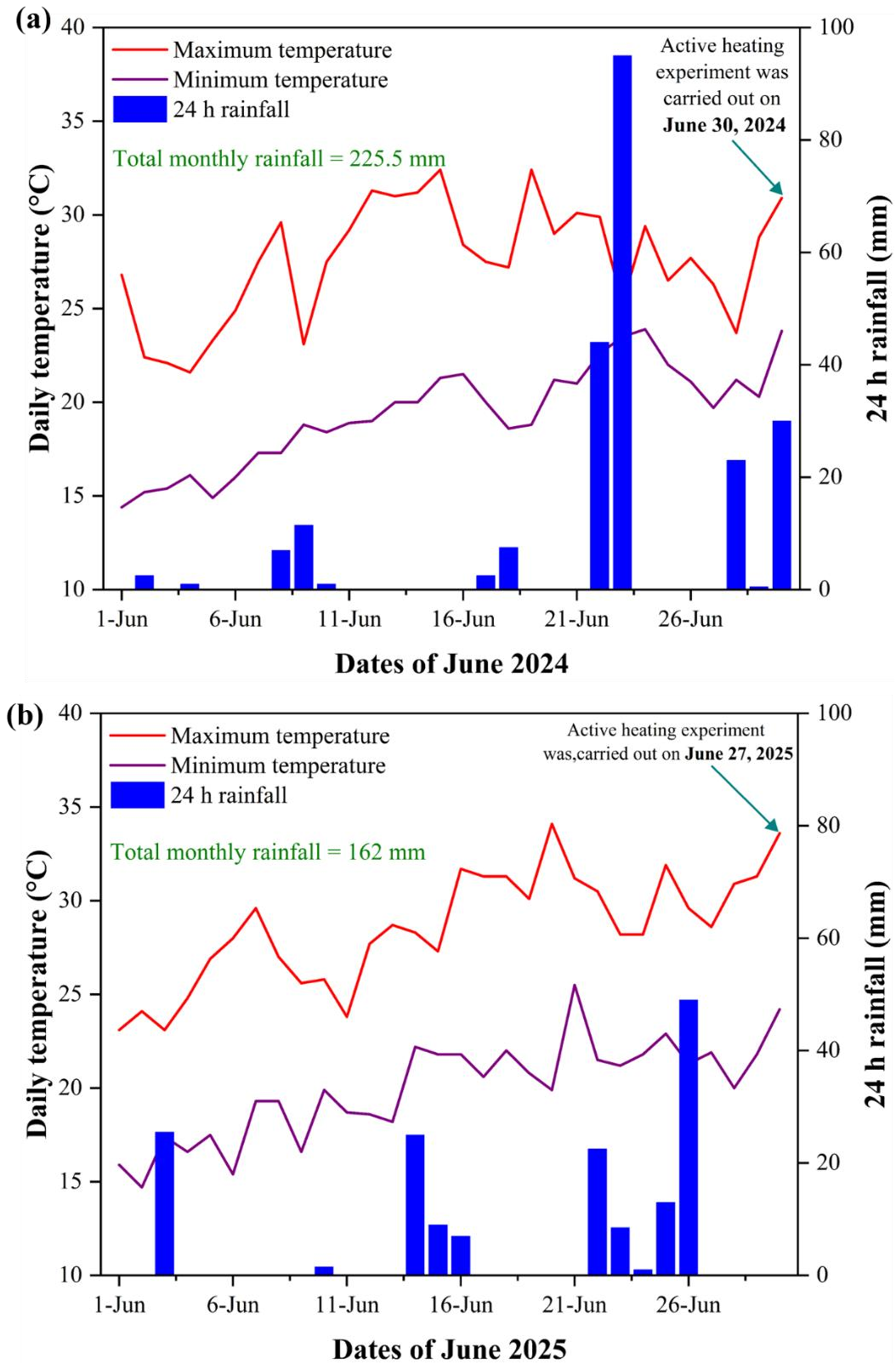

Figure 27 Comparison of daily weather conditions during June 2024 (a); and June 2025 (b), showing maximum and minimum air temperatures (°C) and 24-hour rainfall (mm).

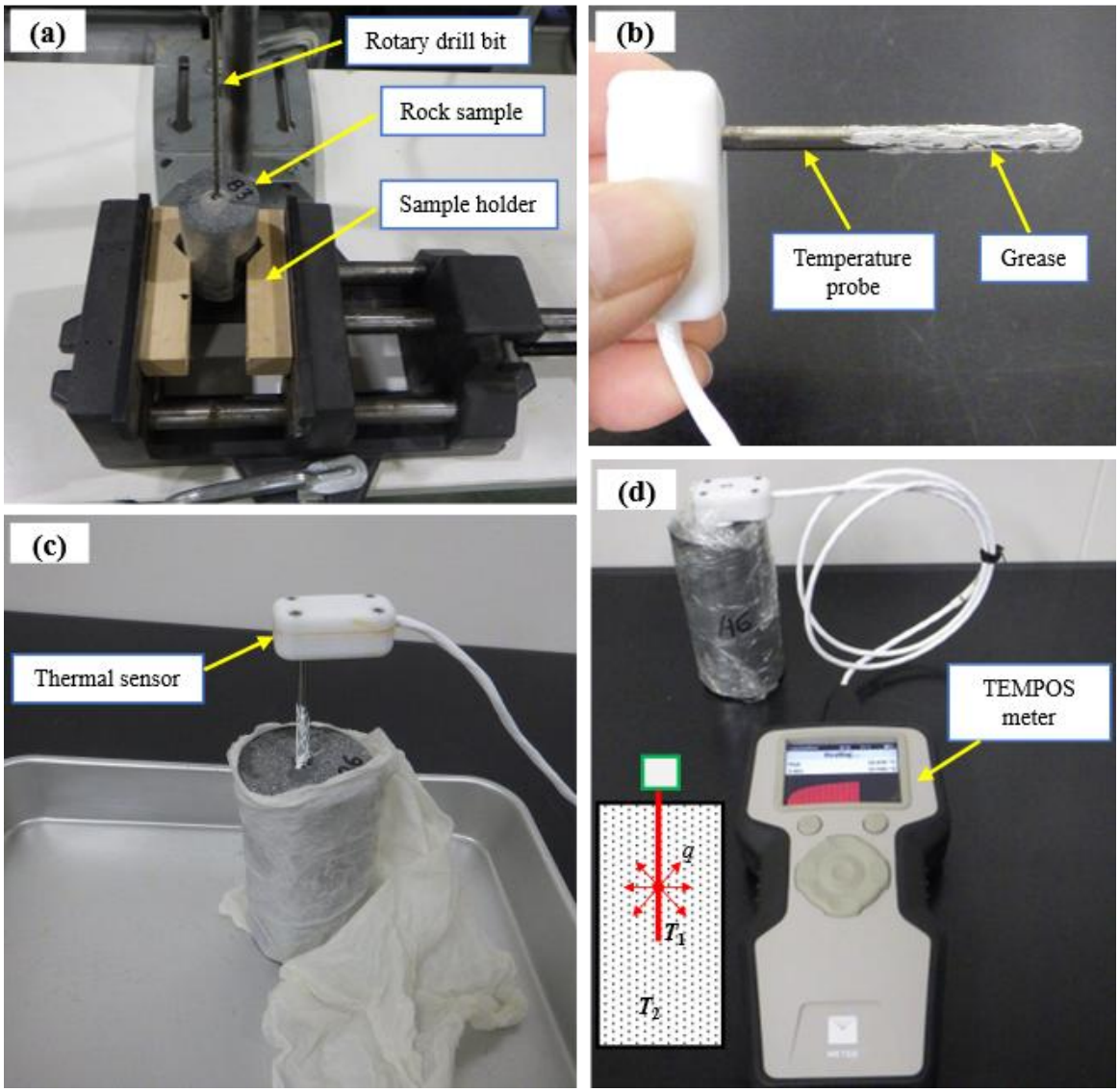

Figure 28 Laboratory thermal conductivity measurement techniques.

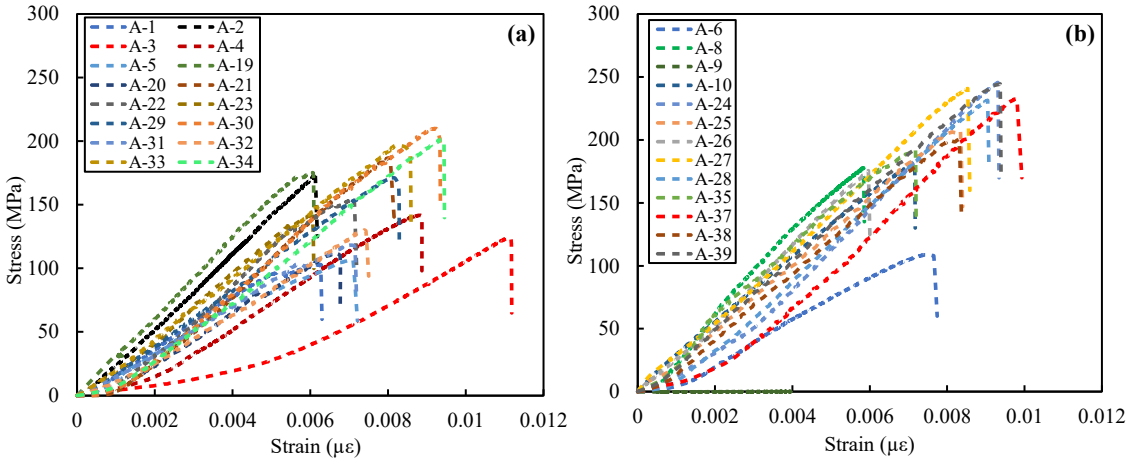

Figure 29 Typical stress-strain curves of studied rocks in (a) saturated condition; and (b) dry condition.

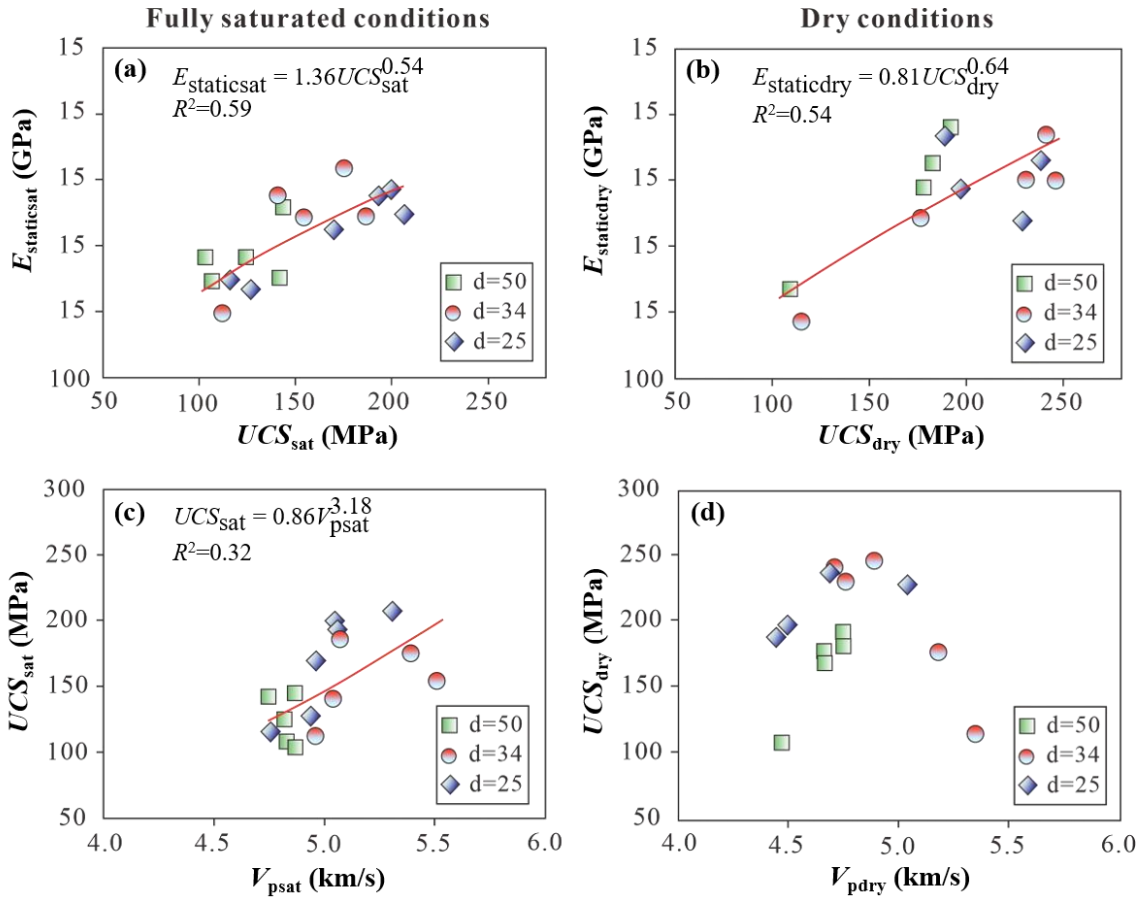

Figure 30 Relationship between (a) UCS_{sat} and $E_{staticsat}$; (b) UCS_{dry} and $E_{staticdry}$; (c) V_{psat} and UCS_{sat}; and (d) V_{pdry} and UCS_{dry}.

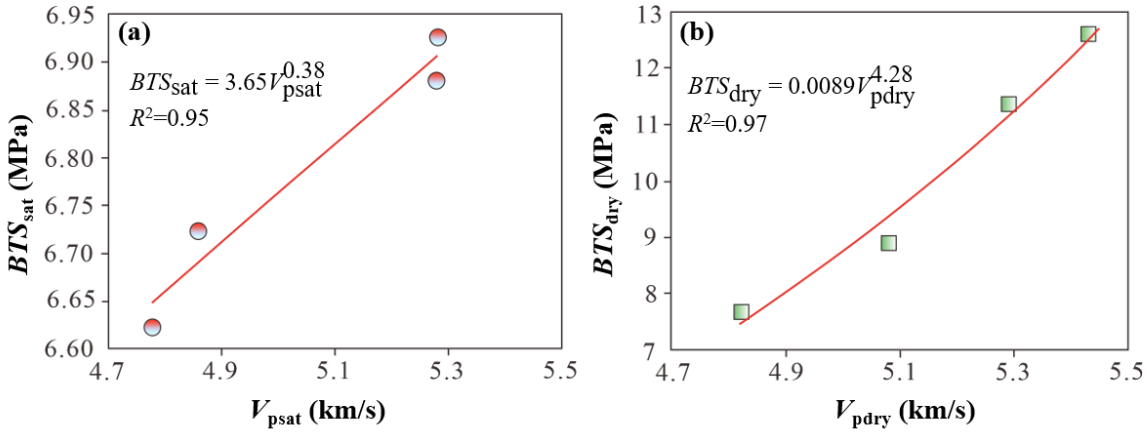

Figure 31 Relationship between (a) V_{psat} and BTS_{sat}; and (b) V_{pdry} and BTS_{dry}.

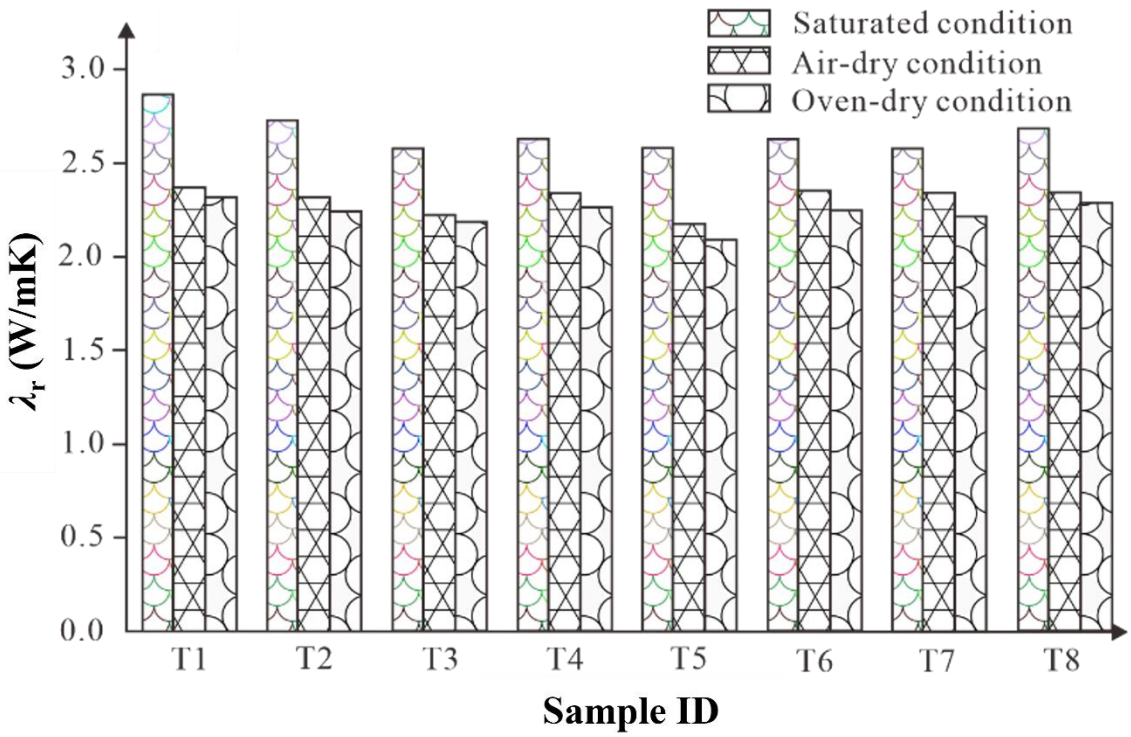

Figure 32 λ_r of specimens under three measurement conditions (saturated, air-dry, and oven-dry).

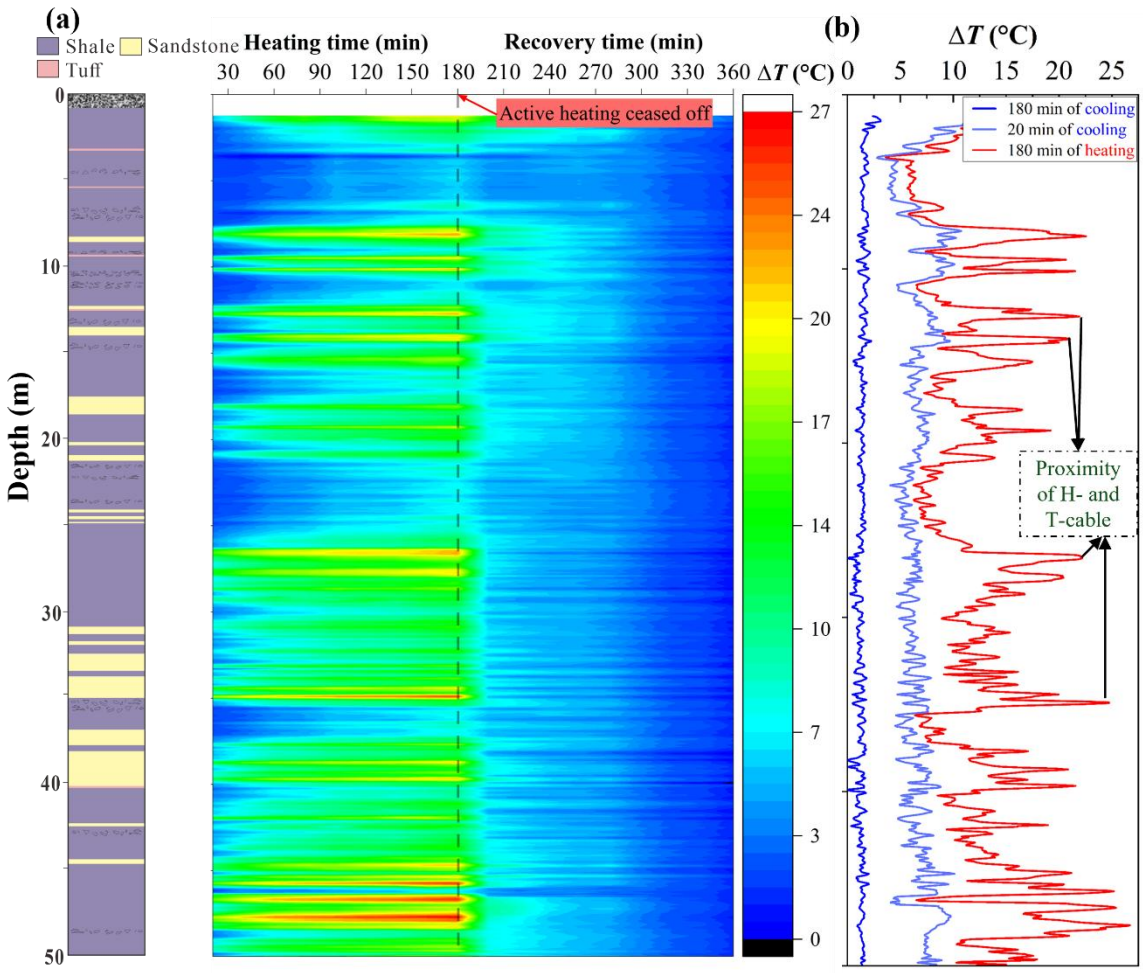

Figure 33 (a) Spatio-temporal thermal response over depth and time during heating phase and recovery phase; and (b) line profiles of temperature rise over depth at different times during heating and recovery phase.

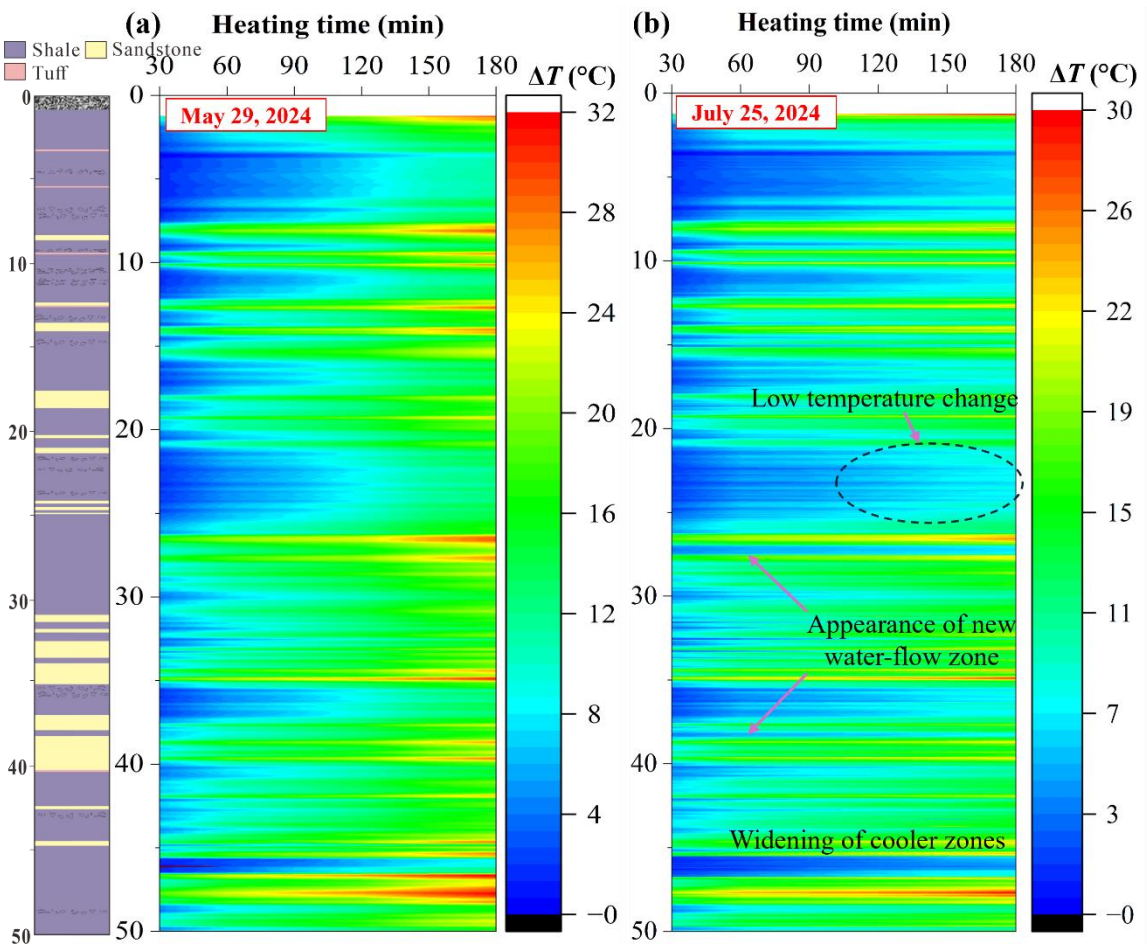

Figure 34 Subsurface Δ*T* over time during two AH-DFOS heating events conducted on (a) May 29, 2024; and (b) July 25, 2024.

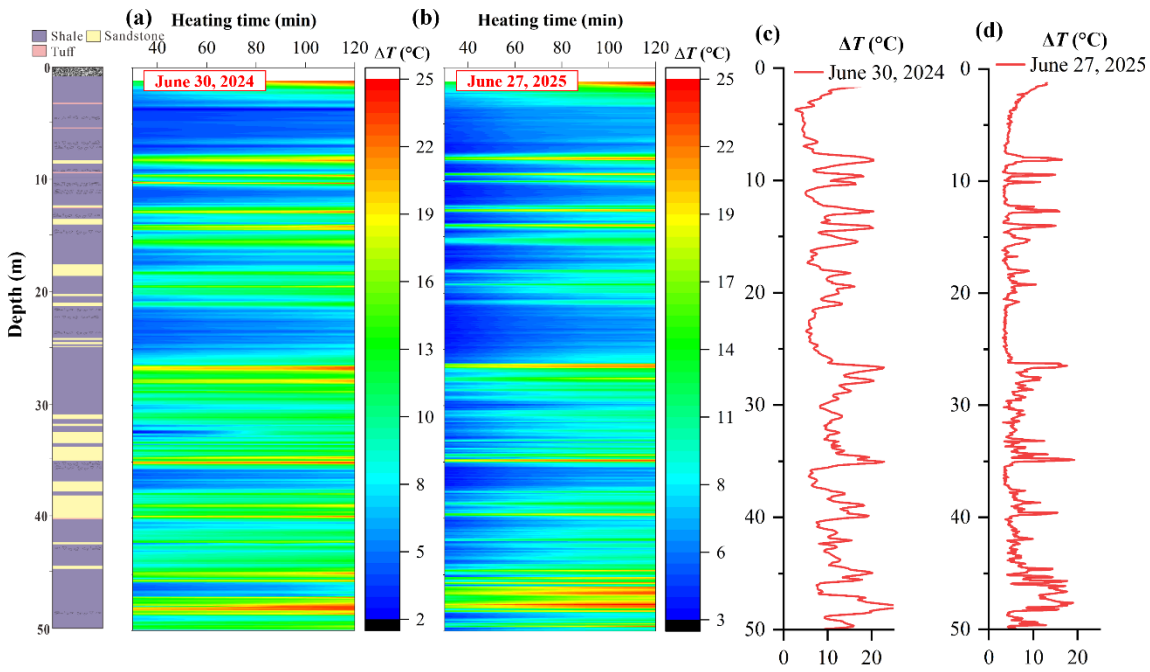

Figure 35 Subsurface Δ*T* over time during two AH-DFOS heating events conducted on (a) June 30, 2024; and (b) June 27, 2025. (c) and (d) represent heating line curves at these different times (data after 120 minutes of heating at different times were used to create this thermal response diagram).

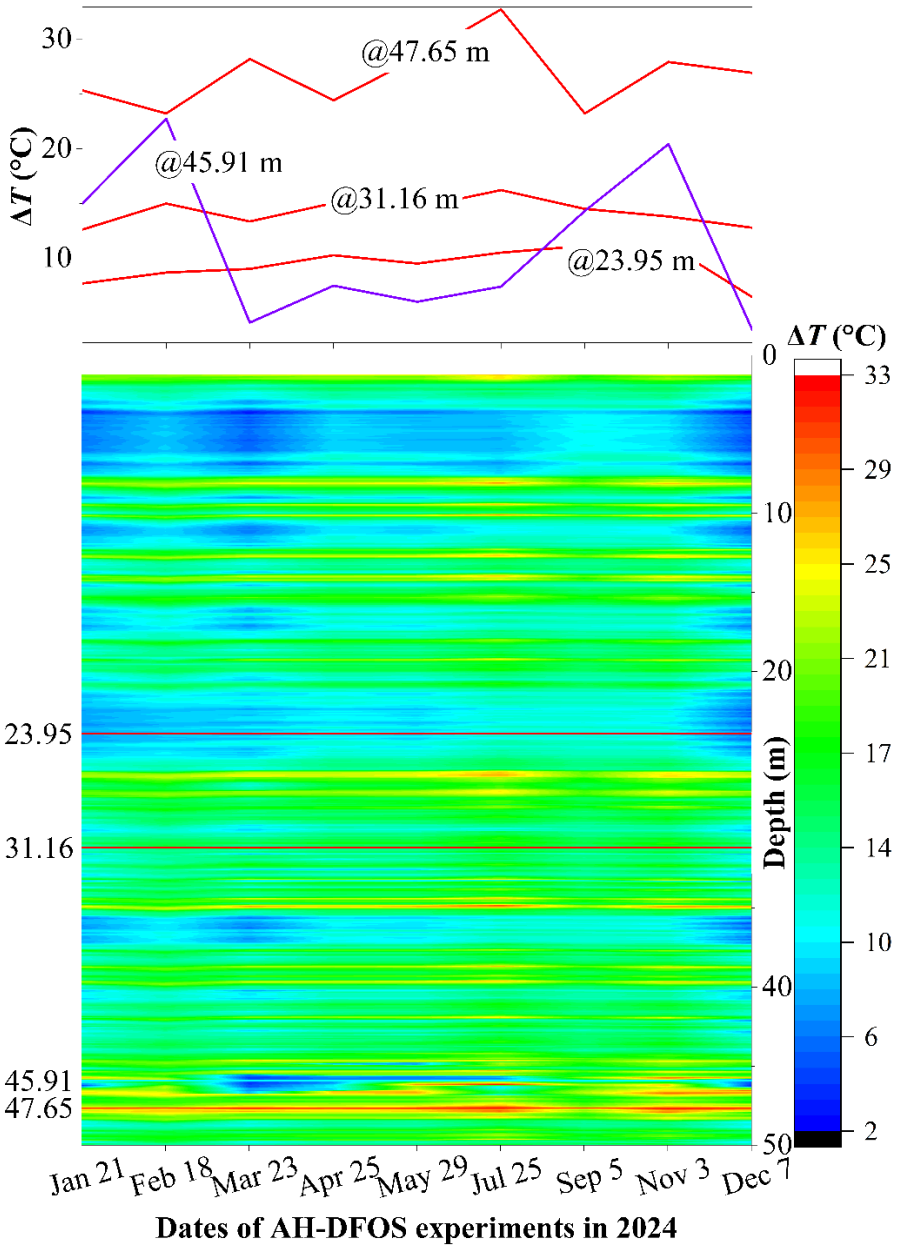

Figure 36 Temporal and depth-wise variation of Δ*T* during AH-DFOS monitoring in 2024 (data after 120 minutes of heating at different times were used to create this thermal response diagram).

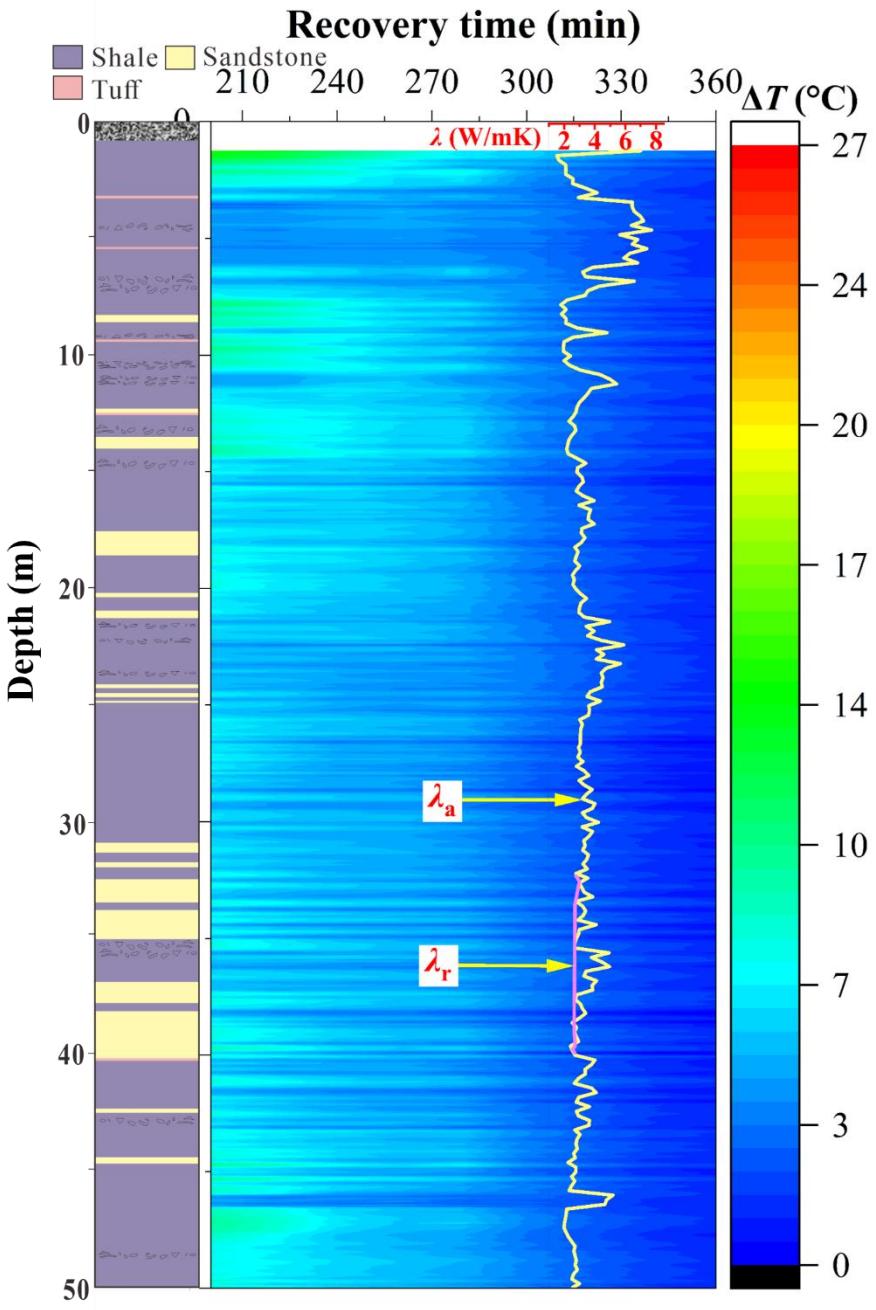

Figure 37 Effective and apparent thermal conductivity embedded in thermal response curve of recovery phase.

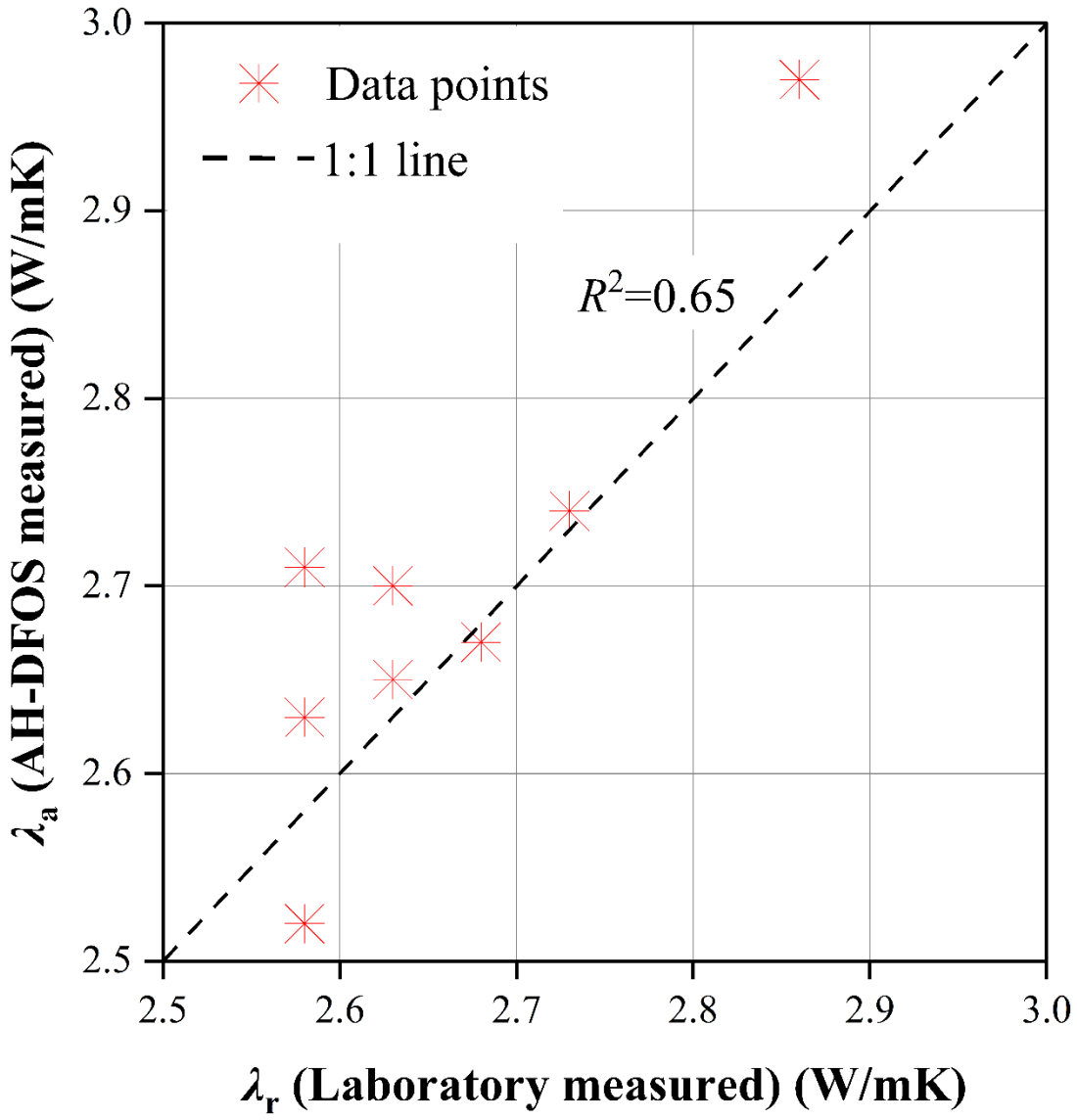

Figure 38 Comparison between λ_r (laboratory measured) and λ_a (AH-DFOS measured) in a 1:1 plot (i.e., y=x).

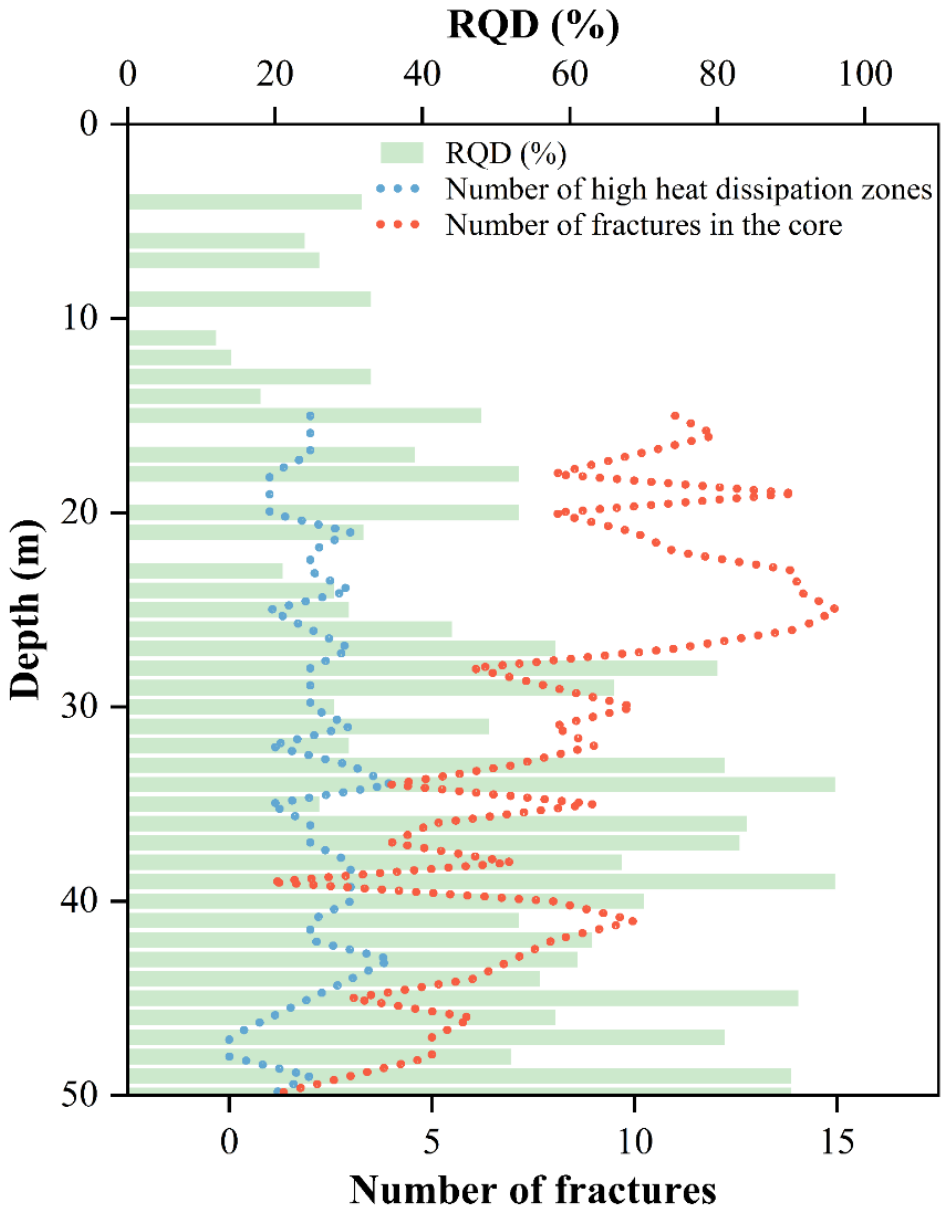

Figure 39 Total number of fractures observed in the core along with RQD values and number of high heat dissipation zones identified from the AH-OFDR method.

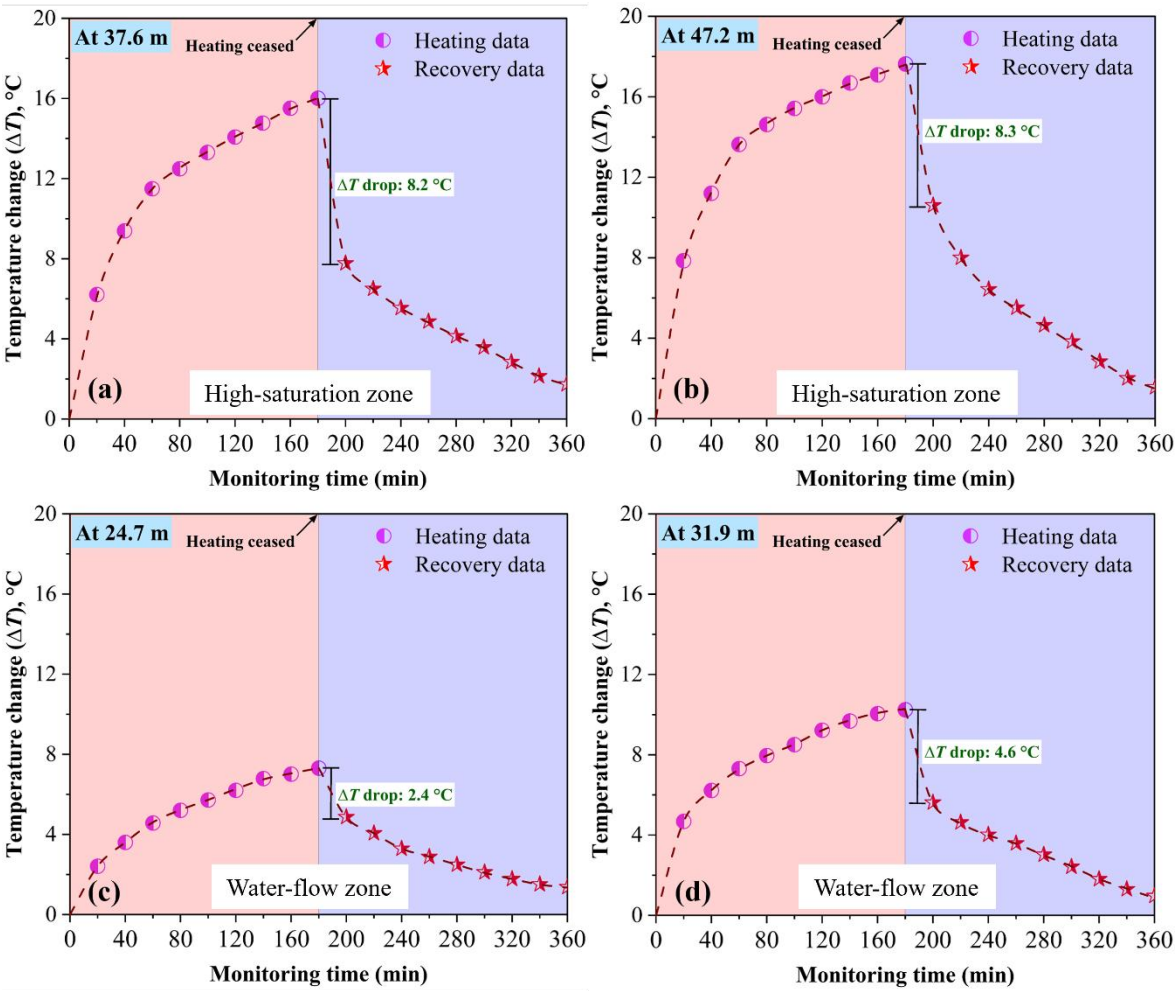

Figure 40 Trend of temperature rise and decling during heating and recovery phases. (a) and (b) high-saturation or conduction-dominant zones; (c) and (d) water flow zones (four representative points were selected based on recovery profile) (heating phase is represented by pink background on left and recovery phase is represented by blue background on right).

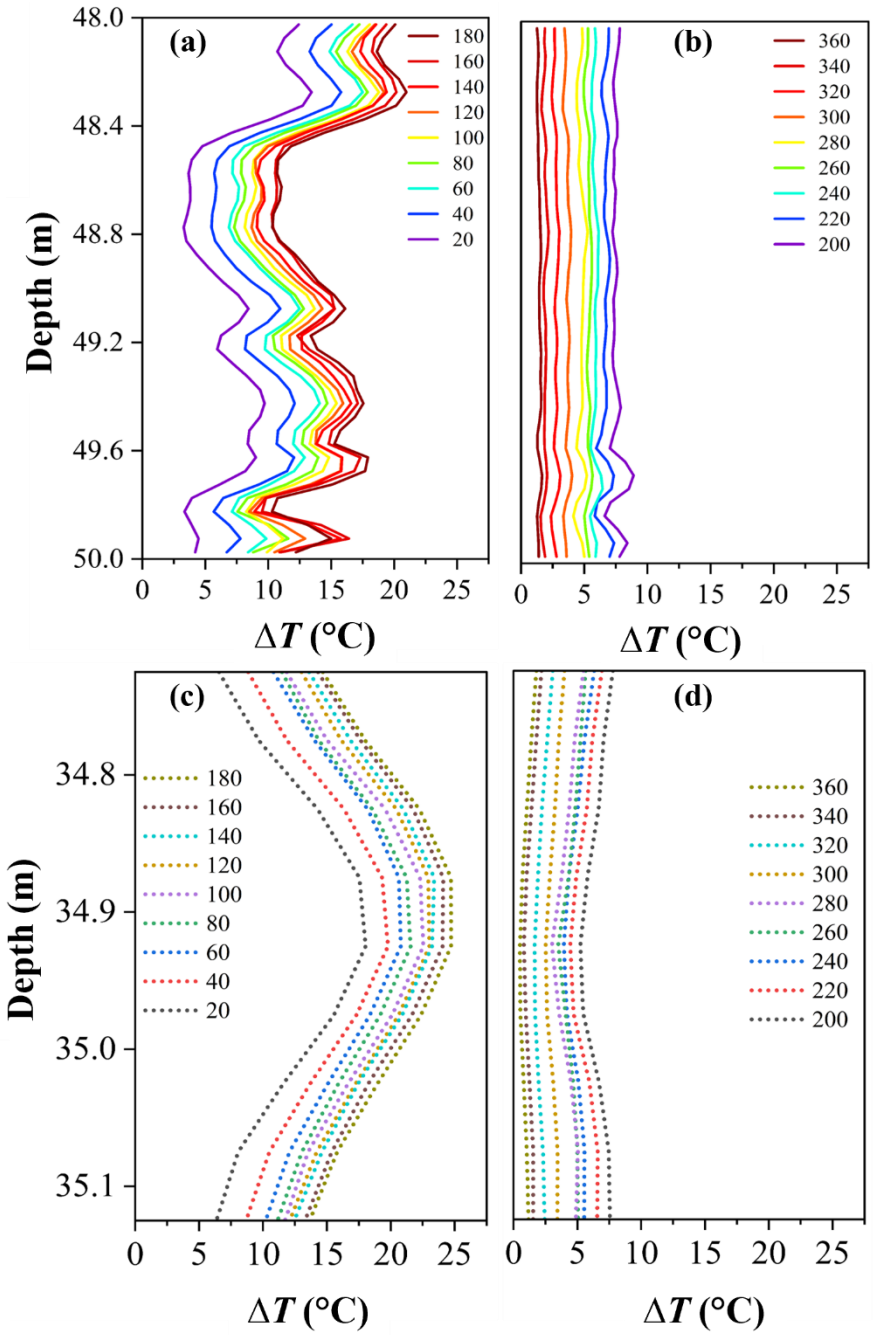

Figure 41 (a) and (b) 2-meter-deep line profiles of temperature rise and decline during heating and recovery phase, respectively; (c) and (d) typical heating line profile to mimic the influence of water flow during recovery phase.